THE STRUCTURE AND DYNAMICS OF THE INTERSTELLAR MEDIUM OF GALAXIES IN THE EARLY UNIVERSE

A THESIS SUBMITTED BY

ANA CAROLINA POSSES NASCIMENTO

TO THE

FACULTAD DE INGENIERÍA Y CIENCIAS
INSTITUTO DE ESTUDIOS ASTROFÍSICOS

In partial fulfillment of the requirements for the degree of Doctor of Philosophy in Astrophysics.

Supervisor: Manuel Aravena Aguirre

Co-Supervisor: Jorge González López

UNIVERSIDAD DIEGO PORTALES
Santiago, Chile
2023

APPROVAL REPORT

It is displayed on the next page a copy of the approval report signed by the Thesis committee.

INSTITUTO DE ESTUDIOS
ASTROFÍSICOS udp
FACULTAD DE INGENIERÍA Y CIENCIAS

Acta de Deliberación

Defensa de Tesis Doctoral

En Santiago, el 01 de diciembre de 2023, el Tribunal de Defensa de Tesis Doctoral compuesto por el profesor Dr. Manuel Aravena (UDP), Dr. Jorge Gonzalez-López (UDP), Dr. Roberto Assef (UDP), Dr. Carlos de Breuck (ESO, Alemania) y Dr. Kirsten Kraiberg Knudsen (U. Chalmers, Suecia), sobre la base del texto del proyecto, la exposición del doctorando y sus respuestas a las intervenciones de los miembros del tribunal, ha resuelto aprobar la tesis doctoral *The Structure and Dynamics of the Interstellar Medium of Galaxies in the Early Universe* de la doctoranda Ana Carolina Posses Nascimento.

Los miembros del Tribunal firman para constancia.

Manuel Aravena
Supervisor, UDP

Jorge Gonzalez-López
Co-supervisor, UDP

Roberto Assef, UDP

Carlos De Breuck
Digitally signed by Carlos De Breuck
Date: 2023.12.12 17:44:51 +01'00'

Carlos de Breuck
ESO, Alemania

Kirsten Kraiberg Knudsen
U. Chalmers, Suecia

This thesis contains the work that has been developed during the rise, peak, and decay of the COVID-19 pandemic. I dedicate it to all of us who face these hard times and lost dear family and friends.

ACKNOWLEDGEMENT

More than 10 years ago, when I decided to pursue a career as an astronomer, I looked with great admiration at the title of doctor. It was that moment when I thought: wow, I am going to contribute to science! My entire journey, from leaving the small town of Colatina in 2012 to study in Rio de Janeiro, to my current time in Chile, has been marked by a lot of effort and an eagerness to learn and explore the universe more deeply. I must say, these past four years were particularly challenging. However, I consider myself a very fortunate person because I have people by my side who, with their warmth and love, helped me get here and achieve a title I have been dreaming of for years. I want to express my gratitude to those who have been part of this journey:

- I want first to thank my research group. I appreciate the care and dedication of my advisors, Professor Manuel Aravena and Professor Jorge González-Lopez. I truly feel like a very fortunate person because I had such dedicated and kind mentors. You believed in me during various moments when I doubted myself. I will be eternally grateful for this. Thank you so much to Professor Roberto Assef, and Professor Tanio Diaz for the discussions in our meetings. I appreciate the company of my colleagues Manuel Solimano and Trystan Lambert for their on this student journey.

- All the amazing four years that the Instituto de Estudios Astrofísicos provided me with. I felt well received and welcomed from day one, up to undoubtedly the last day I will leave here. I was part of the first class of doctoral students and had the opportunity to witness the department grow through the hard work and care provided by the faculty. These years have shown me that it is possible to treat students respectfully and humanely. In particular, I express my gratitude to Professor Lucas Cieza for being so dedicated to welcoming us and assisting with all the administrative and bureaucratic processes of being a foreigner in Chile. I thank my dear professors Jose Prieto, Paula Jofre, and

Manuel Aravena. I appreciate all the administrative, cleaning, and security staff who made it possible for us to use the university facilities for our research.

- To all the incredible people I met and friends I made at UDP, especially: Dejene (thank you for all the friendship and for helping me on my first day in Chile), Keerthana, Anya, Emilio, Manuel (cat buddy), Trisha (and Ranajit!), Pablo and the Brazilian gang.

- I would like to express my gratitude to Professor Natascha Förster-Schreiber, Professor Scott Chapman, Dr. Ryley Hill, and Professor Eduardo Banados for hosting me during collaborative visits to their institutes. Thank you for the time you made available and the knowledge shared and discussed.

- For the weekly soccer and volleyball matches with colleagues and friends in this last year of my Ph.D. I am very grateful for all the engagement in playing, even on the coldest days. Thank you so much, Camilo, Emilio, Douglas, Florence, George, Karen, Kristy, Kurt, Manuel, Camilla, Pascal, Pedro, Priscila, Suman, Tatevik, Natali, Kevin, Rafi, Ranajit, Thallis, Jay, Cata, Sara!

- For the people of Chile who welcomed me in such a hospitable and warm manner. I appreciate all the Chilean taxpayers who made it possible for me to pursue my studies here. It has been a pleasure to learn more about your culture and gain a deeper understanding of your victories, struggles, and pains. You have taught me about the importance of connecting more with Latin America and being proud of where we come from. From the bottom of my heart, I wish that the ongoing struggles lead you to the dignified future you truly deserve. Viva Allende!

- To my family, for always believing in me. To my parents who provided me with the opportunity to live my career dream and for their unwavering support from the very first moment I wanted to become an astronomer. You have taught me the power of how education can change our lives and our perception of the world. I am eternally grateful for this. Thanks to all my aunts, uncles, cousins, and grandparents who have always supported me. I especially want to express my gratitude to my uncles Marco and Cheila, and cousin Marina, whom I would meet with a smile every Christmas. They would ask me about how my studies were going. Unfortunately, I won't be able to tell you that I have finally finished, but you have always been in my thoughts.

- To my dear Brazilian friends Priscilla, Danielle, Douglas, Thallis, Tuila, Florence, Ana, and Larissa. You made me laugh and happy during these last four years away from home. You are so special to me and always will be in my heart, and make me proud to come from our lovely country. Thank you so much!

- I thank the love of my life, Pedro Nogueira. How honored I feel to build a life with you over these past 10 years. Your joys are my joys, your pains are my pains, and your achievements brighten my day. It brings me joy to have your smile, humor, and love every day. I am completely in awe of your character and kindness. I am looking forward to building a life together for the next 10, 20, and 30 years. I love you and our reizinho Morpheu!

- To Vitor and Evelyn for leading such a beautiful project as INEF. I am immensely grateful for your dedication to everything you do and for your didactic approach. You were my companions during the pandemic and were essential in helping me develop critical thinking. I thank my colleagues from Clube das Juremas for the meetings, where different points of view enriched my way of seeing the world. Thank you, Joana, Herly, Tiago, Joeice, Silvio, Belmiro, and everyone who has been part of our club.

- To all the friends I made during conferences, and especially to La Serena School and La Silla Observing School.

- To my dear friend and former advisor Duilia de Mello, thank you so much for all the warmth and support over the years. You will always be an eternal inspiration to me.

- To the members of the thesis committee, Dr. Kirsten Kraiberg Knudsen, Dr. Carlos De Breuck, and Dr. Roberto J. Assef, thank you very much for the rich discussions over the years and for your comments on my thesis.

I thank everyone I have been in contact with over the past few years.

ABSTRACT

We are reaching a critical moment where sub-arcsec observations are key to disentangle the physical mechanisms that shaped young galaxies at $z > 5$. In this thesis, we explored the morphology and kinematics of the cold gas, star-forming, and stellar components of two massive star-forming galaxies at $z = 5 - 7$, using high-resolution ($0.3''$) ALMA observations of the [C II] 158μm line emission. Our analysis shows that COS2987, at $z = 6.8$, is found to be composed of a main central source, a fainter north extension, and candidate [C II] companions located 10 kpc away. The agreement between the UV and [C II] surface brightness radial profiles rules out diffuse, extended [C II] emission in the main galaxy component. The [C II] velocity map reveals a velocity gradient in the north-south direction, as commonly found in rotating-disk galaxies. Kinematical modeling returns a dispersion lower than the expected value from observation trends and semi-analytic models of high redshift galaxies.

The second galaxy CRISTAL-05 , at $z = 5.54$, is actually a complex close encounter surrounded by a disturbed carbon-rich gas. This is imprinted in the disturbed [C II] morphology and the separation of the two components in the position-velocity diagram. The central region is composed of two components, named C05-NW and C05-SE , with the former being the dominant one. A significant fraction of the [C II] arises beyond the galactic disk up to 10 kpc, while the regions forming new massive stars and the stellar component, as traced by rest-frame UV and optical imaging obtained with the Hubble Space Telescope and the James Webb Space Telescope, seem compact ($r_{[CII]} \sim 4\times\ r_{UV}$). We argue that the extended [C II] emission is due to this close merger, which would have been impossible to discern with lower-resolution observations. Our analysis suggests that the galaxy assembly in the early universe is dominated by frequent episodes of satellite accretion, while mature rotating disk galaxies may already be in place. This work reinforces the importance of resolution surveys in the exploration of the properties and stages of the earliest galaxies in the universe.

CONTENTS

3 [CII] extended emission in an interacting system at z $\sim$ 5.5 45

FIGURE

TABLE

CHAPTER 1

INTRODUCTION

Astronomers are the historians of cosmic time. By pointing large telescopes to the dark sky and digging huge amounts of data, we aim to unravel the tales of how the Universe has formed and evolved, from fundamental elements to large structures through the 13 billion years of cosmic history. Extensive studies in the last century have revealed that a crucial side of this history is hidden in a dark universe. Dark matter and dark energy are fundamental components that shape the large structure of the universe, although their nature still challenges our understanding. Luckily, we can access and study the light emitted from the interfaces to these hidden components, the galaxies, whose properties and evolution are directly influenced by them. Galaxies are the result of the gravitational collapse of baryons in dark matter halos, and by the time they began to be formed, they completely changed the formation of the structures and drastically affected the environment within, around, and beyond them. Therefore, it is a major goal of modern astrophysics to shed light on how these fundamental building blocks evolved.

In this thesis, we gladly detail the work we have been developing in the last four years. We aim to provide valuable and novel perspectives on the evolutionary stage of galaxies close to the first billion years of the universe. We explore the structural and dynamic aspects of the interstellar medium (ISM) of typical star-forming galaxies, which are the main responsible for galaxy assembly at all redshift ranges. We take advantage of the capabilities of the revolutionary ALMA observatory to dissect the [C II] emission, a powerful tool to access the multiphase gas medium, as we will see below. In this chapter, we introduce the scientific background required to provide a comprehensive basis for the subsequent analysis of our research findings.

1.1 GALAXY COMPONENTS AND OBSERVABLES

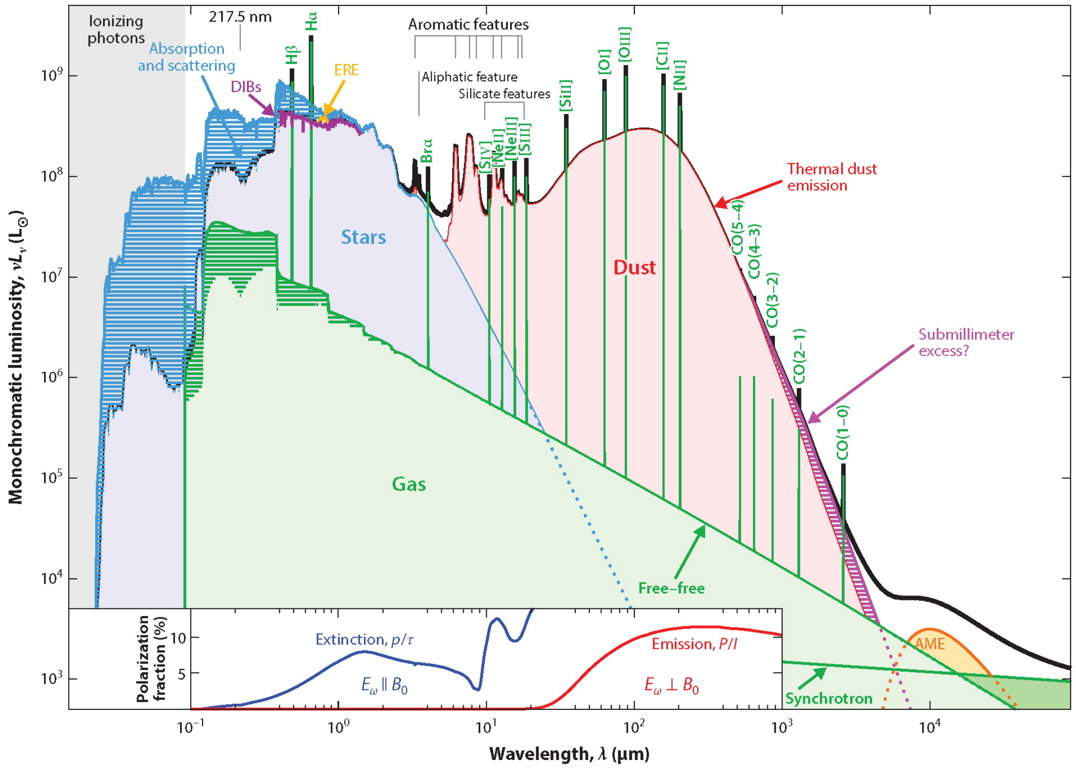

Galliano F, et al. 2018.
Annu. Rev. Astron. Astrophys. 56:673–713

Figure 1.1: Spectral energy distribution of a typical late-type galaxy. Image credit: Galliano et al. (2018)

A galaxy is a gravitational-bounded system composed of numerous populations of stars, planets, stellar remnants, multiphase gas, dust, and dark matter. The main properties and history of a galaxy are imprinted in its spectrum, which is the sum of all the line and continuum emission of all these components, but mainly dominated by the radiation processes in stars, gas, and dust. Figure 1.1 exemplifies a spectral energy distribution of a star-forming galaxy. We below present a description of different parts of a galaxy and observables.

1.1.1 STARS

Stars are one of the main components within galaxies, as they provide information about the star formation history and physical processes affecting their evolution. They usually dominate the restframe UV, optical, and near-infrared emission of the spectral energy distribution

(SED) (Fig. 1.1). In particular, the restframe UV regime in galaxies is primarily composed of the emission from the massive, hot, and bright short-lived stars (lifetime of 10-100 Myr). Therefore, they are a direct tracer of the recent star formation. Considering a Kroupa stellar initial mass function, with constant star formation over 100 Myr, the far-UV ($0.0912\mu\mathrm{m} < \lambda < 0.2\mu\mathrm{m}$) stellar continuum can be converted to an unobscured star formation rate (SFR) as

$$\mathrm{SFR} = 2.24 \times 10^{43} \times (\nu \mathrm{L}_{\nu}), \tag{1.1}$$

with νL_{ν} in units of erg s^{-1}, and the SFR in units of $\mathrm{M}_{\odot}\ \mathrm{yr}^{-1}$ (Kennicutt & Evans, 2012). The main caveat is that the restframe UV emission is easily obscured by dust. Therefore, we also need to account for the obscured star formation by observing the dust continuum emission (see below).

Conversely, less massive stars will dominate the stellar mass composition of galaxies since they have longer lifetimes. To fully characterize the stellar component of a galaxy, we must observe the restframe optical and near-infrared part of the spectrum and measure the emission from colder stars less affected by dust.

1.1.2 INTERSTELLAR MEDIUM

The interstellar medium (ISM) refers to a broad collection of material that fills the space between stars. We focus on the emission contribution of the gas and dust below.

GAS

The gaseous component ISM can be in most general terms divided into three phases: cold (T < 300 K), warm (T $\sim 10^4$ K), and hot (T $> 10^5$ K). We summarize the main components and characteristics as follows (Figure 1.2):

- **Molecular clouds:** Gravitationally bound clouds are composed mostly of molecular hydrogen. Typical temperatures and density are 10 – 50 K, and $10^3 - 10^6\ \mathrm{cm}^{-3}$, respectively, having thus the required conditions to be the place where star formation takes place. Tracers: low-J CO transitions (2.6 mm), and contributions of far-infrared fine-structure lines [C I] , [C II] , and HI.

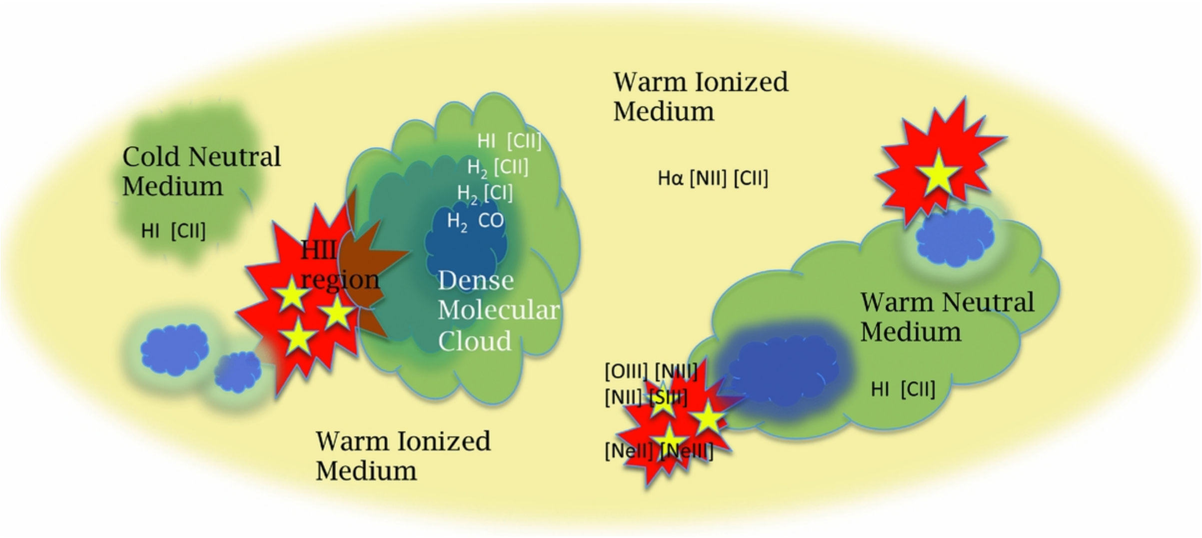

Figure 1.2: Schematic picture of the origin of fine structure and molecular line emission in the mid and far-infrared ranges from the various ISM components of galaxies. Image credit: van der Tak et al. (2018).

- **Cold neutral medium (CNM):** Composed mostly of neutral atomic hydrogen, with typical temperature and density of T = 100 K and 30 cm^{-3}, respectively. It fills around 1% of the volume of the ISM. Also known as cold HI. Tracers: H I, [C II] .

- **Warm neutral medium (WNM):** Composed mostly of neutral atomic hydrogen, and normally surrounds neutral clouds (mainly found in photo-dissociation regions). For this reason, it can be heated to temperatures of T = 8,000 K, with a density of $\sim$ 0.5 cm^{-3}. It composes around 40% of the ISM. Tracer: H I, [C II] .

- **Warm ionized medium (WIM):** Ionized hydrogen phase by energetic UV photons from massive stars, with typical temperatures of T = 10,000 K. It can be found either nearby massive stars as HII regions ($\sim 10^2 – 10^4$ cm^{-3}) or in a more diffuse intercloud phase (0.1 – 10 cm^{-3}). Tracer: H_α, [N II] , [C II] .

- **Hot ionized medium (WIM):** Hydrogen ionized phase heated by supernova explosions. It has the lowest density (0.004), but the highest temperatures (T $\sim$ 1,000,000 K) than other phases. Also known as hot coronal gas.

A crucial measurement for galaxies is to quantify the amount of fuel available for star formation. The cold temperature (T < 100 K) and high density seen in molecular clouds are the required conditions to allow stars to be formed. The most common element in these regions is the H_2 molecule, which does not have a permanent dipole and the excitation of the quadrupole transition requires high temperatures (Omont, 2007), which is not reached in the cold phase. Several indirect tracers of the molecular gas mass are available, relying on the conversion of the line luminosity to molecular gas mass by a mass conversion factor α (that may depend on the galaxy properties). The most used tracer is the low-J transition of the carbon monoxide atom CO (Bolatto et al., 2013). The main advantage is that this is the second most abundant molecule in the cold gas phase, but this is a very faint line and may be affected by the cosmic microwave background (CMB) at high redshifts. Recent studies have shown that alternatives, as reliable as the low-J CO lines, can be the fine-structure lines of the atomic carbon [C I] 492 and 809 GHz (Papadopoulos & Greve, 2004; Heintz et al., 2021), and the far-infrared [C II] 158μm, (Zanella et al., 2018). More details on the [C II] line are provided in the next Section.

DUST

The observation of the dust emission is the final piece of the puzzle to fully reveal the stellar properties of galaxies. Interstellar dust is a collection of particles, mainly composed of silicate or carbonaceous material (such as graphite and Polycyclic Aromatic Hydrocarbons), but also containing ice and metals (Galliano et al., 2018). They have sizes ranging $\sim$ from 0.3 nm to $\sim$ 0.3 μm, and despite having a subdominant contribution in the bulk mass of the ISM, their properties strongly affect the measurement of several observables. For instance, dust absorbs the preferentially short wavelength photons of stars and re-emits it as a thermal continuum emission at longer infrared wavelengths. In local normal galaxies, this re-emission can reach up to $\sim$ 30% of the absorbed stellar light (Skibba et al., 2011; Bianchi et al., 2018), dominating the emission at $\lambda > 10$ μm (Figure 1.1). Since most of the emission coming from star-forming regions corresponds to bright stars emitting mainly in the UV regime, a significant fraction of the SFR can be dust obscured. Considering a Kroupa stellar initial mass function, with constant star formation over 100 Myr, the bolometric IR luminosity ($3\mu\text{m} < \lambda < 1100\mu\text{m}$) dust continuum can be converted to an obscured SFR as

$$\mathrm{SFR} = 2.57 \times 10^{43} \times (\nu L_\nu), \tag{1.2}$$

with νL_ν in units of erg s^{-1}, and the SFR in units of M$_\odot$ yr^{-1} (Kennicutt & Evans, 2012). The measurement of the bolometric IR luminosity requires knowing the shape of the dust SED. To achieve this, it is essential to have a well-sampled photometry of the infrared continuum to constrain the temperature and emissivity index. Since at high redshift, often we have only a single data point (usually 850μm or 1.2 mm) in the Rayleigh Jeans-limit (> 200 μm), typical models of the dust far-infrared SED assume a modified back-body shape, with a constant redshift-dependent dust temperature (Béthermin et al., 2014) in the optically thin regime.

1.1.3 [C II] EMISSION LINE

Among all the tracers of the multiple gas phases presented at 1.1.2, we highlight the [C II] line emission. It refers to the radiative de-excitation of singly ionized carbon atom (C$^+$) via the fine-structure level transition $^2P_{3/2}$ - $^2P_{1/2}$. The decay releases a photon with a wavelength of λ_{rest} = 158 μm (equivalent frequency of ν = 1900 GHz), placing it in the far-infrared regime of the SED of a galaxy (Figure 1.1). The line has been openly used as the main diagnosis of ISM of early galaxies due to the conditions to produce the emission and observational capability. At $z > 4$, the line is redshifted into the (sub)mm atmospheric windows (Fig. 1.3), which makes it observable with ground-based (sub)mm facilities such as ALMA (Carilli & Walter, 2013).

The carbon atom has a low ionization potential of 11.2 eV (below the hydrogen ionization potential of 13.6 eV). It means that it can be easily ionized in any region exposed to UV photons, making it the dominant form of carbon under a wide variety of environments. The [C II] line mainly traces regions of neutral hydrogen gas (photodissociation regions, outer regions of molecular clouds, Stacey et al., 2010; Gullberg et al., 2015) and diffuse neutral gas due to excitation by collision with neutral hydrogen atoms (Goldsmith et al., 2012). However, it also has contributions from diffuse ionized gas regions due to collisions with free electrons (Goldsmith et al., 2012). Moreover, this is one of the strongest far-infrared (FIR) lines, reaching up to 1% of the total bolometric luminosity (Díaz-Santos et al., 2013; Cormier et al., 2015; Herrera-Camus et al., 2018a; Schaerer et al., 2020).

The emission acts like a thermostat since it is an important coolant of the ISM, mainly heated by the photoelectric effect (Draine, 1978). The heating sources are the massive young stars, providing enough energy to eject electrons from dust and polycyclic aromatic hydrocarbon (PAHs). These released photoelectrons collisionally heat the gas. The carbon ion [C II] can be excited by electrons, and atomic and molecular hydrogen, depending on the gas conditions (Draine, 2011).

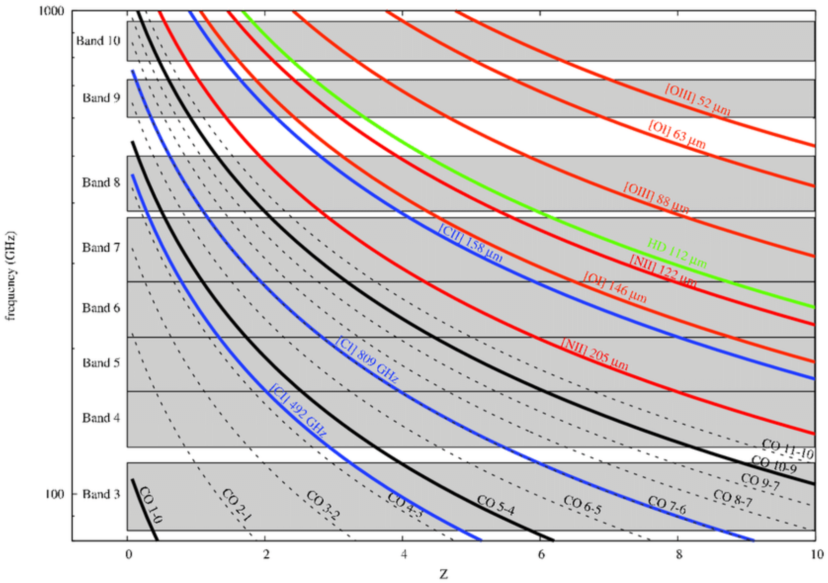

Figure 1.3: Redshifted observed frequency of ISM emission lines as a function of redshift. The frequency ranges of ALMA receivers are plotted as gray areas. Image credit: de Ugarte Postigo et al. (2012).

1.2 FUNDAMENTAL BUILDING BLOCKS

Galaxy evolution aims to reconstruct back in time the major events and underlying physical mechanisms that have shaped galaxies' properties the way we see them today. In this section, we provide a brief introduction of the theoretical framework and hints of galaxy formation.

1.2.1 GALAXY FORMATION AND EVOLUTION: A BRIEF VIEW

According to the classic paradigm of galaxy formation in the ΛCDM cosmological framework, the dark matter halos are the gravitational foundation upon which galaxies are built. We provide a synopsis of what is extensively detailed in several textbooks (Ryden, 2003; Longair, 2008). At around redshifts of z $\sim$ 30 - 20, dark halos begin to collapse from small irregularities in the density field of the universe. Before it, the matter distribution was relatively homogeneous, with small density perturbations. These overdense regions grow initially linearly, and as gravity overcomes cosmic expansion, the dark matter halos collapse. The gas falls towards the potential wells of the growing dark matter halos, being heated to the virial temperature of the galaxy by accretion shocks, and then cools via atomic and molecular transitions. The condensation allowed the cold gas to form the first generations of stars.

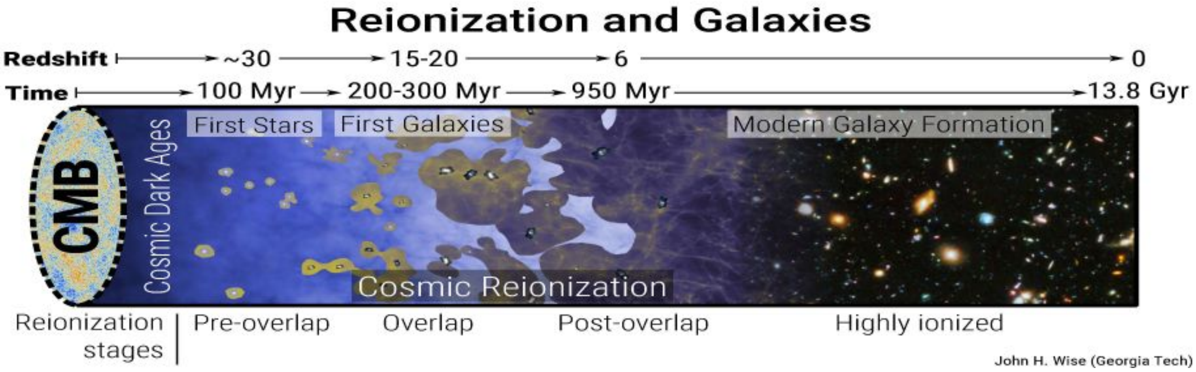

Figure 1.4: Cosmic timeline of the universe along recombination. Image credit: Zaroubi (2013).

The first stars influenced not just structure growth in the central regions of the dark halo potential wells but also modified the conditions of the matter embedded between these new sites. It triggers the beginning of the reionization epoch at z $\sim$ 30 (Zaroubi, 2013; Dayal & Ferrara, 2018), schemed in Figure 1.4, which ends up around z = 6. The ionizing radiation emitted by these initial generations of stars transformed the intergalactic medium from a neutral state to an ionized one.

The formation of the first stars sited in the first galaxies remarks as a crucial transition in the evolution of the structure of the universe. Previously, the growth of dark matter halos was exclusively driven by gravity, and the role of baryons was marginal. Starting from this point, the evolution of the baryonic component of a galaxy becomes dominant on small scales and galaxy growth continues in a bottom-up (hierarchical) scenario. A proper treatment of galaxy evolution accounts additionally for the complex interplay of physics mechanisms that affect the formation of stars, such as gas accretion, AGN, and stellar feedback.

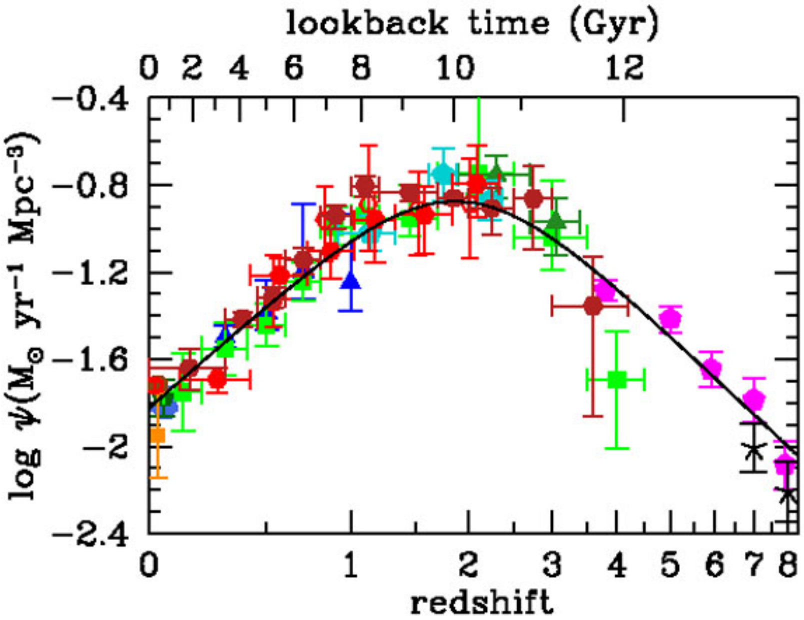

Figure 1.5: Comoving star formation rate density in the universe as a function of cosmic time. Image credit: Madau & Dickinson (2014).

1.2.2 COSMIC STAR FORMATION DENSITY

The stars provide the primary clues to access the assembly and evolution of galaxies since these are governed by complex and interconnected physical processes that directly affect the rate at which they are formed. The processes of star formation and subsequent death of stars, for instance, release energy to the ISM, dissipating it and/or heating it at the point it prevents the formation of new stellar populations. Another source of halting can also be the energetic processes taking place in the nuclear supermassive black hole of a galaxy. Both stellar and AGN feedback impact not just the internal ISM but the circum- and intergalactic medium (CGM), but cause deep structural changes in the way matter is distributed and chemically composed. On the other hand, galaxy growth can occur due to external processes such as merger activity and gas accretion from the intergalactic medium (IGM). It acts as a counterweight for feedback, as it provides the gaseous fuel for triggering the formation of new stars (Elmegreen & Elmegreen, 2005; Conselice & Arnold, 2009; Duncan et al., 2019; Shibuya et al., 2022).

A key measurement has been the determination of the evolution of the cosmic star formation rate (SFR) density with redshift (or cosmic time), which is defined by the comoving space density of the global SFR in a unitary volume of the universe. The latest measurements show that the cosmic star formation density is not constant across cosmic time (Madau & Dickinson, 2014). It yields three main epochs for galaxy assembly (Fig. 1.5):

(1) At z $\sim$ 8 -3: cosmic dawn, where the first galaxies were formed, we observe a rapid increase of the SFR density.

(2) At z $\sim$ 3 - 1: the so-called cosmic time, where most stars in the universe were created, yielding a peak of the cosmic SFR density.

(3) Slow decrease in the cosmic SFR density at z $<$ 1, corresponding to approximately the last 10 Gyr to the present day.

Interestingly, 50% of the stars we see in the universe today were formed at the peak of the cosmic SFR density. About 25% were formed at z $>$ 2, and the other 25% roughly over the last half of the universe time, at z $<$ 0.7. Understanding when and how these physical mechanisms were in place in galaxies is crucial for comprehending how the internal properties of galaxies have evolved over time. The cosmic star formation density hence provides deep insights into the growth, chemical, and structural evolution of galaxies.

1.2.3 MAIN SEQUENCE OF STAR-FORMING GALAXIES

A dominant fraction of the star-forming galaxies that contribute to the evolution of the cosmic SFR density form a correlation between the SFR and the stellar mass. This relationship usually called the star-forming ‘main sequence’ (MS), makes it evident that the most massive galaxies have higher SFRs (Brinchmann et al., 2004; Speagle et al., 2014; Schreiber et al., 2015). Galaxies above the MS are typically called ’starbursts’ and those below it are identified as ’passive’ galaxies. The left panel of Figure 1.6 shows the evolution of the main sequence taken from the best fit to observations from the literature by Speagle et al. (2014), as we can see changes in the slope and around 2 orders of magnitude in the SFR at a fixed mass from z = 4 to 0. This relationship, which holds for z = 0 – 6 indicates that there is a regulating mechanism for star-forming activity.

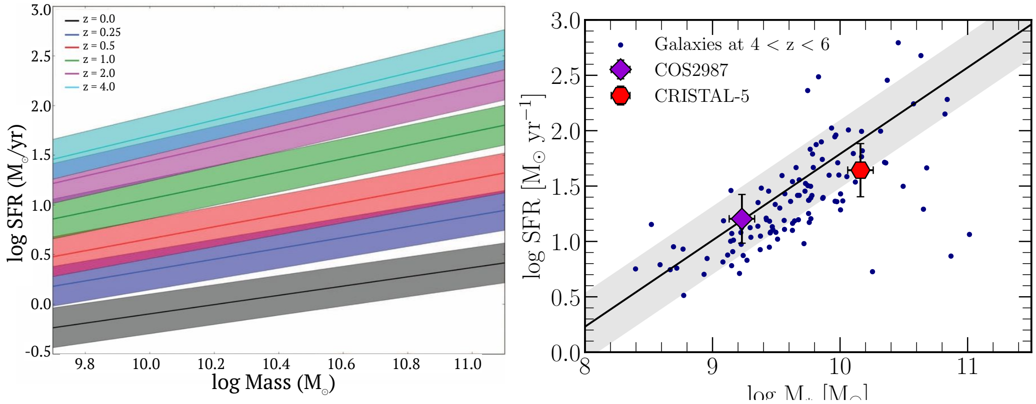

Figure 1.6: The star formation rate of the main population of galaxies as a function of the stellar mass. It lies in a positive power-law correlation called frequent main-sequence relation. (a) Left panel: Evolution of the main sequence from z = 4 to 0, taken from the literature by Speagle et al. (2014). (b) Right panel: Galaxies from the ALPINE survey (Le Fèvre et al., 2020), at $4 < z < 6$ (navy color points). The best-fit main sequence at $z \sim 5$ is displayed as a black solid line, while the 1-σ dispersion is the gray-filled area. We highlight the two galaxies part of our sample COS2987 and CRISTAL-5, respectively at z = 6.8 and z = 5.54.

While the majority of the galaxies at high redshift appear to lie on this MS relation, a major focus of galaxy evolution studies has been to understand how galaxies move in and out of the sequence, and how major mergers result in starbursting activity and subsequently in quenching of star-formation in galaxies (Genzel et al., 2015; Tacconi et al., 2018). We show in the right panel of Figure 1.6 this relationship for typical star-forming galaxies at z = 4-6 (Faisst et al., 2020). We highlight the high-redshift galaxies COS2987 and CRISTAL-5, located respectively at z = 6.8 and z = 5.54. These galaxies, which compose our study sample (see Chapter 2 and 3), lie within the 1-σ dispersion of the relation, and thus they are classified as main-sequence galaxies. Therefore, our results, detailed in the forthcoming chapters, can provide valuable comprehension of the properties of the typical population of galaxies which directly affect the evolution of the cosmic star formation density.

1.2.4 THE HISTORY OF STRUCTURES IN GALAXIES

If you want to know a galaxy, start looking at it. The morphology is one of the fundamental properties in galaxy evolution, as the shape tracks how matter is distributed across a galaxy.

Moreover, it is the primary indicator of galactic evolutionary history, since the intricate physical mechanisms and gravitational events that affect the large-scale structure imprint peculiar shapes in the matter distribution. For example, when dynamical events and internal processes (such as mergers and outflows) occur, galaxies get disrupted and distorted (Nelson et al., 2019; Pillepich et al., 2019).

At low-redshift, the diversity of shapes of low-redshift galaxies correlates with several physical properties such as the stellar mass, star formation histories, and environment (Baldry et al., 2004; De Lucia et al., 2006; Poggianti et al., 2010; Tojeiro et al., 2013). Local early-type galaxies (namely ellipticals and lenticulars) are in general more massive, have little to no star formation and relatively old stellar populations (Baldry et al., 2004), while late-type galaxies (namely disks and irregulars) have a considerable amount of star formation, and mixed stellar populations (Baldry et al., 2004; Faber et al., 2007). Moreover, elliptical and lenticular galaxies reside preferentially in regions of very high local density, populating especially the cores of clusters and groups, while spiral galaxies inhabit field regions (Dressler, 1980; Postman et al., 2005).

The search for understanding when these different types of galaxies emerge is an active field, which is giving new steps after the launch of JWST. The first studies of the spatial distribution of high-redshift galaxies relied on rest-UV imaging from the Hubble Space Telescope (HST), as it was the only instrument that provides sufficiently high spatial resolution and depth to reveal the inner structures of small galaxies at these wavelengths. Such observations reveal that galaxies at $z > 2$ are clumpy and irregular, indicating high merger rates (Elmegreen & Elmegreen, 2005; Conselice & Arnold, 2009; Duncan et al., 2019; Shibuya et al., 2022), also a direct consequence of the hierarchical model of galaxy growth. A galaxy merger is the event of a close encounter of two or more galaxies under the gravitational forces of each one, that eventually causes them to combine into a larger, more massive single object. Visually, interactions can be identified by multicomponent systems with distorted shapes, bridges, and tidal tails. The final product depends directly on the mass ratio between the galaxies: in a major merger, both galaxies have comparable masses and the tidal forces destroy the individual internal structures. In a minor merger, one galaxy is considerably more massive than the other and the interaction ends up with the accretion of the less massive satellite galaxy. Currently, the most acceptable scenario for the formation of elliptical galaxies is quenching after a merger of disk galaxies that completely disrupt their original structures (Hopkins et al., 2006).

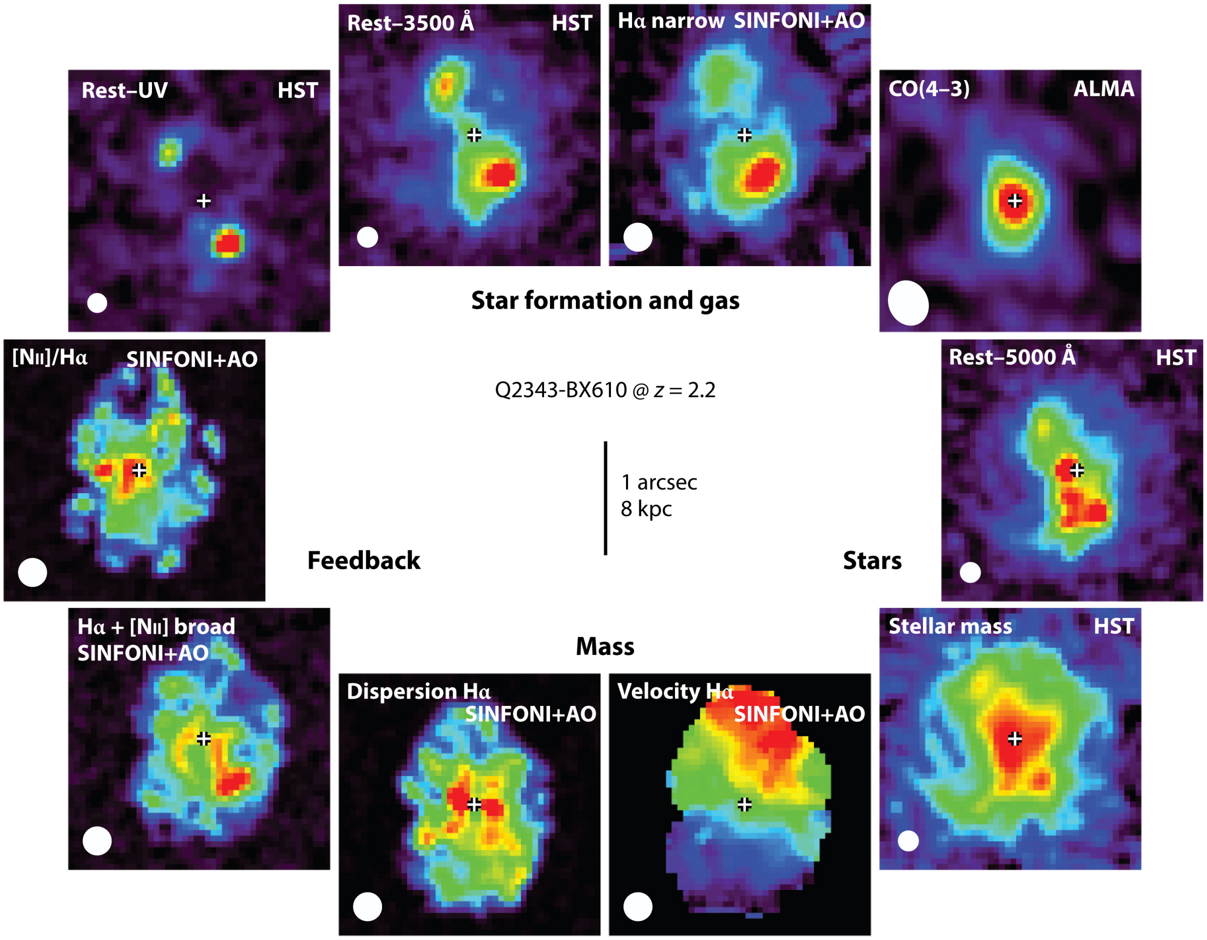

Förster Schreiber NM, Wuyts S. 2020.
Annu. Rev. Astron. Astrophys. 58:661–725

Figure 1.7: Multi-wavelength cutout postage stamps toward Q2343-BX610. Image credit: Förster Schreiber & Wuyts (2020)

Alternatively, the disk formation is the direct consequence of cold mode gas accretion (Dekel et al., 2009; van de Voort et al., 2011), an important mechanism of gas supply. This gas comes from the filamentary highways of the intergalactic medium, and up to date, there is little observational evidence of these features (Rauch et al., 2011; Daddi et al., 2021, 2022; Emonts et al., 2023). This gas supplementation happens in a cold mode, meaning that they travel through cold streams being heated to temperatures much lower than the virial temperature of the galaxy. As this gas is accreted, the conservation of the angular momentum (from tidal torques from surrounding large scale structure, Hoyle, 1949) places it in a rotating supported disk. This is believed to transition from a thick, clumpy, and dynamically hotter disk to a cold thin one in the local universe (Wisnioski et al., 2019; Pillepich et al., 2019).

One of the main challenges to tracking when these different galaxy shapes arrises is that high-redshift galaxies are distant, fainter, have smaller angular sizes, and suffer from cosmological dimming which makes detecting subtle features difficult. Besides, just like in local galaxies, the tracer of the matter distribution choices can affect significantly the final morphological classification, and thus the understanding of the dynamical state of the system. We exemplify how the morphological classification is tricky in Figure 1.7, as we show multi-wavelength cutout images of the galaxy BX610, at z = 2.2 (Förster Schreiber & Wuyts, 2020). Only by analyzing the rest-UV images, one would classify the BX610 system as two galaxies in a close encounter. However, stellar tracers such as rest-5000Å images reveal that the double sources are star-forming clumps of a rotating disk galaxy. Therefore studies at $z > 5$ require access to the morphology of different components of a galaxy so that a reliable classification can ultimately be made.

1.3 OUTLINE OF THIS THESIS

In this thesis, we aim to provide new insights into the mechanisms responsible for galaxy assembly in the early Universe through high-resolution imaging of the ISM in galaxies at the end of cosmic reionization (z = 5-7). We addressed the following questions:

1. What do early galaxies look like?
2. What are the physical drivers of galaxy growth in the early universe?
3. Are rotating disks dynamically hotter at high redshift? What is causing the high turbulence?
4. What is producing the [C II] emission in high-redshift galaxies? What is the origin of the [C II] halos?

This is organized as follows: In Chapter 2, we explore the structure and dynamics of the galaxy COS2987, a star-forming galaxy at $z \sim 7$. We also discuss the ISM properties derived from resolved measurements of the star formation rate (SFR) and [C ii] surface densities and the implications of our results in the context of cosmic evolution of the intrinsic velocity dispersion of rotating disks. This chapter was published as: "Structure and kinematics of a massive galaxy at z $\sim$ 7" (Posses et al. 2023, 669, A46, 20). In Chapter 3, we describe a similar study case at galaxy CRISTAL-05 , at z = 5.54. We also analyze the structure and dynamics of [C ii] emission and compare it to the rest-UV and optical emission. We particularly investigate the cause of [C ii] extended emission in this galaxy. Finally, in Chapter 4 we summarize the conclusions and final remarks of the projects. We discuss the immediate future steps to keep investigating the galaxy evolution of these early sources.

CHAPTER 2

STRUCTURE AND KINEMATICS OF A MASSIVE GALAXY AT Z $\sim$ 7

The content of this chapter is published in the journal Astronomy & Astrophysics (A&A), see Posses et al. (2023).

2.1 INTRODUCTION

The early stages of the build-up of galaxies are thought to be marked by gas accretion from the intergalactic medium (IGM) as well as from episodes of major galaxy mergers (Kereš et al., 2005a; Hopkins et al., 2006; Dekel et al., 2009; Bournaud et al., 2011). These processes provide the fuel for star formation, which is regulated by stellar and AGN feedback (Heckman et al., 2000; Hopkins et al., 2008; Silk, 2013; King & Pounds, 2015). Furthermore, the far ultraviolet (FUV) photons produced by the first stars and early galaxies could ionize the previously neutral IGM. These effects ultimately led to the era of so-called cosmic reionization, which is believed to have taken place at $z \sim 20-6$ (Robertson et al., 2015).

Normal star-forming galaxies in the early universe ($z \sim 8-6$), located close to the knee of the UV luminosity function, are expected to be sufficiently abundant and produce enough ionizing photons to play an important role in the process of cosmic reionization (Dayal et al., 2020; Naidu et al., 2020). Thus, describing the physical properties and mechanisms of assembly of these early systems, through morphological and dynamical studies, remains a fundamental step to understanding the formation and evolution of galaxies, as well as how these sources influenced the evolution of the universe.

In the last few decades, a large number of studies have taken advantage of high-angular resolution optical and near-infrared images to investigate the structure of $z > 6$ galaxies. The Hubble Space Telescope (HST) images, which at these redshifts trace the rest-frame UV emission and, thus the star-forming component of such galaxies as well, have mostly shown (multi-component) clumpy structures, likely indicating an early stage of mass assembly (Capak et al., 2015; Carniani et al., 2018a,c; Bowler et al., 2017; Matthee et al., 2017, 2019; Le Fèvre et al., 2020). The rest-frame UV radiation, however, might be affected by dust obscuration, which can lead to patchy geometry, thereby preventing us from acquiring a reliable picture of the galaxy structures. Observations of the different components of galaxies, including star formation processes, the stars themselves, and the cold interstellar medium (ISM) at wavelengths not affected by dust obscuration, are thus necessary to provide a full description of the galaxy structures and the related mechanisms involved in galaxy growth (Förster Schreiber & Wuyts, 2020).

The Atacama Large Millimeter/submillimeter Array (ALMA), thanks to its great sensitivity and angular resolution, has opened a new window on the distribution of the cold ISM by exploring the far-infrared regime through dust continuum and fine-structure emission lines. In particular, the $^2P_{3/2}$—$^2P_{1/2}$ transition of the singly ionized carbon atom (hereafter [C II] ; centered at 158μm) is one of the brightest cooling lines[1] in the far-infrared regime (Stacey et al., 1991, 2010) and a tracer of multiple gaseous phases (cold molecular, neutral, and ionized gas associated with photon-dissociation regions; Wolfire et al., 2003; Vallini et al., 2015; Clark et al., 2019).

At $z > 2$, the [C II] emission line shifts into the (sub)millimeter atmospheric windows, which are widely accessible from the ground, thus making it a flagship focus of ISM studies of early galaxies. In recent years, a plethora of [C II] line detections has been reported (e.g., Capak et al., 2015; Willott et al., 2015; Harikane et al., 2018; Smit et al., 2018; Carniani et al., 2018a), including those carried out by the ALPINE (Le Fèvre et al., 2020) and REBELS (Bouwens et al., 2021) ALMA large programs that are specially designed to provide [C II] line measurements for normal star-forming galaxies at $z = 4 - 6$ and $z = 6 - 9$, respectively. While the number of

---

[1] Due to its low ionization potential of 11.3 eV

[C II] detections has increased rapidly (mostly at $\sim 1''$ resolution), only a few observations to date have been able to resolve the [C II] emission at $z > 4$ to enable the characterization of the galaxy's structures and kinematics (Neeleman et al., 2020; Rizzo et al., 2020; Lelli et al., 2021; Herrera-Camus et al., 2021; Rizzo et al., 2021).

The wealth of relatively low-resolution (i.e., $\sim 1''$) observations have shown complex [C II] structures, revealing clumpy, irregular ones in some cases (Inoue et al., 2016; Matthee et al., 2017; Carniani et al., 2018a,c), as well as regular velocity fields in others (Fig. 3 in Smit et al., 2018; Neeleman et al., 2020). In some systems, the brightest regions in [C II] and UV emission do not spatially match, while in others, the presence of [C II] (UV) clumps with no UV ([C II]) counterparts has been reported (Capak et al., 2015; Fujimoto et al., 2020). In a similar vein, several objects display extended [C II] emission when compared to the UV component. It is still unclear what the cause behind this difference is, but some possible explanations include differential dust obscuration, outflows, and infalling satellites (Fujimoto et al., 2019, 2020).

In this paper, we report sensitive ALMA high-resolution [C II] line observations of the typical star-forming galaxy COS-2987030247 (hereafter, COS2987) at $z = 6.8076$. This system was a $z \sim 7$ Lyman-break galaxy candidate with a high [OIII]+Hβ equivalent-width (EW) obtained from optical to infrared spectral energy distribution (SED) modeling (Smit et al., 2015; Laporte et al., 2017), which was later confirmed to be a gas-rich star-forming galaxy based on the detection of its bright [C II] line with ALMA (Smit et al., 2018). Dynamical analyses of the [C II] line velocity field in low-resolution observations ($1.1''$x$0.7''$, translated to 5.8×3.7 kpc at z = 6.8), have suggested that disk rotation could be in place (Smit et al., 2018). Here, we analyze the morpho-kinematic properties of this galaxy and its close environment in detail.

In Section 2.2, we describe the general properties of our target, as well as the ALMA observations. In Section 2.3, we analyze the structure and spatial extension of the [C II] and UV emission, along with a dynamical analysis. In Section 2.4, we discuss the ISM properties derived from resolved measurements of the star formation rate (SFR) and [C II] surface densities. We discuss the implications of our results in the context of the cosmic evolution of the intrinsic velocity dispersion of rotating disks. In Section 2.5, we list the main results. We assume a standard ΛCDM cosmology with: Ω_Λ =0.7, Ω_M =0.3, $H_0 = 70$ km s^{-1} Mpc^{-1} throughout the paper, leading to a physical conversion of 5.312 kpc/$''$.

2.2 DATA

2.2.1 TARGET

COS2987 is a star-forming galaxy located at $z = 6.8076 \pm 0.0002$ (Smit et al., 2018). It was initially detected as a Lyman-break galaxy by Smit et al. (2015) in the CANDELS/COSMOS field (Scoville et al., 2007; Koekemoer et al., 2011). Rest-frame UV to far-infrared observations, as well as SED modeling, indicate a massive star-forming galaxy, located within the expected main sequence of star formation at this redshift, and low dust content due to a non-detection of dust continuum emission (Smit et al., 2018). The multi-wavelength SED (including 4.5μm Spitzer/IRAC band) yields a stellar mass of $1.7^{+0.5}_{-0.2} \times 10^9 \mathrm{M}_\odot$ (Smit et al., 2018). Measurements of Lyman-α line emission indicate a broad and strong emission compared to other sources at the same redshift (Laporte et al., 2017). .

Smit et al. (2018) identified tentative evidence that the galaxy is a rotating system based on the detection of the [C II] line emission using ALMA observations at $\sim 0.8''$ resolution (PI: Smit, ALMA ID: 2015.1.01111.S). This finding makes the galaxy a unique target for confirmation of its dynamical state, given that most systems at $z > 5$ showed clumpy irregular morphology (Capak et al., 2015). The main physical properties of COS2987 from the literature as well as those derived from this work are listed in Table 3.2.

2.2.2 ALMA OBSERVATIONS

ALMA observations were obtained during Cycle 5 in the C43-5 configuration with 43 antennas, (PI: Aravena, PID: 2018.1.01359.S), with 3.6 hours of on-source integration time. The ALMA band 6 receivers were used to target the redshifted [C II] line emission at 243.3465 GHz. Observations were taken with four spectral windows (SPWs), each with a total bandwidth of 1.875 MHz, and a native channel resolution of 7.813 MHz (≈ 9.6 km s^{-1}). One of the SPWs was centered on the [C II] emission line and the rest of the SPWs were used to measure the underlying continuum emission.

We combined the new ALMA Cycle 5 data with previous lower-resolution observations from the original [C II] detection (PID: 2015.1.01111.S; Smith et al. 2018). These observations took 24 minutes of on-source integration. These data add important information on shorter baselines, which are sensitive to extended emission. The lower and higher resolution data sets were calibrated with the Common Astronomy Software Applications package pipeline (CASA; McMullin et al., 2007), using versions 4.5.3 and 5.4, respectively. The quasar J0948+0022 was used as the phase calibrator for both observations, while J1058+0133 and J0854+2006 were chosen as amplitude calibrators for the previous and latest data sets, respectively. No additional flagging was deemed necessary given the good quality of the observations.

We employed the *tclean* task to generate a continuum image and a data cube for the SPW containing the [C II] emission line, using natural weighting to preserve sensitivity. To obtain a continuum image, we used all the channels in each SPW, excluding the ones within the velocity range [-250, 250] km s^{-1}, centered at the line. For the cube, we binned the data to a channel resolution of 30 km s^{-1}, which is a compromise between the sensitivity and velocity resolution. The cleaning was done interactively until no significant emission was left in the residual. Since no continuum emission was detected, we did not perform a continuum subtraction in the uv plane. This procedure yielded a noise level of 6 μJy beam^{-1} and 0.134 mJy beam^{-1} for the continuum image and line cube, respectively, and a synthesized beam size of $0.44'' \times 0.35''$ (PA= 50 deg; natural weighting). This scale translates into a physical size of 2.3×1.8 kpc^2, at z = 6.8. The angular resolution obtained for previous observations of this galaxy is about two times coarser: $1.07'' \times 0.72''$, corresponding to 5.7×3.82 kpc^2 (Appendix A.1).

2.2.3 ANCILLARY DATA

We used the F160W-band image ($\lambda_{\text{rest-frame}} \sim 2050$ Å) obtained with the Wide Field Camera 3 (WFC3) of the HST from the CANDELS survey (PI: Sandra Faber, ID: 12440). It yields a view of the rest-frame near-UV emission at the redshift of the source. Rest-frame UV images are also available from the F125W-band (Koekemoer et al., 2011). We chose the F160W-band for the spatial analysis, mostly for consistency with the analysis conducted by Smit et al. (2018) . The F125W-band was employed to measure the SFR since it represents a rest-frame far-UV regime ($\lambda_{rf} \sim 1600$ Å). Both F160W and F125W images have a point spread function (PSF)

Table 2.1: Observational and physical properties of COS2987

Property	Value	Reference
Right Ascension	+10:00:29.86	2
Declination	+02:13:02.19	2
$z_{\text{[CII]}}$	6.8076 ± 0.0002	1
SFR_{UV} ($\text{M}_\odot$ yr^{-1})	16 ± 9.0	2
SFR_{IR} ^{a} ($\text{M}_\odot$ yr^{-1})	≤ 1.7	2
Stellar mass (10^9 $\text{M}_\odot$)	$1.7^{+0.5}_{-0.2}$	2
β_{UV}	-1.18 ± 0.53	1
S/N ([C II])	8.4σ	2
[C II] line flux (Jy km s^{-1})	0.15 ± 0.02	2
$\text{FWHM}_{\text{[CII]}}$ (km s^{-1})	126 ± 16	2
$S_{158\mu\text{m}}$ ^{a} (μJy)	≤ 18	2
$\text{L}_{\text{[CII]}}$ (10^8 $\text{L}_\odot$)	1.6 ± 0.2	2
L_{FIR} (10^{10} $\text{L}_\odot$)	$\leq$1.15	2
$\text{r}^{eff\ b}_{\text{UV}}$	$0.31''^{+0.06}_{-0.05}$	2
$\text{r}^{eff\ b}_{\text{[CII]}}$	$0.38''^{+0.02}_{-0.02}$	2
v_{rot} (km s^{-1})	86 ± 16	2
v_{disp} (km s^{-1})	≤ 30	2
Conversion (kpc/”)	5.312	

Notes: Values derived in this work were obtained in the region containing the main central source C with a 0.5″-aperture; see Section 2.3.1. ^{a} 3-σ upper limit,^{b} Considering an exponential radial profile (Sérsic index = 1.0); References: [1] Smit et al. (2018) and [2] This work.

of 0.18″, a pixel scale of 0.06″/pix, and have been astrometrically matched to the Gaia DR2 release (Gaia Collaboration et al., 2018).

2.3 RESULTS

2.3.1 SPATIAL DISTRIBUTION

We analyzed the spatial distribution of the rest-frame UV emission, traced by the HST F160W-band image, and the [C II] line emission from ALMA, in the left panel of Figure 2.1. We find a good match between the spatial distribution of both emissions, particularly in the central region

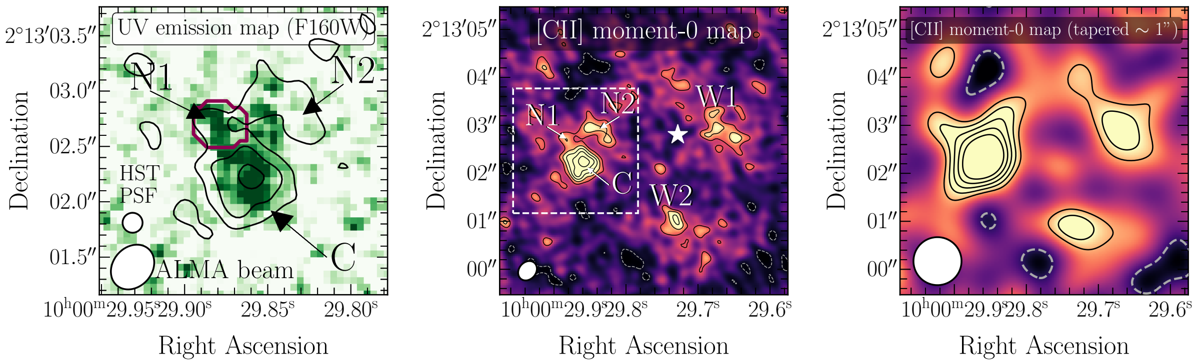

Figure 2.1: Rest-frame UV and [C ɪɪ] line maps of the galaxy COS2987 and its surroundings. **(a) Left:** HST F160W-band image in the background shows the rest-UV emission in a 1.3″ ×1.3″ region around the galaxy. The [C ɪɪ] integrated map (moment-0) is overlaid as black contours shown at 2-, 4- and 6-σ, where σ is the rms noise level of the moment-0 map. The region containing the foreground galaxy identified by Laporte et al. (2017) is highlighted by the purple line. **(b) Middle:** Zoom-out version of the [C ɪɪ] moment-0 map toward COS2987 (6″ x 6″). The region shown in the left panel is represented by the dashed white line. We marked the locations of the central source (C), north-east emission (N1), north-west arm (N2), west emission (W1), and south-west emission (W2). The black contours represent the integrated [C ɪɪ] line emission at 2-, 3-, 4-, 5-, and 6-σ levels and the dashed white contour represents the -2-σ level. The white star corresponds to a galaxy observed in the F160W-band map at $z_{phot} = 1.73$ (Laigle et al., 2016).**(c) Right:** [C ɪɪ] line integrated map tapered to a 1″ beam size, showing the same region as in the central panel. The black contours represent the 2-, 4-, 6-, 8-, and 10-σ levels and the dashed white contour represents the -2-σ level.

where most of the [C ɪɪ] emission is detected. There is a small offset of 0.118″ (corresponding to 0.628 kpc) between the centroids of UV and [C ɪɪ] emissions, which is less than the HST PSF and the ALMA beam size. Hence, we do not find any divergent locations for the UV and [C ɪɪ] emission, as it has been observed in other objects at similar redshifts. We refer to this central region as the ‘C’ component in the left and central panel of Figure 2.1. A 0.5″ -circular aperture photometry reveals a [C ɪɪ] line flux of 0.15 ± 0.02 Jy km s^{-1}, which corresponds to an 8.4σ detection.

To the north of C, we find two clumpy structures traced by both the UV and [C ɪɪ] emissions. One of them extends to the north-east, referred as "N1," and the other resembles an arm-shaped structure to the north-west, labeled as "N2." Component N1 is located 0.60″ north-east from C (measured at the centroids of C and N1 in the [C ɪɪ] image), while N2 is located at 0.73″ north-west from C. This corresponds to a projected physical distance of 3.2 and 3.9 kpc for N1 and N2, respectively. Given the moderate significance of each of these structures, we performed aperture photometry to measure their individual [C ɪɪ] fluxes. We find that N1 and N2 have

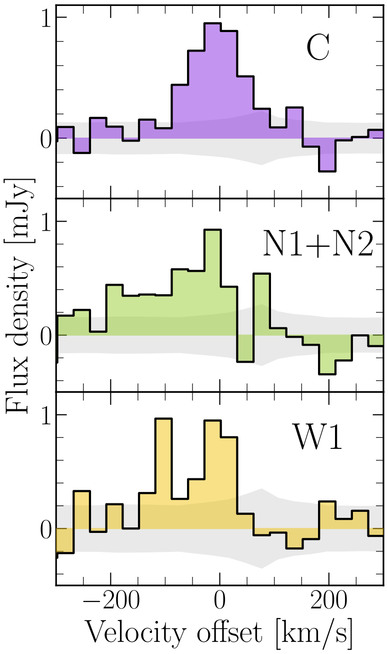

Figure 2.2: Spectra ranging from -300 to 300 km s^{-1} centered at the [C ii] observed-frame frequency at z = 6.8076 (243.3465 GHz), based on a channel resolution of 30 km s^{-1}. The gray region corresponds to the rms per channel. The spectra represent the: **(a) Upper panel:** Central source C; **(b) Central panel:** N1+N2 emissions; and **(c) Bottom panel:** West emission. The regions are marked in Figure 2.1.

integrated [C ii] line fluxes of 0.02 ± 0.01 Jy km s^{-1} and 0.07 ± 0.02 Jy km s^{-1}, yielding significances of 2.2σ and 4.1σ, respectively (Appendix A.2). We highlight the fact that these components were not seen by Smit et al. (2018), mainly because of the lower depth, and were likely blended with the main source.

Laporte et al. (2017) indicated that the rest-UV source associated with N1 corresponds to a foreground galaxy at $z_{\rm spec} = 2.099$. Based on this, and given that the candidate [C ii] emission is of low significance, we consider it as a foreground object. Thus, for further analysis, we mask out the region within N1, which corresponds to the purple contour in the left panel of Fig. 2.1. In the case of N2, the significance of the [C ii] line emission and its extended structure suggest that this is associated with the main galaxy C at z $\sim$ 7. The F160W-band image also shows an extended UV emission in the north-west of the central galaxy C, but not perfectly colocated to N2.

To check for the existence of other emitting regions at the redshift of the main galaxy, we searched for [C II] emitters in the wider field of the ALMA [C II] map (Fig. 2.1, center). Two other sources are identified as candidate [C II] line emitters to the west and south-west of COS2987 (labeled as W1 and W2, respectively). They are located at 15 kpc and 12 kpc from the central source C, with flux densities of 0.10 ± 0.03 Jy km s^{-1} ($\sim 5.2\sigma$) and 0.06 ± 0.02 Jy km s^{-1} ($\sim 3.6\sigma$), respectively. We only found a UV counterpart in the F160W image (Appendix A.1) to source W1, located at $0.95''$ from the peak [C II] emission and marked as a white star in Fig. 2.1 (central panel). It is consistent with a photometric redshift of 1.73 based on the COSMOS2015 catalog (Laigle et al., 2016). The lack of a counterpart for W2 supports the fact that the candidate [C II] positive signal is spurious. Furthermore, the significant distance between the UV counterpart to W1 and the conflicting photometric redshift of this source imply either that this is not the actual counterpart, in which case the [C II] emission might be real but without a UV counterpart, or that the candidate [C II] line is a noise feature. The spectra centered at the [C II] observed frequency of C, N1+N2 and W1 are shown in Figure 2.2.

A $1''$-tapered map (to maximize the extended emission significance of the emitters; Fig. 2.1, right) reveals a tentative detection of the clumps, but the low significance of W2 and N2 requires deeper observations to confirm or discard the sources. Finally, we performed two extra tests to check the reliability of the candidates. We started by splitting the visibility data into two different groups of observing scans (both containing scheduling blocks from the previous and latest data), and recreated the [C II] cubes and maps. We could recover sources N2 and W1, but we were not able to locate W2 in both maps, indicating that the latter is likely to be the product of a noise pattern. Secondly, we explored the moment-0 maps with different weightings and taperings to exclude the possibility that the four candidates are artifacts generated by the side-lobes of the beam. The candidates become fainter in the moment-0 maps, particularly when we use uniform parameters below 1. Nevertheless, as we combine the standard Briggs weighting with a uniform parameter of 0.5, and taper the visibilities, the N2 and W1 candidates still remain with moderate significance. Deeper observations will be key to ultimately confirming or rejecting the reality of these surrounding candidates' sources.

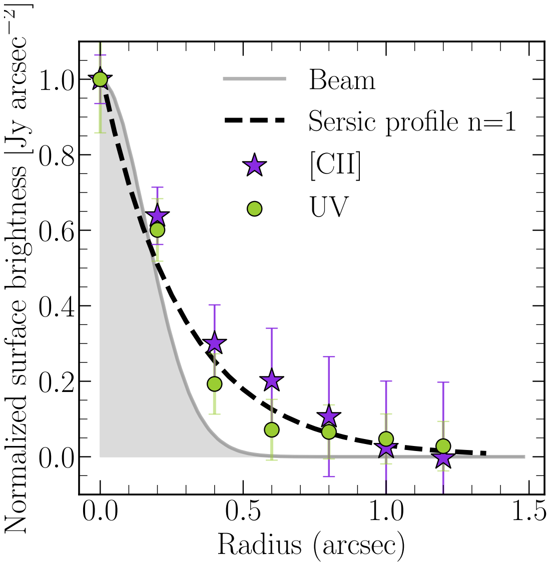

Figure 2.3: Radial profile of the surface brightness of the UV continuum (green circles) and [C II] line (purple stars). Each map is convolved with the PSF/beam of the other image to match the resolution of $0.47'' \times 0.40''$. There is no detection of a dust continuum, therefore no radial profile is shown. As a reference, we added the radial profile of the convolved beam and an exponential profile (Sérsic index = 1) with a $r_{eff} = 0.38''$ as a solid gray line and dashed black line, respectively.

2.3.2 RADIAL PROFILE AND SIZES

We aimed to quantify whether the ISM component traced by the [C II] line emission has a similar spatial distribution to the star-forming component traced by the rest-UV emission. Thus, we measured their effective sizes and compared their radial profiles. We first fit a two-dimensional (2D) Sérsic profile (Sérsic, 1963) to the [C II] brightness distribution in the moment-0 map and UV map using a Markov chain Monte Carlo (MCMC) approach (see Appendix A.3). The Sérsic profile is mainly composed of two parameters: the Sérsic index, n, which describes the curvature of the profile, and the effective radius, $r_{\rm eff}$ defined as the radius at which half of the total brightness was emitted. We convolved the intrinsic and not inclination-corrected model with the synthesized beam before making a comparison with the moment-0 map. We obtained a consistent radial profile distribution with $n_{\rm [CII]} = 1.62^{+0.59}_{-0.43}$ and $r_{\rm eff,[CII]} = 0.47''^{+0.12}_{-0.07}(\sim 2.3$ kpc), but with a largely unconstrained $n_{\rm UV}$, possibly due to the faint data. When we set $n = 1$, we found a compatible effective radius for both components: $r_{\rm eff,[CII]} = 0.38''^{+0.02}_{-0.02}$ ($\sim$ 2 kpc) and $r_{\rm eff,F160W} = 0.31''^{+0.06}_{-0.05}$ ($\sim$ 1.6 kpc). In our further analysis, we stick with n = 1 to maintain consistency with other analyses in the literature (Fujimoto et al., 2020)

COS2987 has one clear component extending to the north-west (N2), as suggested by both the [C II] and rest-UV maps. This prompted us to compare the extension of the [C II] and rest-UV emission in the source (C + N2) and thus check for an extended [C II] halo. We measured the radial surface brightness profile in concentric rings as a function of radius. This procedure is not available for the dust component of the galaxy, since there is no detection of the continuum emission.

Since the ALMA [C II] and F160W rest-UV maps have different angular resolutions, we followed the procedure described in Fujimoto et al. (2020). We convolved the ALMA (HST/F160W) image with the HST/F160W (ALMA) PSF, generating a resolution of $0.47'' \times 0.40''$, which translates to 2.5×2.1 kpc^2 in physical size. For each image, we computed the surface brightness measuring the [C II] and rest-UV flux in $0.2''$-width rings, covering the region from the central peak to the end of the N2 structure. As stated in the previous section, there is a foreground galaxy located to the north-east (N1) of the central source. Thus, we masked the pixels corresponding to this structure in both the ALMA and HST/F160W images. However, given its faintness, the choice of whether or not we include this region reveals no significant difference in the resulting radial profile.

The [C II] and rest-UV emission radial profiles are shown in Fig. 2.3 and they are in good agreement within the uncertainties. There is a slight increase in [C II] emission for the region closer to the north arm N2 ($r \sim 0.6$”), however, it does not represent a substantial difference compared to the rest-UV. We find that the [C II] emission in this case closely follows the rest-UV emission, in shape and size. Since we do not recognize major differences between the [C II] and rest-UV profiles, we conclude that COS2987 does not contain a particularly extended [C II] emission or a [C II] halo.

2.3.3 DYNAMICAL ANALYSIS

Based on low-resolution ALMA [C II] line imaging, Smit et al. (2018) identified a tentative velocity gradient suggesting that a rotating disk is in place in this galaxy. Thus, we analyzed the current dynamic state of COS2987 based on our higher-resolution data. Figure 3.4 shows

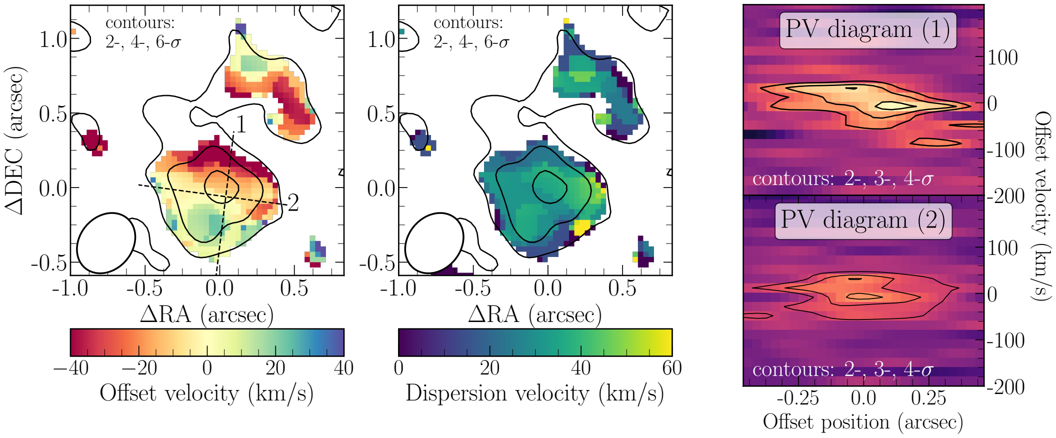

Figure 2.4: Velocity (Moment-1) and dispersion (Moment-2) maps of the galaxy COS2987 (with respect to the observed frequency of [C II] at redshift $z = 6.8076$) are shown in the left and right panels, respectively. The black contours correspond to the 2-, 4-, 6-σ levels of the [C II] integrated (moment-0) map. In the right panel, we plot the position-velocity diagram of slits 1 and 2, shown on the left panel as dashed lines. The black contours correspond to the 2-, 3-, and 4-σ levels of the position-velocity diagram.

the velocity field and dispersion maps (in the left and central panels, respectively) of the central source (C) and north arm (N2). These maps were generated considering the pixels with fluxes above 2 × the rms per channel from a cube with a channel resolution of 30 km s^{-1}. We also only display pixels with a [C II] emission significance greater than 2.5-σ in the moment-0 map. The N2 structure does not show a clear trend, due to its fainter nature. Conversely, we confirmed a north-south velocity gradient across the central source (C). The velocity dispersion map is fairly homogeneous, with a low mean dispersion of 29 km s^{-1} and a scatter of 12 km s^{-1}. The position-velocity diagram along the major axis of the velocity field (top right panel of Fig. 3.4) suggests a tentative pattern typical of rotating disks, as an increase of the radial velocity with the distance to the center of the galaxy and a flattening after a certain radius. However, this cannot be confirmed due to the limited sensitivity of the observations.

We performed a dynamical modeling of our data cube with the ^{3D}BAROLO code (Di Teodoro & Fraternali, 2015). If we assume that COS2987 has a rotating gaseous disk, the modeling retrieves the kinematic parameters of the galaxy, such as the rotational and dispersion velocities. We discuss some of the scenarios that could lead to a gradient in the velocity map in Section 2.4.3.

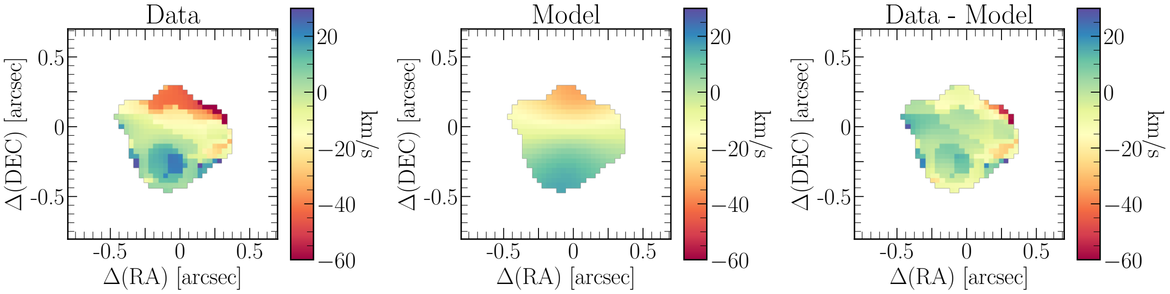

Figure 2.5: Rotational velocity products of the tilted-ring model fitting obtained using ^{3D}BAROLO . The maps are shown in the velocity range of [-60,30] km s^{-1} with respect to the observed frequency of the [C II] line at $z = 6.8076$ **(a) Left:** Observed velocity map of COS2987. **(b) Middle:** Velocity map of the best-fit model with an inclination of $i = 23$ deg. **(c) Right:** Residuals of the velocity map.

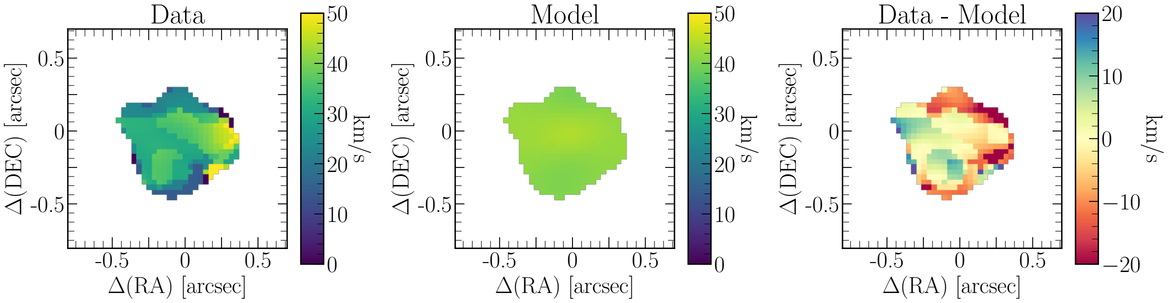

Figure 2.6: Dispersion velocity products of the tilted-ring model fitting obtained using ^{3D}BAROLO . The left and central maps are shown in the velocity range of [0,50] km s^{-1} and the left map in the velocity range of [-20,20] km s^{-1}, with respect to the observed frequency of the [C II] line at $z = 6.8076$ **(a) Left:** Observed dispersion velocity map of COS2987. **(b) Middle:** Dispersion velocity map of the best-fit model with an inclination of $i = 23$ deg. **(c) Right:** Residuals of the dispersion velocity map.

^{3D}BAROLO is based on a tilted-ring model in the case of a galaxy disk. It divides the model into a given number of concentric rings to provide a fit to the observed data cube, taking into account the three spatial and three velocity dimensions. To construct the model, initial guesses of all the parameters need to be provided: the disk position angle, central position of the disk, systemic velocity of the system, radial and rotational velocity, dispersion velocity, inclination, and thickness of the disk. This disk model is then convolved to the original data beam size so that the degraded product can reproduce the real data; the code can thereby deal with effects due to the resolution, such as beam smearing. The initial iterations begin in the inner annuli and if the parameters reproduce the data well, the code steps up to the next annuli. Otherwise, it updates the parameters until it finds the best fit.

We applied this modeling to the [C II] data cube. Using channel resolution higher than 30 km s^{-1}, the performance of the fitting routine failed due to the low signal-to-noise per channel. We considered as a detection per channel any emission with intensity equals to or greater than 0.2 mJy $beam^{-1}$ (2× the mean rms per channel). We also masked the region to consider pixels with significances above 2.5 × the rms of the moment-0 map. We fixed the central position (x_0,y_0) on the centroid of the emission in the moment-0 map. The moment 1 map indicates a velocity gradient tilted by nearly 180 deg from the negative y-axis, so we set this value as an initial guess position angle, and we allowed it to vary between $170-190$ deg. We let the systemic velocity as a free parameter since the peak of the line emission seems to be offset by $\sim$ -10 km s^{-1} from the [C II] observed frequency. We also fixed the radial velocity at 0 km s^{-1} since the depth and resolution cannot allow for the detection of outflows from stellar or AGN feedback. As a final step, we let the code run in three concentric rings, with a width of $0.18''$. It satisfactorily covers the central source and excludes the north-arm region.

As often pointed out by previous studies (Rizzo et al., 2020; Fraternali et al., 2021), the initial inclination has a crucial influence on the best-fit model. Therefore, we performed trial-and-error tests with initial inclination guesses ranging from 0 deg to 90 deg and calculated the residuals (|data - model|, weighted by the moment-0 map) in the velocity and dispersion maps. The residuals are lowest when we consider low inclination values (Appendix A.4). The galaxy has a close-to-round shape, which likely means that it is close to a face-on configuration. Using these criteria, the galaxy agrees with a system tilted by $\sim$ 15 deg. So, we set as an initial guess an inclination of 23 deg, based on the minimized value found from the velocity and dispersion map.

In Figures 2.5 and 2.6, we show the rotational and dispersion products for the best-fit model. We recovered an average rotational and dispersion velocity of 86 ± 16 km s^{-1} and 26 ± 16 km s^{-1}, respectively. However, we preferred to consider in the following analysis the average velocity dispersion as an upper limit of 30 km s^{-1}, since the data cube channel resolution is greater than the value found by the code. Smit et al. (2018) identified an observed velocity difference of 54 ± 20 km s^{-1}, which is tentatively lower than the average rotational velocity found here. However, such value could be strongly affected by the blending of the central source (C) and north arm (N2) due to the lower resolution of the data.

2.4 DISCUSSION

2.4.1 IR EMISSION

We did not detect any far-infrared (FIR) continuum (Appendix A.1), leading to an upper limit (3σ) for the IR luminosity of $L_{IR}^{3-1100\mu m} \leq 1.15 \times 10^{10}$ $L_{\odot}$, assuming a single-component modified black body (MBB) approach and considering $\beta_{\rm IR} = 1.6$ and $T_{\rm dust} = 53$ K (Eales et al., 1989; Klaas et al., 1997; Bouwens et al., 2020). This infrared luminosity can be translated into $\mathrm{SFR}_{IR} \lesssim 1.7$ $M_{\odot}$ yr^{-1}, for the calibration provided by Kennicutt & Evans (2012) (Kroupa IMF), which is nine times lower than that estimated for the UV emission (see Section 2.4.2). Despite the non-detection of the dust continuum emission, the galaxy shows a red UV continuum slope of β_{UV} = -1.18 (Smit et al., 2018), which indicates some dust absorption. This value is also much redder compared to $\beta_{UV} \sim$ -2, which is the mean value expected for galaxies at z $\sim$ 7 (Dunlop et al., 2013; Bouwens et al., 2014, 2016). This suggests that COS2987 has either a slightly older stellar population than other galaxies at this redshift or is more dust obscured (or both).

The low infrared luminosity points to a lower IR excess ($\mathrm{IRX} = L_{\rm IR}/L_{UV} \leq 0.12$) compared to the upper limit found by Smit et al. (2018). A similar non-detection of dust emission is seen in normal galaxies at z = 5-6 (Capak et al., 2015) and it could indicate a warmer dust, which can underestimate the infrared luminosity based on a MBB approach. It follows the conclusion of Fudamoto et al. (2020) and previous studies, which indicate a fast evolution of the ISM conditions in the first 4 billion years of the Universe. An alternative scenario for the non-detected dust emission is that the galaxy contains dust that is cold enough to be completely diluted by the cosmic microwave background, $T_{\rm CMB}(z = 6.8076) \sim 22\,$K. However, we are limited with regard to our ability to infer how cold the dust needs to make the continuum undetectable at 158μm because this is strongly dependent on the optical depth assumption for the gas.

Finally, the galaxy has a lower-limit line-to-continuum luminosity ratio of [C II]/FIR $\geq$ 0.015, comparable to values found for nearby low-metallicity dwarfs and star-forming galaxies (0.1% - 1%, Herrera-Camus et al., 2018b). A similar finding was obtained for the non-dust-detected normal galaxies at z = 5 - 6 from Capak et al. (2015) (mean log[CII]/FIR ~ -1.75 for the typical upper limits of $L_{IR} \lesssim 10.3$). Such high ratios suggest a lower dust-to-gas ratio or more diffuse clouds than normal galaxies at $z \sim 0$ (or both). Our results for COS2987 further confirm that the dust continuum emission is difficult to detect in galaxies at the Epoch of Reionization, even with the new ALMA sensitive observations. We still need to test the hypothesis that low metallicity or warm and cold dust components are the main culprits for such a lack of detection.

2.4.2 RESOLVED Σ_{SFR} VS Σ_{CII}

In the past decade, a tight correlation between the [C II] luminosity and the total SFR in nearby, un-obscured star-forming galaxies has been established (z $\sim$ 0, De Looze et al., 2011; Herrera-Camus et al., 2015a). The efforts to provide a similar relation for the early Universe reveal that this relation still exists (e.g., Schaerer et al., 2020), but it features a higher dispersion (Carniani et al., 2018a). This suggests that the physical conditions of high-redshift galaxies may vary significantly from galaxy-to-galaxy, affecting how we link the star-forming activity to the ISM conditions. Furthermore, the observed relation of the SFR and [C II] luminosity surface densities in high-redshift galaxies shows an offset from the local relation, indicating a possible [C II] deficiency or a more extended [C II] effective radius with respect to the star-forming components.

We performed a global (integrated) and resolved analysis of the relation between the SFR and [C II] luminosity and surface densities in COS2987. We defined apertures throughout the source and measured the corresponding fluxes (luminosities) in the ALMA [C II] and HST/F125W rest-UV maps. Given the lack of dust continuum detection in our data, we assumed that the SFR is largely dominated by the rest-UV emission and, thus, the $SFR_{tot} \simeq SFR_{UV}$. We used the flux measured in the HST/F125W band as a tracer of the rest-UV emission and converted the corresponding luminosity to SFR using the calibration provided by Kennicutt & Evans (2012) and a Kroupa IMF (Kroupa & Weidner, 2003). For the global measurement, we defined an aperture of 0.5″ radius (2.7 kpc), which roughly corresponds to the size of the central region of the galaxy C (as defined in Section 2.3.1). For the resolved measurements, we divided the

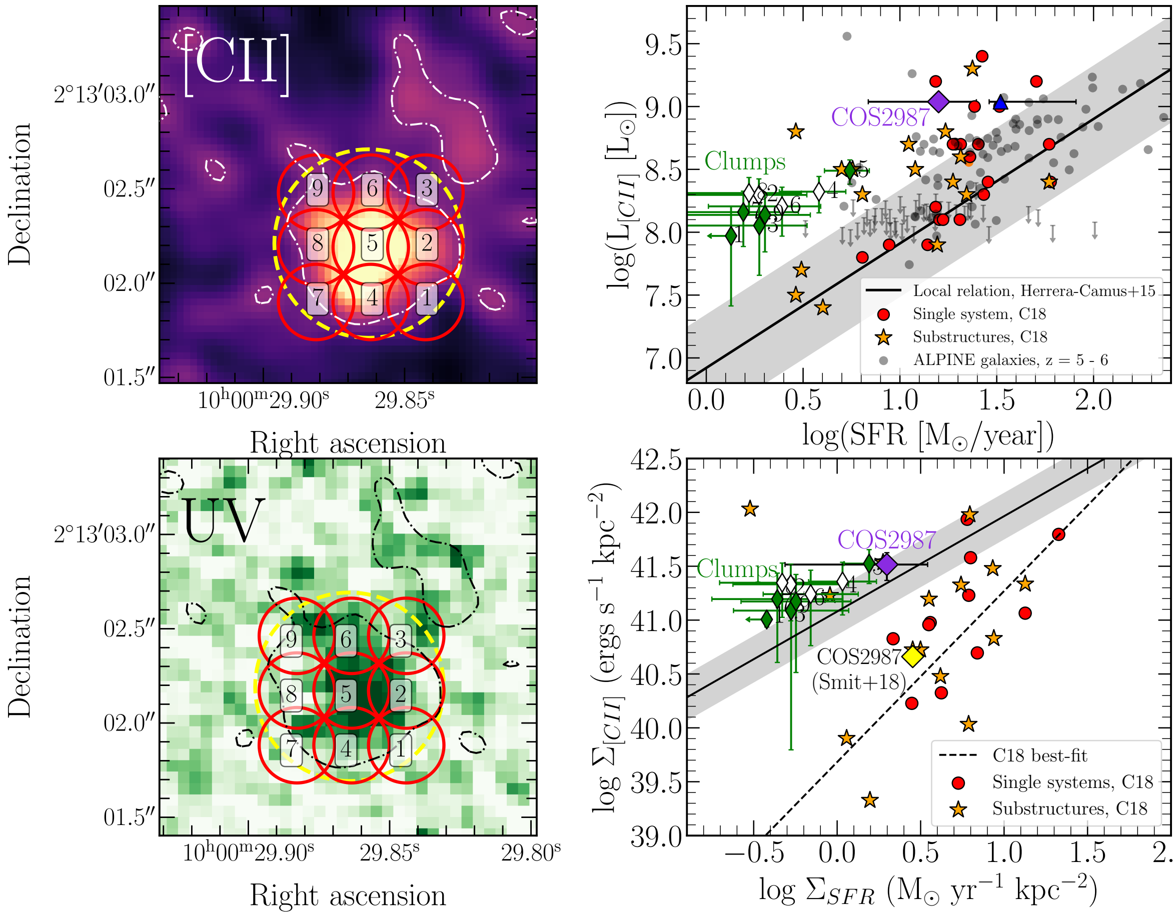

Figure 2.7: $L_{[\mathrm{CII}]}$-SFR and $\Sigma_{[\mathrm{CII}]}$-Σ_{SFR} relations for the galaxy COS2987 and its minor components. (a) Upper-left panel: [C II] moment-0 map with the regions considered as the whole system of COS2987 and its substructures highlighted as a yellow dashed circle and red circles, respectively. The regions within COS2987 are numbers as displayed in the figure. The dashed-dotted white line shows the 2-σ significance level of the galaxy. (b) Bottom-left panel: F125W-band map with the same regions displayed in the upper left panel. The 2-σ significance level of the [C II] moment-0 map is shown as a black dashed-dotted line. (c) Upper-right panel: $L_{[\mathrm{CII}]}$-SFR relation. The single system of COS2987 and its substructures are displaced as a purple diamond and thin green/white diamond, respectively. As a reference, the single system and their corresponding substructures of galaxies at z = 5-6 are represented as red circles and orange stars, similar as the original study (Carniani et al., 2018a). Normal star-forming galaxies from the ALPINE survey (Schaerer et al., 2020) are represented as black circles. The black solid line and filled area describe the best-fit for the distribution of galaxies at z ∼ 0 (De Looze et al., 2014). (d) Bottom-right panel: $\Sigma_{[\mathrm{CII}]}$-Σ_{SFR} relation. The lines and points are the same from the upper right panel, except for the black solid line and filled area that corresponds to the local $\Sigma_{[\mathrm{CII}]}$-Σ_{SFR} relation by (Herrera-Camus et al., 2015a). The dashed black line represents the best-fit for the galaxies and their respective clumps (Carniani et al., 2018a).

source into nine subregions, defined by apertures of a $0.2''$ radius. The central and subregions are labeled from 1 to 9 in Figure 2.7 top and bottom left panels. The circle labeled as 9 corresponds to the foreground galaxy discussed in Section 2.3.1; therefore, we discarded any further analyses for this region.

Figure 2.7 (top and bottom right panels) shows the global (dashed-yellow) and subregion (solid-red) apertures along with the measured $L_{[CII]}$-SFR and $\Sigma_{[CII]}$-Σ_{SFR} relations of these regions. For comparison, we displayed measurements from Carniani et al. (2018a) (C18, in Fig. 2.7) in normal star-forming galaxies at $z = 5-7$ and from Schaerer et al. (2020) in ALPINE star-forming galaxies at $z = 4-6$. In the former case, measurements are provided for the full single systems (represented by red circles in Fig. 2.7) and their clumps (yellow stars), with the SFR defined as $\mathrm{SFR_{UV}}$ + $\mathrm{SFR_{IR}}$ (SFRs of galaxies with no dust continuum detection are defined as SFR $\sim$ $\mathrm{SFR_{UV}}$). For the ALPINE galaxies, only integrated measurements of each galaxy are provided, and the SFRs were obtained by SED fitting.

Our target, COS2987, is shown as a purple diamond, and the resolved measurements as thin diamonds. Since some apertures (labeled as 2, 4, 6, and 8; Figure 2.7, left panels) are overlapped with the central one (labeled as 5) and may have considerable emission from the central region; we separate them in non-filled thin diamonds. The other spatially independent apertures (labeled as 1, 3, 5, 7, and 9; Figure 2.7) are shown as green-filled diamonds. The galaxy lies within the nearby [C II] -SFR relation (Figure 2.7; top right panel). It also holds for the resolved measurements, which follow a similar trend of increasing [C II] luminosity with increasing SFR. These subregions are concentrated at a particular [C II] - SFR range, indicating a homogeneous, non-complex structure. This result for the single system is consistent with the previous finding from Smit et al. (2018).

The bottom right panel of Fig. 2.7 demonstrates how the spatial distribution is correlated with the [C II] luminosity and SFR. The positive correlation of galaxies at $z = 5-6$ is displaced from the local relation, such that galaxies and their substructures have a lower [C II] luminosity than previously expected (dashed black line; Carniani et al., 2018a). The [C II] and SFR surface densities of the integrated and resolved measurements of COS2987 are defined at the effective radius of the [C II] and UV emission, respectively. In this case, both the global system and subregions are located slightly below (within 3σ of) the local $\Sigma_{\mathrm{[CII]}} - \Sigma_{\mathrm{UV}}$ relation (black solid line and gray area; Herrera-Camus et al., 2015a). These results for both relations support the scenario shown by previous studies, where a [C II] deficiency may be in place in high redshift galaxies, even for galaxies that tightly follow the local $L_{[CII]}$-SFR relation. In any case, COS2987 and its subregions are closer to the local relation than we would expect from the high-z relation from C18, hinting that the physical conditions are closer to local galaxies than in previous detections.

The high line-to-continuum ratio $[\mathrm{C\,II}]/L_{\mathrm{IR}} \geq 1.5\%$ and the fact that COS2987 lies within the local $L_{[CII]}$-SFR relation evidence different physical mechanisms causing the [C II] deficit than those taking place in high-infrared-luminosity starbursts ($[\mathrm{CII}]/\mathrm{FIR} \sim 0.1\% - 0.01\%$ Herrera-Camus et al., 2018b). The [C II] deficiency could be a consequence of an underestimation of the $L_{[CII]}$, as (Carniani et al., 2020) reported fluxes losses of 20-40% when the angular resolution is comparable to the size of the emitting region. Our high-resolution observations were combined to the shorter baselines of the previous low-resolution data set, and the latter has a $0.8''$ resolution sufficiently greater than the typical [C II] emission size of COS2987 ($\sim 0.5''$ obtained by a Gaussian fit in the moment-0 map). Therefore, we conclude that this observational feature does not influence the [C II] deficiency in COS2987.

Recent PDR models and simulations attribute the existence of [C II] under-luminous normal galaxies as a consequence of multiple conditions in the ISM such as a positive deviation from the Kennicutt-Schimidt relation (due to a starburst phase), low metallicity, and low gas density (Ferrara et al., 2019). Unless $Z < 0.1\ Z_{\odot}$, the metallicity and low gas density just play a subdominant role in the [C II] deficiency (Vallini et al., 2015; Lagache et al., 2018; Pallottini et al., 2019; Lupi & Bovino, 2020). Any combination of these effects could be at play in COS2987, although such a low metallicity ($Z < 0.1\ Z_{\odot}$) would move COS2987 below the local $L_{[CII]}$-SFR relation.

In any case, the [C II] emission cannot fully characterize the ionization state of COS2987 and thus disentangle the degenerate contribution of these parameters. Therefore, other far-infrared (FIR) lines, such as $[\mathrm{OIII}]_{88\mu m}$ and [C III] , are necessary to entirely resolve this tension (Vallini et al., 2020; Carniani et al., 2020; Vallini et al., 2021).

2.4.3 DYNAMICAL STATE AND EVOLUTION OF σ

ALTERNATIVE SCENARIOS

In Section 2.3, we characterized the velocity map of COS2987 with a velocity gradient (Figure 3.4) and a homogeneous velocity dispersion map typical of rotating-disk galaxies, as previously pointed out by Smit et al. (2018). Nevertheless, this might not exclusively be produced by a rotating pattern, especially when it is associated with limited-resolution data. We thus consider two other possible origins to describe the observed velocity gradient in the galaxy: (i) flux of gas towards the circumgalactic medium caused by stellar and AGN feedback and (ii) major mergers. If it is not satisfactorily spatially resolved, both cases can reproduce in the velocity map blueshifted and redshifted lobes smoothed by the beam size. We discuss the reality of these scenarios as follows:

First, outflows can increase the dispersion of the system and add a broad component to the spectrum. Resolved observations and stacking spectrum of normal star-forming galaxies at z > 5 show an extra component with a typical FWHM of a few hundred of km s^{-1} (Ginolfi et al., 2020b; Herrera-Camus et al., 2021). To test this, we fit a two-component Gaussian profile (broad and narrow component) to the spectrum of the main source C (top panel, Figure 2.2), but the resulting chi-square is indistinguishable from the fitting of a single Gaussian profile fit. Given the overall narrow line width of the [CII] line and the lack of evidence for a two-component line profile, we consider this possibility unlikely.

Second, the large gas motions resulting from galaxy mergers can imprint multiple components on the moment-0 map and the spectrum and disturb considerably the velocity dispersion map (Romano et al., 2021). In the case of COS2987, we do not see any obvious secondary source component distribution in the [C II] moment-0 map or the spectrum and individual channel maps. Similarly, there is no evidence for merger activity in the central region of this source (C) in any of the available HST images. The latter is clearly described by a single Sersic profile (Fig. 2.3). Given the lack of dust detection at this position, it is unlikely that the rest-UV distribution seen in the HST images is affected by differential dust obscuration. The dispersion map shows a mainly homogenous low average dispersion ~ 29 km s^{-1}, compared to merging systems at z > 5 in the ALPINE survey (Romano et al., 2021). Moreover, COS2987 has a lower mass of 1.7×10^9 $M_\odot$, as compared to the mass of $\sim 10^{10}$ $M_\odot$ of these merging systems. With the current ALMA [CII] and HST rest-UV data, we can discard a compact merger with separations larger than 2-3 kpc.

As suggested by Rizzo et al. (2022), after several tests with disks and mergers simulations, an accurate differentiation of disks and mergers galaxies requires observations to cover three beams over the major axis of the galaxy and S/N $>$ 10, conditions that are not achieved by our data. With this caveat in mind, in the next two subsections, we examine the implications of an evolution of disk galaxies assuming that the velocity gradient in the velocity map and p-v diagram arrives from a rotating gaseous disk.

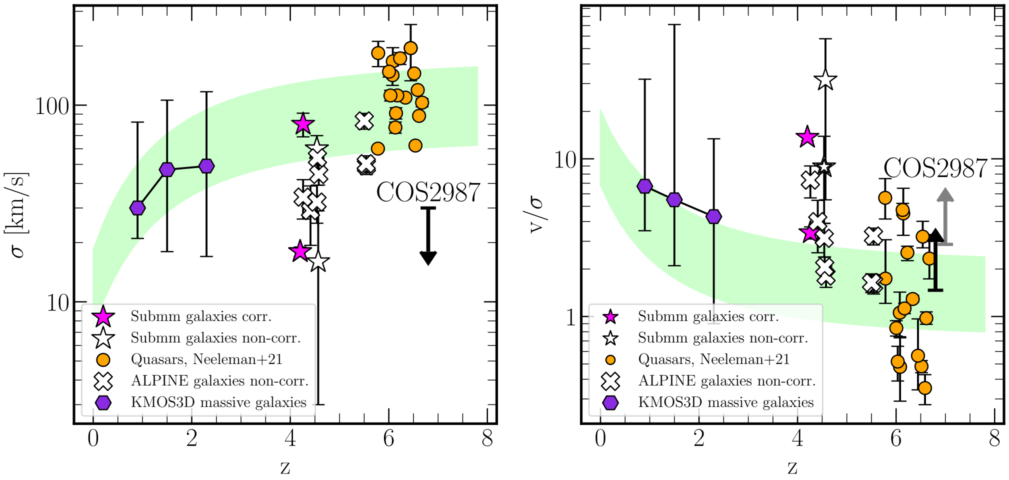

Figure 2.8: Dynamical state of COS2987 in the context of the cosmic evolution of the expected dispersion velocity (left panel) and rotation-to-dispersion ratio (right panel). As a reference, other intermediate- and high-redshift sources are displayed in both panels: KMOS3D massive galaxies at z = 1-2 (purple hexagons; Übler et al., 2017), normal star-forming galaxies of ALPINE survey at z = 5-6 (white crosses; Jones et al., 2021), massive starbursts at z $\sim$ 4.5 (pink and white stars; Neeleman et al., 2020; Fraternali et al., 2021; Rizzo et al., 2020), and quasars at z $>$ 6 (orange circles; Neeleman et al., 2021). The green filled area represents the expected values for the dispersion and rotation-to-velocity from a semi-analytical model based on the Toomre parameter (Wisnioski et al., 2015). COS2987 is represented by upper limits due to resolution limitations (see text). In the right panel, the black upper limit represents the rotation-to-dispersion ratio for the outer regions of the galaxy. The gray upper limit corresponds to the ratio for the average rotational and dispersion velocity. It is slightly offset from the black upper limit for better viewing.

STABILITY AND EVOLUTION

The evolution of the intrinsic velocity dispersion and the rotation-to-dispersion ratio with redshift elucidate which physical mechanisms can play a role during galaxy evolution (Girard et al., 2018; Übler et al., 2019, and references therein). Both simulations and observations point to an increase of the velocity dispersion with redshift indicating that high-redshift disk galaxies are "hotter" dynamically (**?**). Galaxies may have experienced constant turbulence caused by several physical mechanisms, such as energy transfer by winds due to supernova episodes that can generate gas outflows to the outer regions (Mac Low & Klessen, 2004), instability due to the accretion process of cold gas from cosmic filaments (Dekel et al., 2009), and instabilities generated by major and minor mergers (Bournaud et al., 2010; **?**). Furthermore, recent simulations indicate that rotation-supported systems should be expected in the first billion years after the Big Bang(Kereš et al., 2005b; Dekel et al., 2009).

Sensitive CO and Hα imaging surveys of main-sequence galaxies at $z \sim 1-2$ have shown that this population is dominated by rotation-supported systems (Tacconi et al., 2010; Übler et al., 2019; Genzel et al., 2020; Sharma et al., 2021). Recent studies, mainly based on [C II] analysis, point to the presence of fast cold rotators among massive galaxies with intense star formation already at z $\sim$ 4.5 (Neeleman et al., 2020; Rizzo et al., 2020; Fraternali et al., 2021; Lelli et al., 2021). Furthermore, analyses of ALPINE [C II] data cubes indicate that an important fraction ($\sim 40\%$) of the massive main sequence galaxies at $z = 4-6$ can also be associated to rotating disks (Jones et al., 2021) (z = 4 - 6). Smit et al. (2018) showed that rotating disks are already in place at $z \sim 7$. One of the big challenges in this regard is related to the limited resolution and depth of these studies aiming to confirm whether these systems are, in fact, rotating disks.

If we consider the velocity gradient of COS2987 comes from a rotating disk, we can check the stability state of the system and put it into the context of the dynamical evolution of disks. In Fig. 2.8, we show the intrinsic velocity dispersion and rotation-to-dispersion ratio as a function of redshift for COS2987 and recent observations. We compared them with the expected average dynamical parameters for galaxies from the semi-analytical model of Wisnioski et al. (2015, 2019) (green area). We included a sample of main-sequence star-forming galaxies from the

ALPINE survey (white crosses, Jones et al., 2021) at $z > 4$ and the following massive starburst galaxies: DLA0817g (z = 4.26, Neeleman et al., 2020), SPT–S J041839–4751.9 (z = 4.2, Rizzo et al., 2020), and finally AzTEC/C159 (z = 4.57) and J1000+0234 (z = 4.54, Fraternali et al., 2021). They are all signed as stars in Figure 2.8. We also included available dynamical data from quasar host galaxies at $z > 6$ (orange circles; Neeleman et al., 2021).

We noted that there are differences in the definitions of the rotational and dispersion velocity in the literature. We homogenized them as specified by Wisnioski et al. (2015), in which the velocity dispersion is defined at the outer regions of the galaxy to avoid beam-smearing effects. The quasars (Neeleman et al., 2021) and the massive galaxy DLA0817g (Neeleman et al., 2020) were derived by assuming a constant dispersion and rotational velocity profile, therefore no change is needed. For the starburst massive galaxy SPT0418-47, Rizzo et al. (2020) assumed an exponential model for the dispersion velocity profile. We thus used the measurements for R $>$ 1 kpc, where the rotational velocity and dispersion flatten. These two massive galaxies are represented as pink colors in Figure 2.8. For the massive galaxies AzTEC/C159 and J1000+0234 (Fraternali et al., 2021) and the normal star-forming ALPINE galaxies (Jones et al., 2021), the rotational and dispersion velocities were obtained using $^{\rm 3D}$BAROLO and no fixed radial profile shape for the velocity dispersion was used. Due to the beam size, the points for the rotational and dispersion velocities profiles are not independent. For each galaxy, we thus simply took the average value in all rings and caution of possible conclusions for these systems. Therefore, all cases that could not be corrected are marked in white. Finally, for the galaxy COS2987, we computed values for three rings with a width of $0.18''$, and we took the value for the third ring, located at $0.45''$(black upper limit in both panels of Fig. 2.8). However, since it is close to the [C II] effective radius ($0.38''$) and the points are not completely independent, we also display in the left panel the average rotational-to-dispersion ratio (gray upper limit slightly offset from the black one for better visualization).

From this comparison, we note that the model agrees with the average dynamical state of massive disks at $z \sim 1-2$ (KMOS3D survey; Übler et al., 2017) and quasar host galaxies at z $\sim$ 6. However, it struggles to reproduce the velocity dispersion and rotation-to-dispersion ratios of most massive and star-forming galaxies at $z \sim 4-6$. The typical star-forming galaxies and some of the massive galaxies may be affected by beam smearing, which can overestimate the values of the rotation-to-dispersion ratio. But the massive starburst galaxies, especially SPT0418-47 ($\sigma = 18 \pm 1$ km s^{-1} and $v/\sigma = 13.7 \pm 0.7$), also diverge from what is expected by the models and simulations.

We found a value of $v_{rot}/\sigma \geq 1.4$ for COS2987, which agrees with the semi-analytical models, but we noted a low-velocity dispersion (upper limit, Fig 2.8, right panel), where the expectation is to have highly turbulent systems. This implies that the disk, if in place, is likely in a stable dynamical state. This is mildly at odds with our finding of a northern arm, which could represent an ongoing minor merger (or gas inflow) and would thus imply a highly active stage of assembly. Such an event (and possibly subsequent ones) would result in a significant perturbation of the galaxy disk. As pointed out by Katz et al. (2019), observing stable disks at these epochs might represent a short-lived phase, likely coincidental with a particular line-of-sight and geometry, before the galaxy experiences further perturbations. In the case of quasars, such objects are likely in a highly turbulent phase, due to the presence of a dominant AGN.

We noted that the choice of source inclinations for COS2987 would increase the resulting velocity dispersion, thus providing a better agreement with the expected dispersion velocity at $z \sim 7$. To test this assumption, we ran ^{3D}BAROLO with a fixed dispersion velocity of 65 km s^{-1}, which matches the expected velocity dispersion at this redshift. Higher inclinations yield poorer fits to the velocity dispersion maps, making such a conclusion unlikely. These results rule out the possibility that our galaxy would represent a highly unstable system.

We diagnosed the prospect of the candidate gaseous disk developing local instabilities by the Toomre Q-parameter (Toomre, 1964). It is defined by $Q = \kappa\sigma/(\pi G \Sigma_{gas})$, where σ is the dispersion velocity; G is the gravitational constant; Σ_{gas}[2] is the gas surface density, and $\kappa = (2\Omega/r)d(r^2\Omega)/dr = av_c/r$ is the epicyclic frequency, where v_c is the circular velocity and $a = \sqrt{2}$ for a flat rotational curve. For the gas surface brightness, we adopted the total gas mass at the effective radius of $M_{gas} = (5 \pm 3) \times 10^9$ $M_\odot$ ($M_{gas} \sim M_{dyn} - M_*/2$, M_*; see Subsection 2.4.3). If $Q < 1$, the gaseous disk is susceptible to local gravitational collapse. Otherwise ($Q \geq 1$), the system would not be inclined to develop clumpiness. For the effective radius and maximum rotational velocity, we found a mean $Q = 0.44$, indicating that even though COS2987

---

[2] $\Sigma_{gas} = \frac{M_{gas}}{\pi (r^{eff}_{[CII]})^2}$

is a possible rotationally supported system, it is prone to face gravitational instabilities in its internal structure.

CONVERSION FACTOR

We dynamically characterized the galaxy for a rotating-disk scenario, therefore, it is possible to measure the dynamical mass of the system within its effective radius. Rest-frame observations in the near-infrared (NIR) provide the measurement of the extension of the stellar population of the galaxy. Since the rest-frame optical data from Spitzer imaging does not resolve the galaxy sufficiently, we chose the [C II] effective radius as a proxy of the stellar extension, supported by the agreement of the [C II] and UV effective radii. From the maximum rotation velocity of the system, we obtained a dynamical mass of M_{dyn} =(6 ± 3) x 10^9 $M_\odot$. We estimated the total mass of gas at the effective radius, given that the inner region of the galaxy is baryonic dominated ($M_{gas} \sim M_{dyn}$ - $M_*/2$, M_* = 1.7 x 10^9 $M_\odot$; Smit et al., 2018), leading to the value of M_{gas} = (5 ± 3) x 10^9 $M_\odot$.

Considering the [C II] luminosity within the [C II] effective radius of the galaxy ($0.38'' \sim 2$ kpc), we can get the [C II] -to-gas conversion factor. We estimated a conversion factor for the total galaxy gas mass as $\alpha^{total}_{[CII]} = 62 \pm 7$ $M_\odot/L_\odot$ which is a considerably larger value than the median (7^{+4}_{-1} $M_\odot/L_\odot$) for starburst galaxies supported by rotation at z = 4.5 (Rizzo et al., 2021).

Finding the conversion factor for molecular gas is a harder task, since there is no direct measurement of the molecular gas mass at this redshift. If we assume that 70% of the [C II] emission is due to PDR regions (Stacey et al., 1991, 2010), we find an upper limit of $\alpha^{mol}_{[CII]} \leq 90$ $M_\odot/L_\odot$[3], a higher value than the one achieved by Zanella et al. (2018) (mean value of $\alpha^{mol}_{[CII]} = 31$ $M_\odot/L_\odot$).

2.5 CONCLUSIONS

In this paper, we analyze the morphology and kinematics state of the normal star-forming galaxy COS2987, at z ∼ 7. Previous studies found a low dust content and tentative evidence for a velocity gradient, suggesting possible disk rotation (but indistinguishable from a merger

---

[3] Derived from $\alpha^{mol}_{[CII]} = \frac{M_{gas}}{(70\% \times L_{[CII]}/2)}$.

scenario). The new higher-resolution [C II] observations obtained with ALMA in Band 6 can resolve 2 kpc-scale structures, allowing us to perform a detailed study of the cold ionized gas conditions, distribution, and kinematics. We compared the spatial distribution of the stellar and [C II] line emission components to search for hints of extended [C II] emission. We also performed a dynamical fitting using ^{3D}BAROLO to study the possibility of rotation in the galaxy and put it in context with the cosmic evolution of disk galaxies. Finally, the high resolution allowed us to look individually at the components of the galaxy and study the scattering of the L_{CII}-SFR relation and offset in the Σ_{SFR} vs Σ_{CII} relation.

We summarized our findings below:

- **No extended emission/[C II] halo:** COS2987 presents a good match between the cold ionized gas ([C II]) and UV continuum distribution. The [C II] and UV spatial extensions agree within the uncertainties and the radial profile of the emissions is similar in shape and size, even though we could see a [C II] emitter satellite in the north-east portion of the galaxy. Therefore, we did not detect any signs of a [C II] halo, indicating that such structures are not ubiquitous at these redshifts.

- **Complex environment:** The galaxy presents an extended arm-shaped structure, which can be associated with a satellite being accreted. Additional possible evidence for [C II] structures and clumps are found in its neighborhood, within a 10-kpc region. Deeper observations are needed to confirm these structures.

- **A disk candidate in the early Universe**: The rotation-to-dispersion ratio agrees with the models, but a low velocity dispersion reveals that COS2987 is going through a non-turbulent phase. If the scenario of having a complex environment composed of other satellites is correct, the stability of the candidate disk can be a short event, with the disk being affected in posterior times. The suggested rotating disk nature hints that these structures appear as early as the first billion years of the universe. But the low fraction of rotation-ordered normal star-forming galaxies (40%; Jones et al., 2021) at $z > 4$ indicate that this is a subdominant dynamic state in this cosmic epoch. Deeper and higher resolution observations are mandatory to rule out the scenario in which COS2987 is a compact merger.

- **[C II] deficiency:** COS2987 and its substructures lie along the tight correlation $L_{[CII]}$ and SFR of nearby normal star-forming galaxies, but they fall below the local relation of Σ_{SFR} vs Σ_{CII}. This suggests that the [C II] emission may be affected by a strong radiation field caused by a starburst phase, low metallicity, or low gas density. Complementary FIR lines are needed to fully understand the ionization structure of COS2987.

Our findings support the necessity of kpc-scale resolved observations to unveil the nature and properties of the ISM in galaxies early in the Universe. Forthcoming similar observations in larger samples (e.g., REBELS and CRISTAL ALMA large programs) will provide insights into the ubiquity of disks at early cosmic times. Future observations with JWST will also help us to constrain the high-ionization optical lines, which are critical tracers of warm, moderate-density gas environments.

CHAPTER 3

[CII] EXTENDED EMISSION IN AN INTERACTING SYSTEM AT Z $\sim$ 5.5

The content of this chapter will be submitted to the journal Astronomy & Astrophysics (A&A)

3.1 INTRODUCTION

Galaxy growth is dictated by an interplay of several physical processes that transform the galactic internal properties across cosmic time (Somerville & Davé, 2015; Tumlinson et al., 2017). The current galaxy evolution paradigm supports that gas accretion from the intergalactic medium and intense merger activity provide pristine gas to fuel star formation in a galaxy, while AGN and stellar feedback can add the input energy to deplete and expel the internal gas outwards the interstellar medium (ISM), eventually halting star-forming activity (Barnes & Hernquist, 1991; Sanders & Mirabel, 1996; Lambas, D. G. et al., 2012; Sánchez Almeida et al., 2014; Hayward & Hopkins, 2016; Harrison, 2017). We are in the first steps of detecting and characterizing the origin and composition of such gas transport at high redshift, which will enable us to understand the full baryonic cycle at the early stages of galaxy formation. Since these intricate physical mechanisms shape the spatial distribution of the baryonic matter, the morphology becomes the primary indicator of the evolutionary history of these systems. For example, when dynamical events and internal processes (such as mergers and outflows) occur, galaxies get disrupted and distorted (Nelson et al., 2019). Furthermore, the diversity of shapes of low-redshift galaxies correlates with several physical properties, such as the stellar mass, star formation histories, and environment (Baldry et al., 2004; De Lucia et al., 2006; Poggianti et al., 2010; Tojeiro et al., 2013). For instance, elliptical and lenticular galaxies reside preferentially in regions of very high local density, populating especially the cores of clusters and groups, while spiral galaxies inhabit field regions (Dressler, 1980; Postman et al., 2005). However, high-redshift galaxies, because of their distance, are fainter, have a smaller angular size, and suffer from cosmological dimming which makes detecting subtle features challenging, and thus the physical mechanisms that had shaped them.

Most studies of the spatial distribution of high-redshift galaxies rely on rest-UV imaging from the Hubble Space Telescope (HST), as it was the only instrument that provides sufficiently high spatial resolution and depth to reveal the inner structures of small galaxies at these wavelengths. Such observations reveal that galaxies at $z > 4$ are clumpy and irregular, indicating high merger activity in the first billion years of the universe (Elmegreen & Elmegreen, 2005; Conselice & Arnold, 2009; Duncan et al., 2019; Shibuya et al., 2022). However, the HST imaging can not provide a full answer because the UV emission is strongly affected by dust obscuration and recent rest-frame optical JWST imaging has been revealing that many of these clumps are just the compact star-forming regions of disk galaxies, which surprisingly became a common population ($\sim 50\%$) at z = 3-6 (Ferreira et al., 2022; Guo et al., 2023).

Nevertheless, a complete picture of the evolutionary path of galaxies inevitably requires information on the cold gas supply to form stars. Fortunately, the emergence of the Atacama Large Millimeter/submillimeter Array (ALMA) in the last decade was the pivotal point to a new era in assessing such gas at high-redshift in sub-arcsec scales. The cornerstone of these groundbreaking studies has been the [C II] line emission, arising from the fine-structure transition $^2P_{3/2} \rightarrow {}^2P_{1/2}$ of the singly ionized carbon atom (hereafter just [C II] , centered at 158 μm). This is one of the strongest far-infrared (FIR) lines, reaching up to 1% of the total bolometric luminosity (Díaz-Santos et al., 2013; Cormier et al., 2015; Herrera-Camus et al., 2018a; Schaerer et al., 2020). Due to its low ionization potential of 11.2 eV, it is a dominant gas coolant of the neutral ISM coming from photo-dissociation regions (PDR), cold molecular, ionized, and atomic phases. (Wolfire et al., 2003; Vallini et al., 2015; Clark et al., 2019).

A remarkable outcome of recent studies on the spatial distribution of the gas- and star-forming components of galaxies at $z = 4 - 6$ is the existence of extended [C II] line emission reaching out to $\sim$10 kpc radially, or about 5× beyond the extent of the star-forming areas as traced by rest-UV and dust continuum (Fujimoto et al., 2019). These so-called "[C II] halos" have been primarily identified by measuring radial profiles of visibility-based stacking of [C II] emission of 18 normal star-forming galaxies at $z > 4$ by Fujimoto et al. (2019), selected as single systems with no obvious AGN signature. Several studies found similar [C II] structures in individual star-forming galaxies at $z > 4$ (Fujimoto et al., 2020; Herrera-Camus et al., 2021; Akins et al., 2022; Lambert et al., 2023) and massive quasar host galaxies at $z > 6$ (Maiolino et al., 2012; Cicone et al., 2015; Meyer et al., 2022). [C II] halos appear to be ubiquitous in the most massive galaxies yet less relevant in lower mass systems ($M_* < 1\text{x}10^{10}\,M_\odot$) (Fujimoto et al., 2020; Posses et al., 2023; Pizzati et al., 2023).

The presence of emitting carbon-rich gas beyond galactic sizes raises the question of how carbon produced by stellar nucleosynthesis in the central regions of these galaxies was transported to larger distances whilst remaining in a singly ionized state. Mock observations of state-of-the-art cosmological simulations fail to reproduce the [C II] surface brightness distribution of observed galaxies (Fujimoto et al., 2019; Pizzati, Ferrara, Pallottini, Sommovigo, Kohandel & Carniani, 201; Arata et al., 2020). Several plausible physical mechanisms for the origin of these 'halos' have been proposed in the literature (Fujimoto et al., 2019) including the presence of unresolved satellite galaxies around the central source, extended photodissociation or [C II] regions, cold streams, and outflows. Among all scenarios, several studies detected broad components in the [C II] spectrum of stacked and individual galaxies, suggesting that the [C II] halos are the result of past/ongoing episodes of high-speed streams of outflowing gas driven by powerful stellar feedback (Gallerani et al., 2018; Ginolfi et al., 2020a; Herrera-Camus et al., 2021). This is supported by recent semi-analytical models of cold-mode phase outflows ($T \approx 10^{2-4}$ K), which can reproduce [C II] surface brightness profiles (Pizzati et al., 2020, 2023).

However, an additional scenario was proposed by Ginolfi et al. (2020c), which identified a luminous envelope of [C II] emission surrounding a dense merging system at redshift z $\sim$ 4.5. This phenomenon leads to gas stripping, where the gas is removed from the ISM and enriches the circumgalactic medium (CGM) with chemically enhanced material. Similarly, Lambert et al. (2023) reported a [C ii] fuzzy, extended emission in a typical galaxy at redshift z = 5.25, showing indications of a late-stage merger rather than outflow signatures. Most studies rely on observations with a resolution of $\sim$0.8$''$ which can resolve the current halos physical scales in less than two resolution units. The understanding of the dynamic state of these systems that can support or rule out the last scenario is also impacted since a good resolution is needed to reveal the nature of single/multiple sources (Rizzo et al., 2022).

In this context, the ALMA large program CRISTAL ([C ii] resolved ISM in Star-forming galaxies with ALMA) survey comes to light providing the critical conditions to solve these open questions. CRISTAL aims to dissect the [C ii] and dust continuum in 25 mass-selected star-forming galaxies with available ALMA lower-resolution observations and UV continuum detections. The observations improve the sensitivity and spatial resolution allowing them to resolve in 1-2 kpc scales, which is crucial to confirm the detection and identify the physical mechanisms powering the [CII] emission at such distances. This paper, as part of the following series of CRISTAL results, reports our analysis of the compelling case of the main-sequence star-forming galaxy HZ3, identified in the survey as CRISTAL-05 , at z = 5.54 (Capak et al., 2015). This was one of the galaxies reported by (Fujimoto et al., 2020) which host a [C ii] halo, but yet with a still uncertain detailed description of the spatial and dynamical internal structure. Here, we take advantage of the deepest ALMA integration in the CRISTAL sample, owing to previous deep pilot observations, to study the nature of the system and the origin of the puzzling [C ii] halo. Throughout the article, we follow Lambert et al. (2023) point that this is an unusual use of the term halo, since the well-establish halo component (dark matter haloes, stellar haloes, and galactic haloes) refers to a spheroidal shape, that we can not conclude with the resolution in hands. Therefore, we prefer to call it a [C ii] extended emission.

Firstly, we describe in Section 2 the general properties of the galaxy, as well as the ALMA observations and ancillary data. In Section 3, we detail the main results. We characterize the morphology of the [C ii] emission and compare it to the rest-frame UV and dust continuum. We also quantify the multiwavelength extensions. The gas motions are then determined by the moment-1, moment-2, and position-velocity diagram. After that, we dissect the substructure of the system in different components with a clump-finding algorithm. We finally perform a kinematical disk modeling in one of the components of CRISTAL-05 . Section 4 presents a discussion of the results of the previous section. Lastly, in section 5 we summarize the work and main conclusions. We assume a standard ΛCDM cosmology with: $\Omega_{\Lambda} = 0.7$, $\Omega_{M} = 0.3$ and $H_0 = 70\,\mathrm{km\,s^{-1}\,Mpc^{-1}}$, which leads to a physical conversion factor of 5.961 kpc/″.

3.2 OBSERVATIONS AND DATA REDUCTION

A brief description of the target selection and all datasets analyzed in this work is presented below.

3.2.1 TARGET: CRISTAL-05

CRISTAL-05 (also known as HZ3 and COSMOS2015 683613, Capak et al., 2015; Laigle et al., 2016) was first selected as a Lyman break galaxy in the Cosmic Evolution Survey (COSMOS, Laigle et al., 2016), and it was spectroscopically confirmed to be a high-redshift galaxy by UV absorption lines (Ilbert et al., 2013). Posterior ALMA follow-up revealed bright [C II] emission confirming a $z_{[CII]} = 5.546 \pm 0.004$ (Capak et al., 2015), and a non-detection of dust continuum emission, indicating that the galaxy has a low dust content (Capak et al., 2015; Barisic et al., 2017; Faisst et al., 2017).

CRISTAL-05 lies in the expected main sequence of star-forming galaxies at $z \sim 5.5$ ($L_{UV} \sim L^*$), and thus was observed as part of the ALMA Large Program to Investigate C+ at Early Times (ALPINE, Le Fèvre et al., 2020; Béthermin et al., 2020; Faisst et al., 2020) survey, where it was firstly classified as an extended dispersion-dominated system, based on a morpho-kinematic analysis (Le Fèvre et al., 2020). A more detailed analysis updated it to an uncertain classification as it revealed a southern blue, compact source, although the reality of such a source was not well established (Jones et al., 2021). Carniani et al. (2018b) and Fujimoto et al. (2020) found that the [C II] effective radius exceeds the rest-frame UV effective radius by a factor 2, and although it deviates positively from the local $L_{[CII]}$-SFR relation, it presents a [C II] deficiency in the $\Sigma_{[CII]}$ - Σ_{SFR} parameter space. Finally, Fujimoto et al. (2020) found that the [C II] emission extends up to 10 kpc in contrast with the rest-UV and dust emission, being identified as one of the individual detections of [C II] haloes.

In summary, the galaxy is a not-dusty, typical star-forming galaxy in the first billion years

Product	robust	rms μJy beam^{-1}	Beam
Continuum	1	8.8	$0.33'' \times 0.27''$
Cube 10 $\mathrm{km\,s^{-1}}$	1	150	$0.36'' \times 0.29''$
Cube 20 $\mathrm{km\,s^{-1}}$	1	123	$0.31'' \times 0.26''$
[C II] map	0.5	45	$0.21'' \times 0.18''$
[C II] map	1	42	$0.33 \times 0.27''$

Table 3.1: Properties of the main ALMA products.

of the universe with a complex morpho-kinematical structure. These features make CRISTAL-05 an ideal target to study the mechanisms of transportation and emission of the [C II] line in far distances of the central source. The full description of the sample selection, science goals, and data products of the CRISTAL survey are described in Herrera-Camus in prep.

3.2.2 ALMA OBSERVATIONS

We combined different Band 7 ALMA observations of CRISTAL-05 : ALPINE survey in configuration C43-2 (PI: Olivier Le Fèvre, ID: 2017.1.00428.L), CRISTAL pilot program in configuration C43-5 (PI: Manuel Aravena, ID: 2018.1.01359.S) and CRISTAL observations in the configurations C43-2 and C43-5 (PI: Rodrigo Herrera-Camus, ID:2021.1.00280.L). All observations aimed at detecting the [C II] emission line ($\nu_{\rm obs} = 290.6$ GHz) and FIR dust continuum and the four spectral windows fall within closely matching frequency ranges. The different programs use slightly different spectral setups and spectral resolution and the frequency range for the [C II] emission line is well covered. In all cases, four spectral windows were used with an individual usable bandwidth of 1875 MHz.

DATA REDUCTION AND JVM CORRECTION

We downloaded and processed the datasets from the different programs using the corresponding pipeline versions. No extra manual flagging was needed beyond what was already identified by the observatory and automatically flagged by the pipeline. We combined the calibrated datasets into a single measurement set (ms) used to create the images and data cubes. We identified the emission lines and continuum emission in the initial multi-frequency synthesis (mfs) images and data cubes of all the available SPWs to then create the line-free continuum images and subtract the continuum emission using UVCONTSUB with FITORDER = 0.

We created the final product using TCLEAN and the auto-multithresh algorithm. This mode automatically masks regions based on the signal-to-noise of the emission in the image. The way such regions are created depends on the following parameters, SIDELOBETHRESHOLD = 2, NOISETHRESHOLD = 4.5, LOWNOISETHRESHOLD = 2 and MINBEAMFRAC = 0.0. This value choice is intended to match similar results created by eye when using manual cleaning. In all the cases, the cleaning was down to 1σ by selecting NSIGMA=1 where σ is estimated automatically by TCLEAN using robust statistics ($\sigma = 1.4826 \times \mathrm{MAD}$, with MAD being the median absolute deviation). We mainly worked on the products created using a Briggs weighting scheme with ROBUST = 2, but some auxiliary inspections were carried out on the products with and ROBUST = 0.5 (Section 3.3.2).

The primary motivation for cleaning down to such a low threshold of NSIGMA=1 was to try to minimize the "JvM effect" (Jorsater & van Moorsel, 1995; Czekala et al., 2021). Combining multiple array configurations of an interferometer can produce a non-ideal baseline distribution and a synthesized beam that will depart from an ideal Gaussian beam. In these cases, the TCLEAN algorithm can produce final images that mix dirty and clean beam units and incorrect recovered fluxes. To correct for the JvM effect, we applied in all the products the correction suggested by Czekala et al. (2021) that compares the volumes of the clean and dirty beams to determine an ε correction parameter to apply to the residuals. In the case of the data cubes, the correction was estimated at the channel closer to the peak of the [C II] line and applied to all channels. A more detailed description of the data reduction and JvM correction is covered in Gonzalez-Lopez in prep. We summarize the noise level and the synthesized beam sizes of the products used along the following sections in Table 3.1.

3.2.3 HST OBSERVATIONS

We use the available *Hubble Space Telescope/Wide Field Camera 3 near-infrared* (NIR) imaging of CRISTAL-05 as part of the Cosmic Assembly Near-IR Deep Extragalactic Legacy Survey (CANDELS, PI: Sandra Faber, ID: 12440). Observations were performed in 2015 in 1 orbit per filter for the F105W (1.05 μm), F125W (1.25 μm), F140W (1.4 μm), and F160w (1.54 μm) filters. For a galaxy at $z \sim 5.5$, these filters correspond to adding information on the rest-frame near-UV emission at 1605 Å, 1911 Å, 2400 Åand 2450 Å. Raw images were re-calibrated using the latest versions of the pipeline and the astrometry was corrected using GAIA stars. All images have a PSF of FWHM = $0.2''$ and pixel scale of $0.06''$ pixel^{-1}. The unobscured star formation rate $\mathrm{SFR_{UV}}$ is derived by conversion of the luminosity measured in the HST/F105W filter, using the calibration provided by Kennicutt & Evans (2012) and a Kroupa IMF (Kroupa & Weidner, 2003).

3.2.4 JWST OBSERVATIONS

James Webb Space Telescope (JWST) observed CRISTAL-05 as part of the PRIMER program (GO 1837, Dunlop et al., 2021) using the Mid-Infrared Instrument (MIRI) camera. The filter used was F770W and was observed for 29.6 minutes. The data were calibrated using the latest version of the pipeline and astrometrically corrected using both GAIA stars and the sources detected by HST in the same field.

3.3 ANALYSIS AND RESULTS

3.3.1 [C II] LINE AND DUST EMISSION

We measured the spatially integrated [C II] line profile using a $1.5''$-aperture centered at the emission centroid. [C II] is detected and best fit by a single-gaussian distribution with FWHM = 236 ± 18 km s^{-1} and line flux of 1.00 ± 0.07 Jy km s^{-1}, corresponding to a signal-to-noise (S/N = 14). This is consistent with the total flux measured by the ALPINE survey (Le Fèvre et al., 2020), and about 45% higher than the total flux of observations of (Capak et al., 2015).

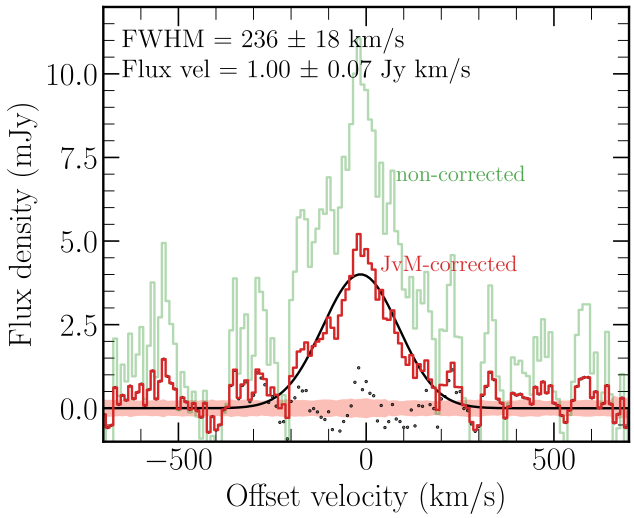

Figure 3.1: [C II] spectrum of CRISTAL-05 , which is extracted within a circular aperture of diameter of 1.5″ , and centered in the [C II] observed frequency $\nu_{\rm obs}$ = 292.48 GHz. We display the continuum-subtracted spectrum from the non-JvM corrected and JvM corrected data cubes (green and red lines, respectively). The black solid line corresponds to the 1-d Gaussian fitting, and the residuals are plotted as black dots.

Table 3.2: Observational and physical properties of CRISTAL-05

Property	Value
Center	(+10:00:29.86,+02:13:02.19)
$z_{\rm [CII]}{}^{a}$	5.5416 ± 0.0002
$\rm SFR_{UV}$ ($\rm M_\odot\ yr^{-1}$)	22 ± 1
$\rm SFR_{IR}{}^{b}$ ($\rm M_\odot\ yr^{-1}$)	1.38 ± 0.09
Stellar mass^{b} (10^{10} $\rm M_\odot$)	1.4 ± 0.6
S/N ([C II])	13
[C II] line flux (Jy km $\rm s^{-1}$)	1.00 ± 0.07
$\rm FWHM_{[CII]}$ (km $\rm s^{-1}$)	236 ± 18
$S_{158\mu m}{}^{a}$ (mJy)	0.118 ± 0.021
$\rm L_{[CII]}$ (10^{8} $\rm L_\odot$)	9.3 ± 0.7
$\rm L_{IR}$ (10^{11} $\rm L_\odot$)	1.60 ± 0.08

Notes: Values derived in this work were obtained in a 1.5″ -aperture; see Section 3.3.1.
[a]Capak et al. (2015), [b]Measured by Mitsuhashi in prep., [c]Integrated S/N.

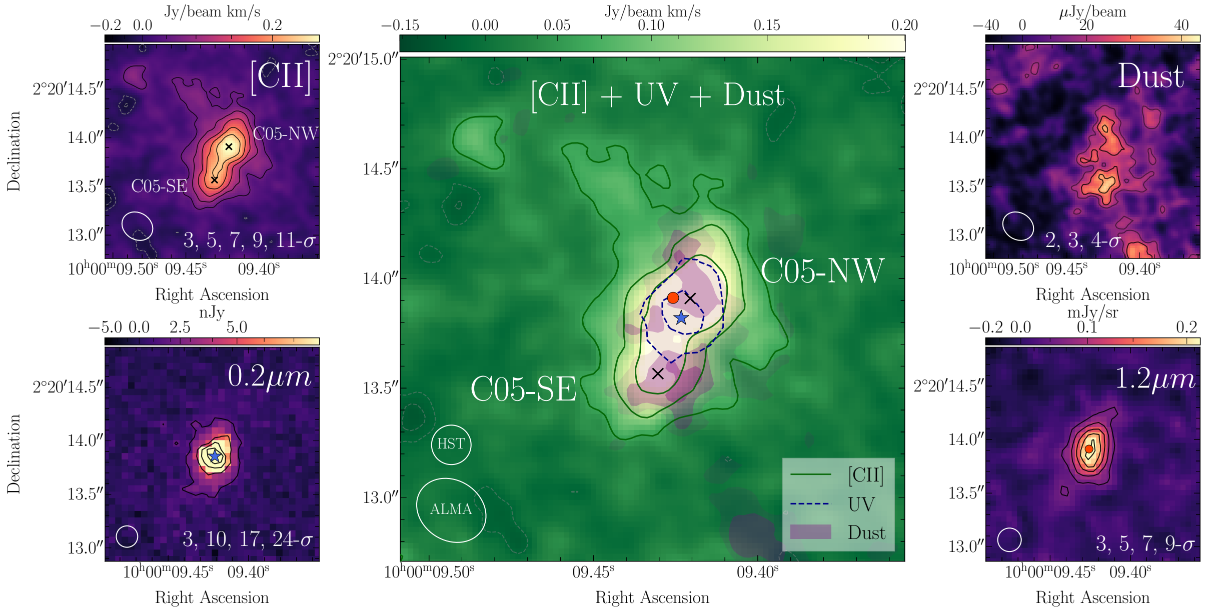

Figure 3.2: Multi-wavelength cutout postage stamps toward CRISTAL-05 . (a) Left upper panel: ALMA [C II] moment-0 map (non-JvM corrected). The overlaid black contours correspond to the 3, 5, 7, 9, and 11-$\sigma_{\rm [CII]}$ levels, where $\sigma_{\rm [CII]} = 0.02$ Jy/beam km s^{-1} is the rms noise level. The white ellipse indicates the beam size of $0.33'' \times 0.27''$. (b) Left bottom panel: HST F140W rest-frame UV (0.2μm) continuum image. The overlaid contours correspond to the 3, 10, 17, and 24-σ_{UV} levels. The white circle indicates the $0.2''$ point spread function. (c) Right upper panel: ALMA rest-frame 160μm dust continuum image. The overlaid contours correspond to the 2, 3, 4-σ_{160}. The white ellipse indicates the beam size of $0.33'' \times 0.27''$, the same as the [C II] moment-0 resolution. (d) Right lower panel: JWST F770W (1.2μm) rest-frame near-infrared image. The black contours correspond to 3, 5, 7, 9-$\sigma_{1.2}$.

The JvM-corrected [C II] spectrum is shown in Figure 3.1 (red solid line), and the best-fit single Gaussian as the black line. The moderate goodness of the fit ($\chi^2 = 6.5$) is explained by the heavy-tail shape of the [C II] distribution, with a blue-wing around v < -100 km s^{-1}.

The dust emission was measured by Mitsuhashi in prep., yielding a flux density of $S_{158\mu m} = 0.118 \pm 0.021$ mJy and a significance of S/N = 6.7. The global properties of the CRISTAL-05 such as central frequency, line width, and integrated flux presented in Tab. 3.2 are consistent with the values recovered in previous observations (Capak et al., 2015; Le Fèvre et al., 2020).

3.3.2 MULTICOMPONENT MORPHOLOGIES

Previous ALMA observations (Capak et al., 2015) obtained a significant, yet mostly unresolved ($0.9'' \sim 5.3$ kpc) detection of the [C II] emission line in CRISTAL-05 , but no detection of the underlying dust continuum. Our data set improves the analysis at a resolution of $0.3''$ ($\sim$ 2 kpc, natural weighting). In this section, we characterize how star formation (as traced by FIR and rest-frame UV), stellar content (rest-frame optical), and cold gas are distributed across the CRISTAL-05 system.

The moment-0 traces the distribution of the global [C II] line emission, thus providing information about the morphology of the gas in the galaxy. Figure 3.2 shows the [C II] moment-0 map collapsed over the full-width tenth maximum of the [C II] line (upper left panel), the rest-frame UV at 0.2μm (traced by the HST F125W-band image; bottom left), the rest-frame FIR dust continuum emission at 160μm (traced by the observed 850μm continuum; top right), and the rest-frame near-infrared at 1.2μm (traced by the JWST F770W image; bottom right). The central main panel gathers the information on all the different wavelengths.

The [C II] emission is spatially extended across $\sim$ 10 resolution elements. The emission is elongated from the southeast to the northwest and shows an asymmetric shape. We also find emissions with significance greater than 3σ extending from the main source towards the northeast. Moreover, the peak emission is found close to the northwest side of CRISTAL-05 . Inspection of the integrated map obtained with Briggs weighting and robust parameter of 0.5 (Appendix B.3) yields the identification of two nuclei or peaks in the image (as black crosses in the top left and central panels of Fig. 3.2).

The disturbed double nucleus shape of the galaxy and its asymmetric emission indicate that this is a potential merging system, missed by previous low-resolution observations. The separation between the two emission peaks (in the Briggs image, with ROBUST = 0.5) is $\sim$ $0.4''$ ($\sim$ 2.4 kpc), smaller than the resolution of previous studies $1'' \sim$ (6 kpc). In the following sections, we refer to the northern peak as the C05-NW clump and the southern peak as the C05-SE clump.

Contrary to the [C II] emission, the rest-frame UV image (bottom left panel in Fig. 3.2) shows a compact single source, slightly elongated in the north-south direction. The peak of the rest-UV emission, shown as a blue star in the left-bottom and central panels of Fig. 3.2, is closer to the C05-NW clump ($0.1'' \sim$ 0.6 kpc) than the C05-SE clump ($0.3'' \sim$ 1.8 kpc). However, the rest-UV emission extends in the region between both [C II] source peaks (blue dashed line in the central panel of Fig. 3.2)

Dust continuum emission is detected with a lower significance than [C II] (peak S/N$\sim 3\sigma$)

throughout the system. Two components are detected and aligned in the north-south axis, similar to the [C II] emission. As shown in the central panel of Fig. 3.2, the rest-UV emission peaks right in between the two dust components or clumps, which closely follow the location of the [C II] C05-NW and C05-SE clumps. This suggests that dust obscuration can be responsible for the compactness of the rest-frame UV emission.

Also shown in Fig. 3.2 is the JWST 1.2μm image, which traces the rest-frame NIR close to the peak of the stellar emission at $z = 5.5$ (rest-frame 1.8μm). This stellar emission is clearly detected and, as with the rest-frame UV, is found to be compact, elongated along the direction of the [C II] emission, and located in between the dust and [C II] clumps.

3.3.3 RADIAL PROFILES

CRISTAL-05 has compact star-forming and stellar components in comparison with the gaseous [C II] emission. The following step is to quantify these extensions by comparing the surface brightness radial profiles and effective radii of each structural element. Since the [C II] , rest-frame UV and near-infrared images have different point spread functions, we matched the resolution of the HST, JWST, and ALMA maps to that of the lowest among them (ALMA), yielding a final beam size of $0.33 \times 0.27''$ (2.0×1.6 kpc^2).

We first compare the spatial distribution of the different components in the top panel of Figure 3.3. Highlighted as solid-filled regions, we show the areas containing half of the total flux density for the [C II] (violet), HST/F125W (yellow), and MIRI/F770W (dark-red) images, respectively. The dashed (violet), dash-dotted (yellow), and dotted (dark-red) lines represent the 3-σ flux level of each observation. From this comparison, we find that the [C II] emission is more extended than the rest-frame UV and near-infrared emission traced by the HST and JWST bands. Based on visibility modeling, assuming a Sérsic elliptical exponential profile with a Sérsic index of $n = 1$ (Ikeda et al. in preparation), results in a circularized effective radius of $r^{\rm cir}_{\rm [CII]} = 1.6 \pm 0.3$ kpc. However, similar modeling of the rest-frame UV emission yields $r^{\rm cir}_{\rm HST/F160W} = 0.36 \pm 0.02$ kpc (Mitsuhashi in prep.) for the HST/F160W. This makes the [C II] emission ~ 4 times larger than the rest-frame UV).

To further inspect the distribution of the [C II] , rest-frame average UV and optical emission,

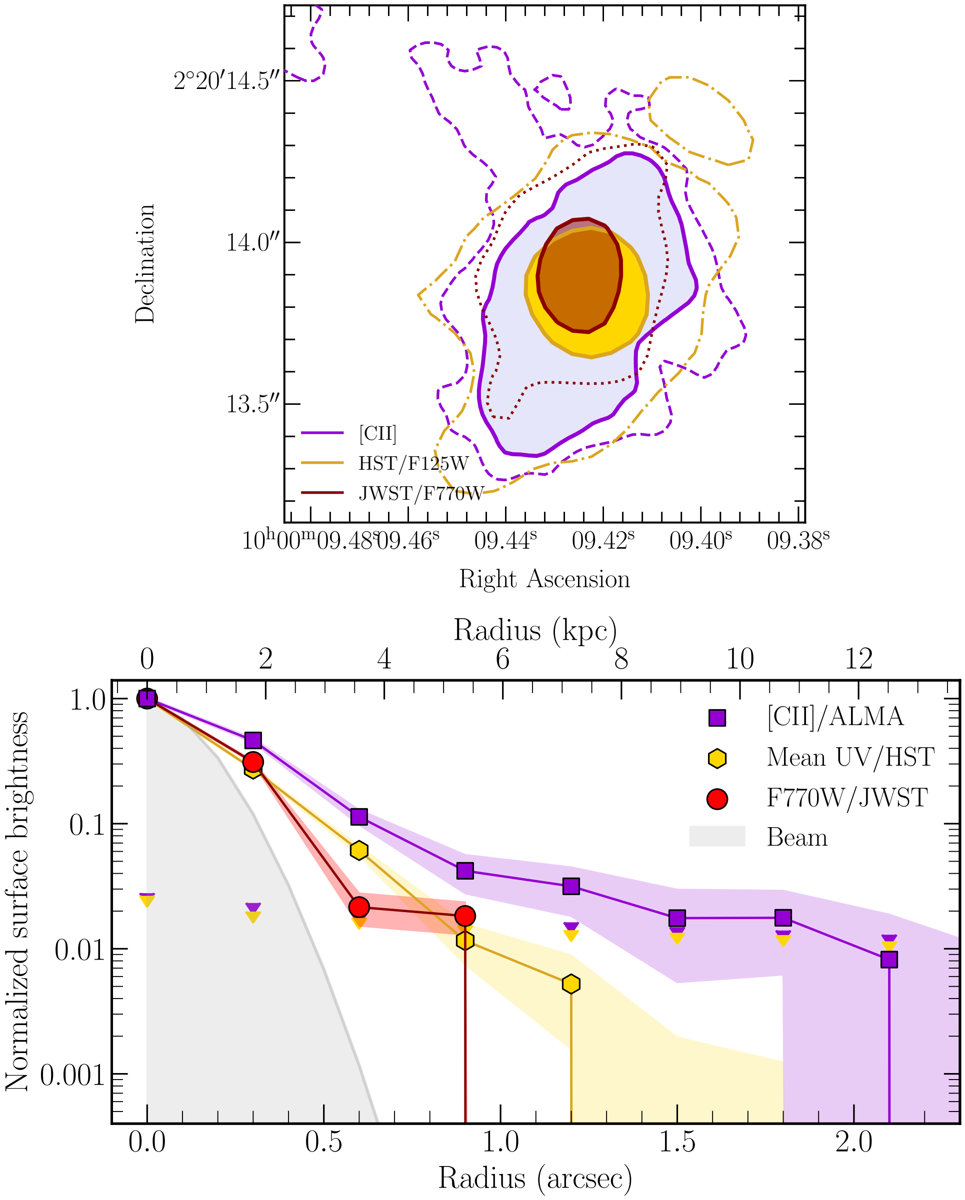

Figure 3.3: Comparison of the multi-wavelength radial profiles. (a) Top: Resolution-matched (0.33″ x 0.27″) moment-0 maps. The [C II] , HST, and JWST are color-coded by purple, yellow, and dark red, respectively. The solid lines correspond to the significance levels, which contain half of the total flux density of the galaxy. The dashed, semi-dashed, and dotted lines correspond to the $3-\sigma$ edge of the source in [C II] , rest-frame UV, and rest-frame NIR, respectively. (b) Bottom: Surface brightness profiles of [C II] and (average F105W + F125W + F140W + F160W) UV emission, in 0.3″-width elliptical apertures all centered in the [C II] centroid. The purple and yellow arrows show 1σ upper limits.

we computed radial profiles as shown in Fig. 3.3 (bottom), respectively seen as violet squares, yellow hexagons, and red circles. We calculate the flux in elliptical annuli with a width of $0.3''$ centered at the [C II] centroid, and divide the flux by the area of the aperture and then normalized by the value of the first aperture. The shaded area for each radial profile represents the 1-σ uncertainty in these measurements. We find that the [C II] emission is more extended than the emission in the rest frame UV and near-infrared bands, extending significantly to 10 kpc, beyond which the [C II] emission is dominated by noise. Beyond 12 kpc, the emission of [C II] is undetected. The radial profiles of both the HST and JWST bands are consistently similar out to 4 kpc, beyond which the JWST/F770W flux falls below the noise level. This result confirms the measurements based on the visibility modeling of the emission distribution and is consistent with recent findings of extended [C II] "halos" in massive star-forming galaxies at these redshifts.

3.3.4 MOMENTS-1 MAPS AND PV-DIAGRAM

In this section, we analyze the dynamical conditions of the gas. We created intensity-weighted velocity maps (moment-1) and intensity-weighted dispersion velocity maps (moment-2) of the [C II] emission, which are shown in the left panels of Figure 3.4. Additionally, we generated a position-velocity diagram that shows how the gas motions change as a function of the position along a predefined slit, which is typically used to search for kinematical features such as outflows. We set a slit along the major axis of the CRISTAL-05 system, with a width of 10 pixels $\sim 0.245''$.

The moment-1 emission map (left panel in Fig. 3.4) reveals that the line-of-sight velocity of the gaseous component is not smoothly distributed across the main system. The velocity range of CRISTAL-05 varies mainly from -50 to 50 km/s, and such a low peak velocity indicates a nearly face-on merger. If we focus on the central region encompassing both sources (within the contour greater than 6-σ), there is a velocity gradient along the major axis for each source. The moment-2 map shows a homogeneous but high mean dispersion velocity of 79 ± 21 km s^{-1}. An inspection of the position-velocity diagram (right panel of Fig. 3.4) reveals that CRISTAL-05 has a complex kinematical structure composed of at least two components and disturbed

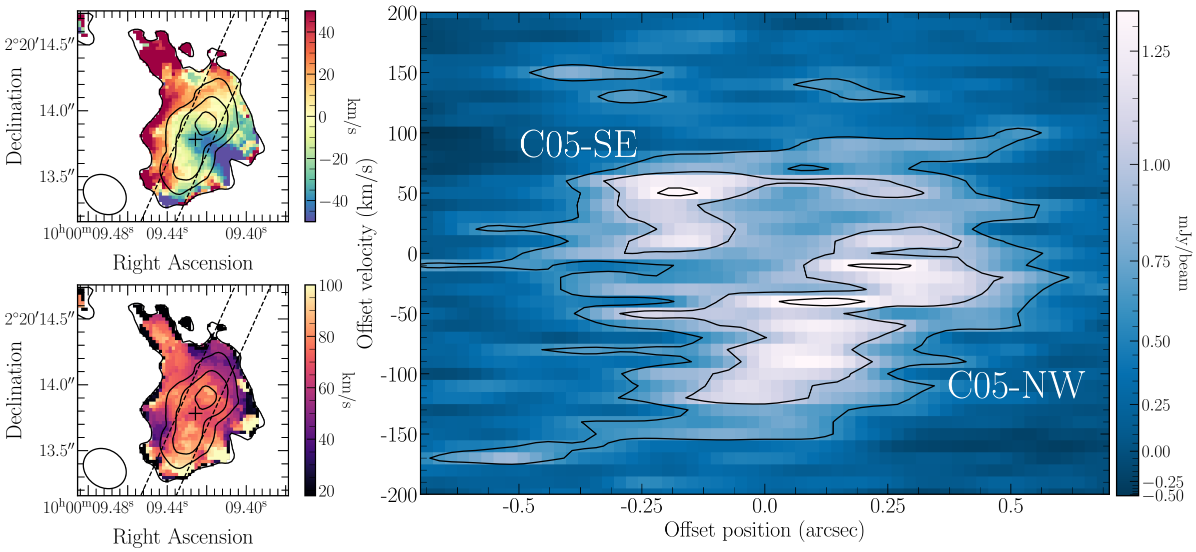

Figure 3.4: Kinematics of the [C II] emission for CRISTAL-05 . (a) Upper and (b) bottom left panels: it is respectively showing the velocity (moment-1) and dispersion (moment-2), with respect to the observed frequency of [C II] at redshift z = 5.54. The black contours correspond to the 3-, 6-, 9-, 12-σ levels of the [C II] moment-0 map. The black dashed line shows the slit in which we created the position-velocity diagram in the right panel, with the center of the slit as a black cross.(c) Right panel: Position-velocity diagram along the major axis of CRISTAL-05 with a width of 0.245″ . The black contours represent the 3-, 5-, 7-σ_{p-v}.

carbon-rich gas surrounding the central system. We can easily pinpoint the two components C05-NW and C05-SE , as identified in the previous section. The component C05-NW extends along 0.7″, equal to a physical size of ≈ 4 kpc, and in a velocity range nearly from -150 $\mathrm{km\,s^{-1}}$ to 30 $\mathrm{km\,s^{-1}}$. This is the most extended and broad component, suggesting that this is the dominant object in the system. The component has a disturbed shape, likely caused by the proximity of C05-SE . The C05-NW component shows the peak of the emission moving in velocity at different positions along the slit. This gradient in velocity is commonly interpreted as a signature of rotation or, alternatively, two unresolved interacting objects (Förster Schreiber & Wuyts, 2020). In the next section, we will investigate the nature of C05-NW . Finally, the second subdominant component C05-SE is more compact and narrower in the velocity axis, extending for 0.275″ and with $\Delta v \sim 60$ $\mathrm{km\,s^{-1}}$.

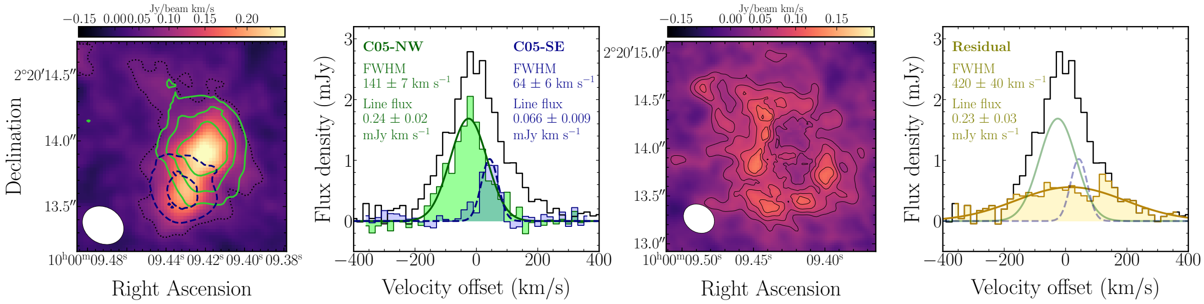

Figure 3.5: Morphologies and spectra of the individual galaxies and extended emission. [From left to right] (a) First panel: [C II] moment-0 map of CRISTAL-05 , similar to the central panel of Figure 3.2, with C05-NW and C05-SE maps overlaid as solid green and dashed navy lines, respectively (as 3-, 9-, 15-σ_{rms}). (b) Second panel: Spectra of CRISTAL-05 (black line), C05-NW (green line) and C05-SE (navy line). The Gaussian distribution represents the best fit for the spectra of C05-NW and C05-SE , with a FWHM of 141 ± 7 and 64 ± 6 $\mathrm{km\,s^{-1}}$, respectively.

3.3.5 CLUMPINESS AND EXTENDED EMISSION FRACTION

The [C II] moment-0 map and position-velocity diagram reveal that CRISTAL-05 is indeed a complex interacting system comprising at least two galaxies projected along the same line of sight. In this section, we aim to disentangle the components of CRISTAL-05 to investigate the number of individual constituents of the system. Additionally, we measure the fraction of the [C II] luminosity associated with the gas surrounding the merging pair.

We performed a search for structures based on a gradient-tracing scheme with the Fellwalker algorithm (Berry, 2015). In brief, the algorithm walks around pixels in the 3D cube that surpasses a specific threshold (determined by the NOISE parameter). It searches for paths with the steepest ascents, i.e. it continually jumps from a giving pixel to the immediately neighboring pixel with the highest value until it finds the peak of the path. All paths reaching the same peak pixel are associated with the same clump. To define the starting point of each path, the algorithm considers only the section with an average gradient over four pixels greater than a threshold (determined by the FLATSLOPE parameter). Once a peak is found, the code expands its search to a broader neighborhood (defined by the MAXJUMP parameter) to check if there are pixels with higher values, thus avoiding noise spikes that may create local maxima. Merging occurs when the pixel value difference between the two adjacent peaks is less than a certain threshold (defined by MINDIP); in such cases, the peaks are considered part of the same clump.

We start the clump search with the hypothesis that only two or three clumps are present, based on the visual inspection of the position-velocity diagram (Figure 3.4). All runs were performed in a version of the data cube with a channel resolution of 10 km s^{-1}. We note that the final results are significantly influenced by the choice of key parameters and the ones that primarily affect clump detection are MINDIP, MAXJUMP, and MINPIX (the minimum number of pixels a clump must contain). To minimize the influence of these parameters, we set MINPIX to 16 pixels to eliminate obvious noise spikes. We determined FLATSLOPE as 2×rms based on several tests, as no significant differences were observed in the output. To mitigate the impact of MINDIP and MAXJUMP, we performed several runs varying the parameters in the range of [1, 2, 3]-σ_{rms} and [4, 6, 8] pixels, respectively. For all the scenarios, the algorithm retrieves a total number of 2 clumps. Three clumps can only be found if the smallest dip in height allowed (MINDIP) is below 1-σ. It means that the difference between the flux of the two peaks of C05-NW is not significant enough to be considered as two independent components. In conclusion, our analysis favors the scenario that CRISTAL-05 is composed of two components, as previously named as C05-NW and C05-SE .

In Figure 3.5, we display integrated maps and spectra after the clump extraction relative to the whole system. From left to right, the first panel shows the [C II] moment-0 map integrated over the full velocity range covered by the CRISTAL-05 system (same as Figure 3.2). Green and dashed navy blue contours show the integrated emission of C05-NW and C05-SE . In the second panel, we present the spectra of the whole system and of each of the identified individual clumps. There is significant additional emission not accounted for by the two identified clumps. To pinpoint its location, we subtract the emission from the two clump-based identified components (C05-NW and C05-SE) and compute the moment-0 map, which is shown in the third panel. Most of the compact emission in the central region is removed, and only extended emission is left in the surroundings of the galaxy. The fourth panel shows the spectrum of this extended emission component compared to the spectra of the full system and of each of the clumps. We find that the C05-NW , C05-SE , and extended components contribute 46%, 13%, and 41% of the total [C II] emission of the system, respectively.

The components segmentation shows that a substantial fraction of the total [C II] line emission comes from the residual emission after subtracting the C05-NW and C05-SE . However, the interpretation of such extended emission being an independent third component isolated from the other two is not straightforward. It could be that the two compact components have extended tails on their gas distribution and, because of the lower signal-to-noise, they are not associated with the central regions by the Fellwalker algorithm. Independently of the segmentation of the emission, it is clear that there is an extended [C II] emission with two brighter and compact central components.

3.3.6 KINEMATIC MODELLING

C05-NW agrees with the main observational signatures of a rotating disk given the criteria commonly used in the literature (Förster Schreiber & Wuyts, 2020): (i) a smooth monotonic velocity gradient across the galaxy, (ii) nearly co-location of the kinematical and morphological centers, and (iii) co-alignment of the morphological and kinematic major axes. Therefore, we assume that C05-NW has a rotating gaseous disk to check if the component represents an early rotating disk that is facing strong gravitational interactions with C05-SE .

We thus perform galaxy kinematics modeling in the C05-NW with the parametric 3D software DYSMALpy (Price et al., 2021). This code employs a multi-component 3D model to compare with the observed spectroscopy cube via MCMC minimization, accounting for observational effects such as beam smearing and instrumental line broadening. We choose the 1-d approach to simultaneously model the radial and dispersion velocity curves along the major axis of the galaxy since it contains most information of the intrinsic rotation curve (Price et al., 2021).

In the left panel of Figure 3.6, we show the position-velocity diagram in the cube masking out the C05-SE and extended emission. We created the rotation curves by fitting a Gaussian distribution in each column of the position-velocity diagram. The procedure is complex since the component has features caused by the gravitational instabilities of the interaction, requiring either mask out in the cubes or adopting two Gaussian fittings in a giving column. The peaks from the Gaussian fitting, which correspond to the radial velocity of the rotating curve, are plotted as black circles, and the error bars correspond to the dispersion of each column.

In the central and right panels of Figure 3.6, we show the radial and dispersion velocity

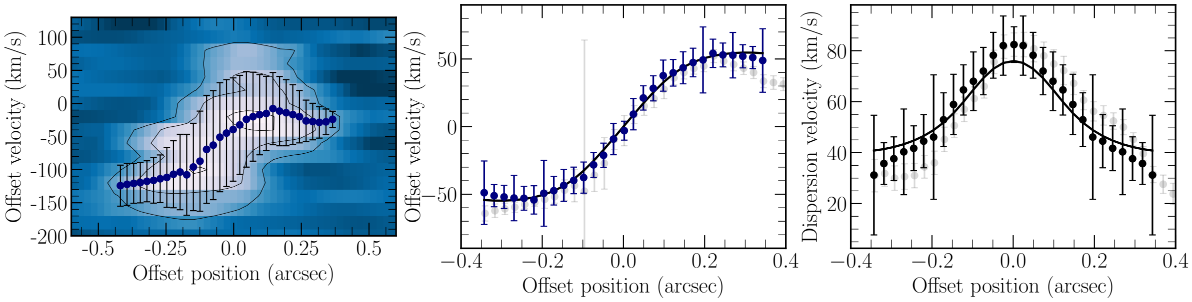

Figure 3.6: Radial kinematics curves of C05-NW as an input for DYSMALpy. (a) Left panel: Position-velocity diagram in an extracted-C05-NW cube, with a slit along the major axis with a width of 0.245$''$. The navy circles are the peak velocity of the Gaussian distribution in each position, and the black error bars are the dispersion of the distribution. These curves were symetrized and presented in the central and right panels, respectively. (b) Central panel: Symmetrized rotation radial profile of C05-NW as navy circles. The background gray circles are the not-symmetrized curve, shown as navy circles in the left panel. (c) Right panel: Symmetrized dispersion velocity radial profile of C05-NW as black circles. The background gray circles are the black error bars in the left panel before being symmetrized.

curves (in purple and black points, respectively), which were symmetrized as an input to DYSMALpy. This was motivated by the considerable asymmetries beyond 0.2$''$ in both curves. The radial velocity peaks at 0.2$''$ and C05-NW is very compact and barely resolved, with an effective radius of $\sim$ 700 pc ($\sim$ 0.12 $''$). This means that the curves extended up to $2.5 \times \mathrm{R_{eff}}$, even though it corresponds to a size similar to that of the beam size.

The mass model consists of a thick disk, a bulge, and a dark matter halo. The parameter selection is summarized as follows:

a) Dark matter mass distribution: It follows a Navarro-Frenk-White profile (Navarro et al., 1996), with a fixed concentration c as 3, according to what is expected to this redshift (Dutton & Macciò, 2014). We let the dark matter fraction at the effective radius as a free parameter with an initial guess of 0.5 and a flat prior. We do not assume an adiabatic contraction of the halo.

b) Baryon mass distribution (disk+bulge component):

We let the total baryonic mass as a free parameter with an initial guess of log $\mathrm{M_*/M_\odot}$ = 10.5, by the sum of the stellar mass log $\mathrm{M_*/M_\odot}$ = 10.27 obtained by Capak et al. (2015), and the gas mass assumption of log $\mathrm{M_{gas}/M_*}$ = 0.75 (Dessauges-Zavadsky et al., 2020). We set it with a Gaussian prior varying in a wide range $\mathrm{M_{gas}/M_*} \in [9.5{,}11]$. This choice is based on the fact that stellar mass estimation assumes that CRISTAL-05 is a single source since it is

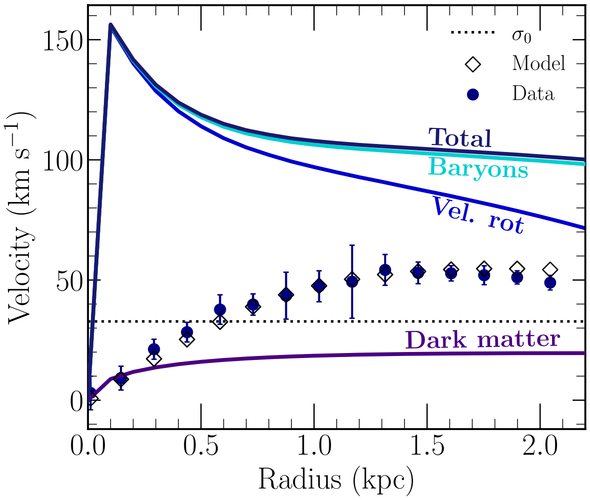

Figure 3.7: Intrinsic circular velocity and rotation velocity profiles of C05-NW for the best-fit model of DYSMALpy. From top to bottom, we show as solid lines: the intrinsic circular velocity of total mass distribution (baryon + dark matter component, navy color), the intrinsic circular velocity of the baryons (gas + stars, cyan color), rotation velocity curve of the total mass distribution (baryon + dark matter, blue color), the intrinsic circular velocity of the dark matter mass distribution (dark violet color). All the curves are inclination-corrected. As a reference, the intrinsic velocity dispersion is plotted as dotted black lines. The symmetrized rotation curve, the same as Figure 6, is plotted as navy circles, and the white diamonds show the best-fit model. Both rotation curves are not inclination-corrected.

unresolved in the HST imaging (Capak et al., 2015).

Our choice of a disk+bulge mass modeling is motivated by the failure of initial tests in fitting just a disk component. We assume a fixed bulge-to-light ratio of 30%. The disk component follows a Sersic profile with a fixed Sersic index n = 1 and the effective radius is left free with an initial guess of 1 kpc and a Gaussian prior varying in [0.5,3] kpc. For the bulge component, we fixed the Sersic index and effective radius as n = 4 and r_{eff} = 0.15 kpc. The thick disk requires an asymmetric drift correction following Burkert et al. (2010). Finally, we assume that the dispersion velocity is isotropic and constant along the galaxy, so we add an initial guess of 40 km s^{-1} with a flat prior varying from [5,100] km s^{-1}.

(c) Geometry: We fixed the kinematic center and position angle based on the moment-0 [C II] emission. The inclination was set as 60°, according to the axial ratio of the moment-0 map.

In summary, the free parameters are the dark matter fraction tied with the virial mass, disk effective radius, and dispersion velocity. We ran with 1000 walkers and a burn phase of 50 iterations, which led to the following best fit: log $M_{bar} = 9.78^{+0.09}_{-0.14}$ $M_{\odot}$, $r^{eff}_{disk} = 1.6^{+0.6}_{-0.6}$ kpc, darf mater fraction at the effective radius fdm = $0.03^{+0.14}_{-0.03}$ and $\sigma_0 = 33^{+2}_{-3}$ $\mathrm{km\,s^{-1}}$.

In Figure 3.7, we display the intrinsic circular velocity curves of the total, baryon, and dark matter components. The intrinsic circular velocity peaks at 100 pc, with a velocity of 150 $\mathrm{km\,s^{-1}}$, and it remains flat at $r > 0.6$ kpc for a value of ~ 110 $\mathrm{km\,s^{-1}}$. The dark matter contribution remains small at all radii. This is a good fit for the velocity curve (χ^2 = 0.63) but moderate for the dispersion velocity curve (χ^2 = 2.6). The kinematical modeling could retrieve a rotating gaseous disk in a compact source, mainly baryon-dominated. At distances greater than the beam size, the rotation-to-dispersion is $V/\sigma_0 \sim 3$, which meets the criteria broadly used to distinguish rotation- and dispersion-dominated systems. However, the main axis of the galaxy is resolved over 2.5 beam sizes, therefore we can not ultimately rule out that C05-NW is actually a compact merger whose nuclei are closer than 2 kpc.

3.4 DISCUSSION

In the previous section, we concluded that CRISTAL-05 is a nearly face-on interacting system composed of at least two components with disturbed gas surrounding the central source. Although having a compact UV and stellar continuum, its [C II] emission extends up to 10-12 kpc, and the residuals of the [C II] emission around the central double source account for 41% of the total [C II] emission. In this section, we discuss the possible nature of CRISTAL-05 and the origin of the extended [C II] emission around it.

3.4.1 CRISTAL-05 AS AN ONGOING MERGING SYSTEM

We measure the dynamical mass to check the nature of the system. We calculate the dynamical mass by $M_{\mathrm{Dyn}} = \gamma R v^2/G$ in units of $M_\odot$ (Spilker et al., 2015, 2022), where G is the gravitational constant $G = 4.32 \times 10^{-6}$ $\mathrm{km\,s^{-1}}$ kpc $M_\odot$, R is the radius (in units of kpc), v the velocity of the system in $\mathrm{km\,s^{-1}}$ and γ is the pre-factor which accounts for the geometry of the system (Spilker et al., 2022). The radius R is assumed to be the circularized radius from a beam-corrected Gaussian fitting on the moment-0 map of each component. For C05-NW, we assume the velocity v = 120 $\mathrm{km\,s^{-1}}$ at R = 1.5 kpc, where the rotation curve is flat (Fig. 3.7). For C05-SE, since the system is dispersion-dominated, we assume $\gamma = 5$ (Spilker et al., 2022) and $v \sim \sigma$ of the system. It results in a dynamical mass of $M_{dyn}^{NW} = 5 \times 10^9$ $M_\odot$, $M_{dyn}^{SE} = 9.1 \times 10^8$ $M_\odot$, which are consistent with the value estimated for C05-NW in section 3.3.6 and the dynamical mass of typical galaxies at z = 5.5 (Spilker et al., 2022). It leads to a mass fraction of $M_{dyn}^{SE}/M_{dyn}^{NW} = 0.2$, which is considered a minor merger.

Assuming a fiducial gas fraction of unity, we can estimate that the stellar mass of C05-NW is $\sim 2.5 \times 10^9$ $M_\odot$, which is in the middle of the range of stellar masses measured at similar redshifts (Grazian et al., 2015; Song et al., 2016; Navarro-Carrera et al., 2023).

3.4.2 [C II] EXTENDED EMISSION

Several studies in the literature refer to [C II] haloes in early galaxies as the existence of carbon-enriched gas surrounding the galactic disk where most of the star-forming activity takes place. The typical sizes of 6-12 kpc (Fujimoto et al., 2020; Herrera-Camus et al., 2021; Akins et al., 2022) of these gaseous components exceed the effective radius of UV emission (1-3 kpc, Fujimoto et al., 2020), reaching the circumgalactic medium, loosely defined as the gas beyond the 1 - 2 × the effective radius of the galactic disk out to the virial radius. It suggests that the circumgalactic medium is also composed of a cold gas phase, in addition to the usual hot and warm gas (Tumlinson et al., 2017, and references in), as a result of galactic-scale processes such as nuclear, and stellar outflows and intergalactic gas accretion.

It is well known that the [C II] emission is associated with the star formation activity of local and distant galaxies (De Looze et al., 2014; Herrera-Camus et al., 2015b; Carniani et al., 2018b) since this is the major cooling line of stellar heating, in different gas phases (Stacey et al., 2010). The lack of heating sources to generate this emission at far distances requires some physical mechanism to transport the carbon produced by the stellar nucleosynthesis to the outskirts and constantly excite the singly ionized phase.

Currently, there are two different approaches to identifying a [C II] halo: (i) the first one was adopted by Fujimoto et al. (2020), where a galaxy contains a [C II] halo when $R_{[CII]}^{eff} > R_{UV}^{eff}$ and it has a [C II] intensity in the outskirts of the galaxy greater than 4-σ for [C II] , but below 3-σ for the UV continuum. This extended area is delimited by an aperture radius of 10 kpc, masking out the emission within a beam area centered at the source peak emission. (ii) the second one also adopted by Fujimoto et al. (2020) and kpc-resolved studies (Herrera-Camus et al., 2021; Akins et al., 2022) claims a [C II] halo when $R^{eff}_{[CII]} > R^{eff}_{UV}$ and there is a significant intensity gap between the normalized surface brightness radial profiles of [C II] and UV emission, beyond the noise level.

According to both definitions, Fujimoto et al. (2020) defined CRISTAL-05 as having a [C II] halo. Since the first approach depends on the relative sizes of the galaxy and the beam, we stick to the second one which evaluates the relative morphologies and extension of the different emissions. The higher resolution and depth of our observations confirm the extended nature of [C II] extended emission compared to both the rest-UV and optical continuum, at least to 10 kpc. The detection of a [C II] halo so far assumes that the rest-UV emission from HST observations is a good tracer of the galactic disk. However, rest-frame UV observations can be affected by dust obscuration and thus not necessarily trace the galaxy star formation distribution. Moreover, it is well known that the star-forming regions tend to be more compact and it not necessarily trace the mass distribution of a galaxy (Pallottini et al., 2022; Ferreira et al., 2022). Thus, the rest-UV emission is not enough to specify the galactic disk extent, and therefore, information on the stellar spatial distribution is also required. Hence, we also added the available JWST/F770W-band imaging of CRISTAL-05 , which at z = 5.54 traces the emission close to the peak of the stellar continuum. Similarly to the UV-continuum, the stellar emission is compact (Fig. 3.3), reinforcing the extended nature of [C II] in CRISTAL-05 .

We thus describe the main physical mechanisms proposed in the literature to explain the origin of the [C II] extended emission (Fujimoto et al., 2019; Ginolfi et al., 2020a; Akins et al., 2022):

1. Satellite galaxies - a non-neglected number of low-mass galaxies reside spatially around the massive galaxy and the [C II] emission arising from stellar heating in these smaller systems is diluted by the current resolution of observations, therefore mimicking an extended emission.

2. Cold streams - intergalactic gas streams flow toward the potential well of the central massive galaxy. [C II] emission is the product of gravitational energy and/or shock heating.

3. Outflows - high-speed interstellar gas flows outwards the potential well of the massive

galaxies as a product of AGN and/or stellar feedback.

4. Bridges and tidal tails by mergers - the cooling of [C II] release emission via kinematic energy dissipation in a turbulent cascade from large to small scales.

Our high-resolution observations provide evidence of the merger nature of CRISTAL-05 , supporting scenario (4) as the main explanation for the presence of [C II] emission beyond $\sim$ R_{UV}^{eff}. Simulations point out that satellites in minor mergers can disrupt the gas in low-mass galaxies (Kohandel et al., 2020; Akins et al., 2022). This result impacts the detection and analysis of the current properties of galaxies with [C II] halos. In the ALPINE survey, Fujimoto et al. (2020) considered only galaxies classified as non-mergers to avoid the obvious [C II] emission caused by shock heating in tidal stripping gas. Following this criterion, they concluded that 30% of the single ALPINE sources are classified as containing a [C II] halo ($>$ 4-$\sigma_{[CII]}$ and $>$ 3-σ_{UV} in the outskirts of the galaxies). Comparing both samples, galaxies with haloes are more massive and starbursting and have most likely past/ongoing stellar-driven outflow episodes to form this kind of haloes. A similar analysis by (Fujimoto et al., 2019) could not reproduce the [C II] excess in surface brightness radial profiles of the stacked observations of the ALPINE survey in state-of-art cosmological simulations (Pallottini et al., 2017; Yajima et al., 2017). Our results suggest that at least a fraction of the galaxies with a [C II] halo that are located in the bright end of the SFR-M* relation could be multi-component systems misclassified as individual galaxies. In such cases, the SED fitting on the non-resolved sources took into account the summed photometry of the system that can mimic a more luminous, and thus more massive system. For these sources, the tension between observational and cosmological simulation breaks since we are analyzing objects with different dynamical natures.

This outcome highlights the need for high-resolution observations to ultimately distinguish isolated galaxies from mergers, requiring at least three beams along the major axis and a S/N $>$ 10 (Rizzo et al., 2022). A face-on close encounter, such as CRISTAL-05 , imprints a low-velocity gradient in moment-1 and position-velocity diagrams, requiring a higher spatial and spectral resolution to efficiently separate two or more components.

Other examples in the literature also support merger activity as the cause of [C II] extended emission. Ginolfi et al. (2020a) observed that 50% of the [C II] emission in a merging system at z $\sim$ 4.6 comes from the stripped gas surrounding the system composed of two massive galaxies and a few low-mass satellites. The typical star-forming galaxy HZ7 at z = 5.25 also contains a [C II] extended emission (Lambert et al., 2023) with no evidence of a broad secondary component in the [C II] spectrum across the galaxy, as evidence for outflows. Instead, the disturbed integrated gas and dust emission and velocity field points to a late-state merger. Similarly, the strongly lensed sub-L* galaxy A1689-zD1 at z = 7.13 also has a [C II] halo, with signs of being a multicomponent system (Akins et al., 2022).

3.4.3 SHOCK HEATING EXCITING THE EXTENDED [C II] EMISSION

The [C II] arises from regions surrounding the star-formation regions, mostly from the photodissociation regions. Considering a thermal balance, a correlation of the [C II] emission and the star-forming activity is valid for both local and high-redshift galaxies (De Looze et al., 2014; Herrera-Camus et al., 2015b; Carniani et al., 2018b; Schaerer et al., 2020), and a positive deviation indicates the need for an additional mechanism that enhances the [C II] emission. Our results for CRISTAL-05 resemble the [C II] emission origin in tidal tails and bridges of low-redshift merging galaxies. In particular, Appleton et al. (2013) found an excess in the [C II] -to-PAH and [C II] -to-FIR luminosities ratios in a pure-shock region of the Stefan Quintet (SQ), arguing against purely photoelectric-heated gas in photodissociation regions. Hence, an excess in [C II] /FIR ratio compared to normal galaxies can yield evidence for possible shock heating in a given system. The excess in the SQ shock gas is shown in Figure 3.8. A similar case is identified in the bridge between the local merging Taffy galaxies (UGC 12914/12915) (Peterson et al., 2018), also shown in Figure 3.8. The [C II] luminosity reaches 2-10% of the total far-IR emission, which contrasts with the fraction in normal galaxies and local LIRGs nuclei (darkgreen triangles and grey circles, Malhotra et al., 2001; Díaz-Santos et al., 2013).

We explore this scenario by evaluating how the [C II] emission varies relative to the star formation (as probed by UV + IR emission) across the galaxy in apertures with the same width of the beam size (r $\sim 0.17'' \sim$ 1 kpc), in Fig. 3.8. The apertures were selected to isolate the different features of the galaxy. As we can see in the [C II] moment-0 map, regions 0 to 7 comprise the area around the central sources, with region 0 tracking the UV-dark emission

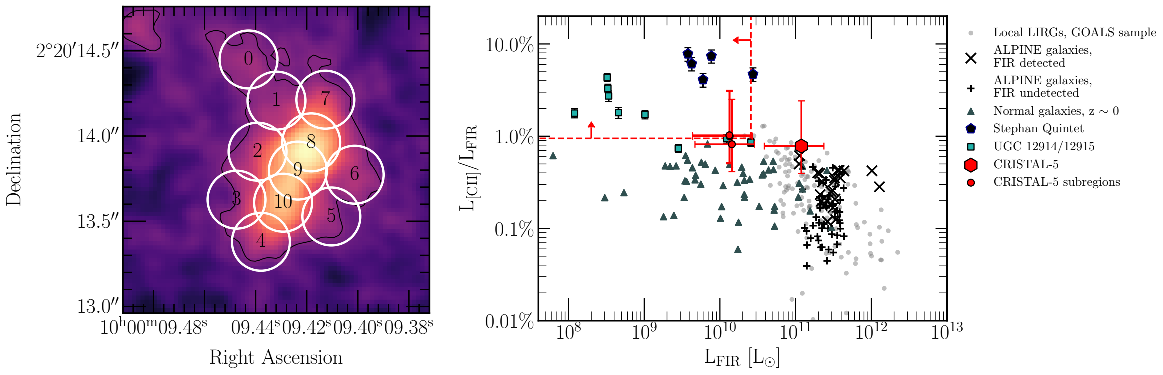

Figure 3.8: (a) Left panel: [C II] moment-0 map, same as Figure 3.2, with 0.17″-width apertures across the galaxy (white circles). The emission extracted is analyzed in the right panel and Figure 3.9. (b) Right panel: [C II] -to-FIR luminosity ratio, as a function of the FIR luminosity. The global measurement (aperture of 1.5″) is shown as a red hexagon, and the subregions 8, 9, and 10 are shown as red circles. The uncertainties reflect the possible dust temperature range between 30 and 60 K. The red area locates the upper limits of the mean of the ratios. As a comparison, we also reference to $z \sim 0$ LIRGS of the GOALS sample (gray circles; Díaz-Santos et al., 2013), $z \sim 0$ normal galaxies (darkgray triangles; Malhotra et al., 2001), a purely shock-gas region in the Stephan Quintet compact group (navy pentagons; Appleton et al., 2013), shock-gas in the bridge of the merging pair UGC12914/12915 (cyan squares; Peterson et al., 2018), and $4 < z < 6$ typical galaxies from the ALPINE galaxies (IR detected sources as x-shape marker and IR upper limits as plus-shape markers; Béthermin et al., 2020).

in the northeast arm. Regions 8 to 10, on the other hand, sample the area in and between the two galaxies. Emission from regions 8 and 10 arises mostly from C05-NW and C05-SE, respectively, although contamination from disturbed gas in line of sight cannot be excluded.

For the IR luminosity estimation, we fitted a modified black body dust SED with $T_d = 45$ K and $\beta = 1.5$ (assumption comparable with other sources at the same redshift Pavesi et al., 2016; Faisst et al., 2017; Herrera-Camus et al., 2021) to the rest-frame 158 μm continuum and computed the FIR luminosity for the wavelength range 42-122 μm (as Appleton et al., 2013; Peterson et al., 2018). We then applied a mid-infrared correction using the integrated best SED fits from Béthermin et al. (2020). The uncertainties reflect the possible dust temperature range between 30 and 60 K. The global emission (aperture of r = 1.5″) is displayed as a red hexagon in Figure 3.8, and the IR emission is detected in regions 8, 9, and 10 (red circles). For the non-detected regions (0 to 7), the filled-red area corresponds to the upper limits of the mean of the ratios, also assuming $T_d = 45$ K. The global measurement of CRISTAL-05 places it around the upper envelope of the location of local LIRGs. Regions 8, 9, and 10, which comprise the regions in and between C05-NW and C05-SE have a luminosity ratio $\lesssim 1\%$, similar to

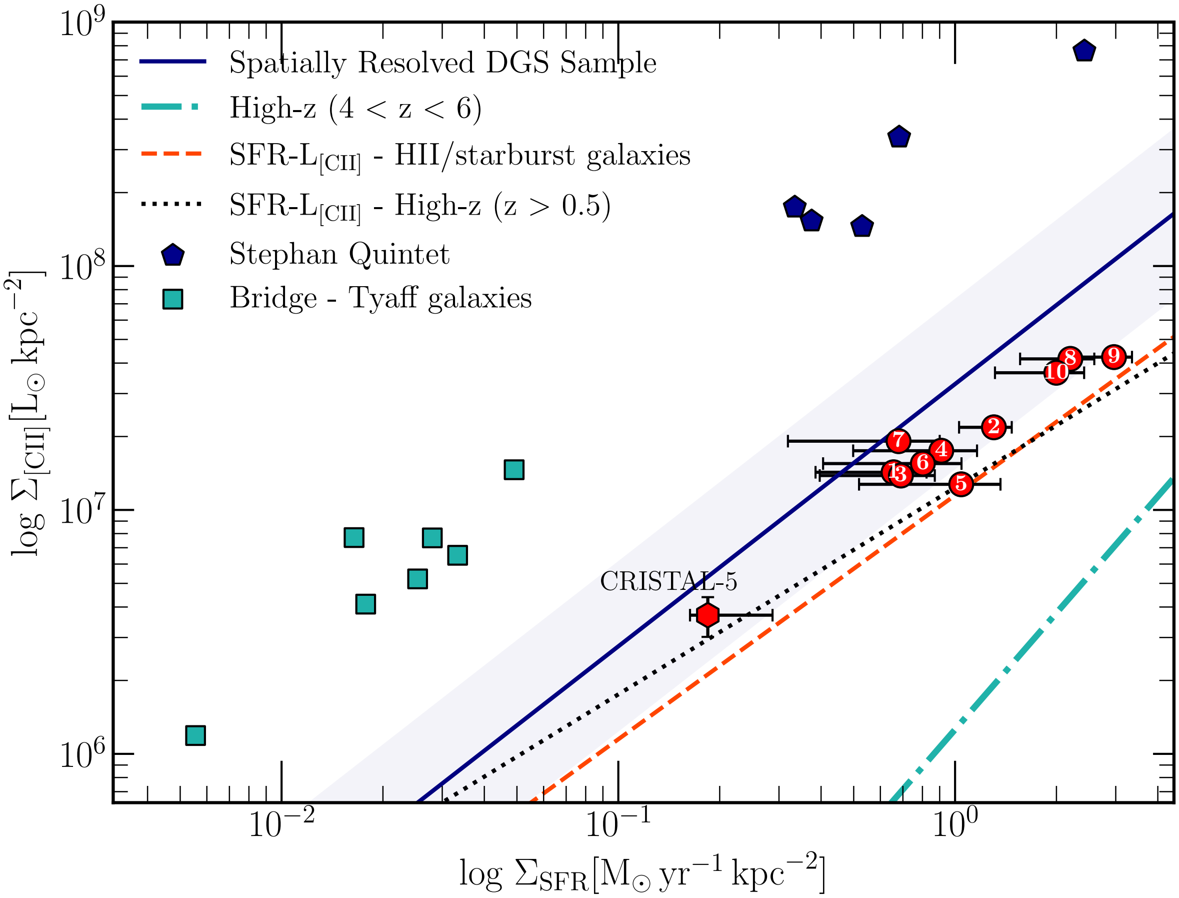

Figure 3.9: Surface [C II] luminosity of CRISTAL-05 and its subregions as a function of the surface star formation rate. The global measurement (aperture of $1.5''$) are represented as red hexagon, and the subregions as red circles, labeled as shown in the left panel Figure 3.8.

normal galaxies. We can see that the upper and lower limits on the L_{FIR} and $L_{[CII]}/L_{FIR}$ values, corresponding to the regions around the two main galaxy components of CRISTAL-05 , are consistent with those found in the overlap/shocked regions of the SQ and Taffy systems.

Although high-z galaxies follow the local $L_{[CII]}$-SFR relation, they show a [C II] deficiency in the $\Sigma_{L_{[CII]}} - \Sigma_{SFR}$ relation compared to local ones, due to their starburst nature, low metallicity or hardness of the UV radiation field (Ferrara et al., 2019). This discrepancy is shown in the dotted-dashed cyan lines in Fig. 3.9, compared to the local relation (solid navy color line). A similar deficiency is seen for local HII galaxies and high-z galaxies (z > 1), as orange dashed and black dotted lines (De Looze et al., 2014), respectively. To make this comparison, we converted their $L_{[CII]} - SFR$ relation to the surface density assuming an area of 7 kpc^2, comparable to the effective radius of the [C II] and UV emission. The SQ Tyaff and SQ shocks regions clearly lie above the local relation. Both the global and subregion emissions are above the discrepancy of Carniani et al. (2018b), indicating a [C II] boost.

Finally, the studies of local galaxies and simulations have also revealed that mergers of galaxies can produce extended gas components without extended stellar distributions produced by collisional processes, which can be produced by ram pressure stripping, shocks, and gas accretion (Sparre et al., 2022). Additionally, Zhang et al. (2020) showed that galaxy interactions can in fact increase some emission line ratios which are consistent with shock produced by mergers.

3.5 CONCLUSIONS

We present sensitive, kpc-scale resolved observations of the [C II] line emission in the massive, main-sequence star-forming galaxy CRISTAL-05 at z $\sim$ 5.54. Based on these [C II] observations from the ALMA large program CRISTAL (plus previous archival and pilot observations), and HST/WFC3 rest-frame UV and JWST MIRI rest-frame optical imaging, we conduct a detailed morphological and kinematic analysis of this system. Previous studies showed this is a low-dust typical star-forming galaxy, with [C II] emission extending beyond the galactic disk, which classifies it as a [C II] halo. We summarize the main findings:

1. **Morpho-kinematical misclassification due to resolution:** The [C II] emission shape is elongated (southeast to the northwest direction), as a result of a double nucleus distribution 2.5 kpc distant. The asymmetric morphology also shows a line-of-sight velocity not smoothly distributed and a homogeneous high peak dispersion velocity of 79 ± 21 km s^{-1}. All these features indicate that CRISTAL-05 is actually a multicomponent system that could not be clearly identified by previous low-resolution observations. The close approach and low-velocity range of -50 – 50 km s^{-1} are typical of interacting with low angular configuration, which requires high-resolution observations to properly perform a morpho-kinematical classification.

2. **[C II] halos:** Contrary to the [C II] emission, the rest UV and near-infrared continuum is compact, slightly elongated to the north-south direction. The $r^{cir}_{[CII]} = 1.6 \pm 0.3$ kpc is

about 4 times greater than the UV effective extension. It extends up to 10 kpc compared to the average UV surface brightness radial profiles. It contributes to about 41% of the [C II] light.

3. **A complex kinematical structure:** CRISTAL-05 is composed of two components and a carbon-rich gas surrounding the central system. We called these components C05-NW and C05-SE . C05-NW especially is more extended and has a rising behavior in the position-velocity diagram. A clump-finding algorithm favors that it is a single clump rather than two merging clumps. The component agrees with a rotating gaseous disk with a low dark matter fraction.
4. **[C II] extended emission due to gas stripping:** We can see that the upper and lower limits on the L_{FIR} and $L_{[CII]}/L_{FIR}$ values of the regions around the C05-NW and C05-SE components of CRISTAL-05 are consistent with those found in the overlap/shocked regions of the local merging systems.

Our results strongly exemplify the necessity to kpc-scale and pc-scales observations to completely dissect the internal dynamical state of galaxies and how it contributes to the the metal enrichment circumgalactic medium of early galaxies. Future observations with JWST and ALMA can help in stating the contribution of outflows in CRISTAL-05 by analyzing the hot ionized outflows.

CHAPTER 4

FINAL REMARKS AND CONCLUSIONS

This Ph.D. thesis presented two detailed studies of the morphology and kinematical properties of two galaxies at the end of the Epoch of Reionization, using recent sensitive high-resolution observations of the [C ɪɪ] line emission obtained with ALMA.

In Chapter 2, we perform a detailed study on the structure and kinematics of COS2987, a Lyman-break galaxy detected in the CANDELS/COSMOS field (Scoville et al., 2007; Koekemoer et al., 2011), and located at z = 6.8076 ± 0.0002. As Smit et al. (2018) identified a tentative gradient in the velocity field of the galaxy, it became a special case to study the dynamical maturity of a galaxy at the moment we may expect a major frequency of clumpy, multi-component systems (Capak et al., 2015). In Chapter 3, we analyze the star-forming galaxy CRISTAL-05, a source well studied by the literature, located at z = 5.54. The galaxy is one of the systems with a spatially extended [C ɪɪ] emission line relative to the UV and dust continuum, commonly referred to as containing a [C ɪɪ] halo. At the time of writing, these two studies represent some of the few detailed resolved investigations of "normal galaxies" at these early epochs, directly tracing their cold ISM's dynamics and internal structure.

SPECIFIC QUESTIONS ADDRESSED

In this work, we address, analyze, and provide insights on the following questions:

WHAT DO EARLY GALAXIES LOOK LIKE?

According to the current galaxy evolution framework, the early stages of galaxy formation are marked by multicomponent structures with irregular velocity fields, possibly by a high rate of galaxy mergers. The galaxy builds up its mass as it is constantly fed by pristine gas from the intergalactic medium through cold mode accretion while it smoothly transitions to become a mature rotating disk galaxy. Owing to the capacity of the two different physical mechanisms (mergers, cold accretion) to shape matter distribution, morphology acts as a primary parameter to identify the evolutionary stage of a galaxy. Furthermore, dynamical processes imprint features in the morphology. Although in the local universe ($z < 1$) the galaxy diversity shapes are well established and thus well correlated to the physical properties of galaxies, little is known about the structures of early galaxies.

Before this thesis, the studies of gaseous properties of $4 < z < 6$ "typical" main-sequence star-forming galaxies using the [C II] line emission were carried out with resolutions of $0.8''$–$1''$. This translates into physical sizes of 4 – 6 kpc, at z = 5 – 7, which is 2 – 3× larger than the effective radius of star-forming galaxies (Fujimoto et al., 2020, $r^{eff}_{[CII]} \sim 2 - 3$ kpc). Therefore, previous observations could only allow for global measurements, not exploring the morphological features of the gas or possible differences in the gas conditions of these galaxies. Our observations reach a final resolution of $0.3''$-$0.4''$, thus changing the morphological scenario of the two galaxies in our sample. Both galaxies, which at first looked like extended single galaxies, became multicomponent systems. COS2987 was first seen as an elongated system, commonly resembling a disk galaxy (Smit et al., 2018). This conclusion was supported by the velocity gradient in the velocity map, typical of rotating systems. Our observations could confirm a velocity gradient in the system's central component, but the galaxy was split into a central component and a northwest arc-shaped component. Conversely, CRISTAL-05 , previously thought to be a dispersion-dominated system, is actually an ongoing merger split into two or three components.

WHAT ARE THE PHYSICAL DRIVERS OF GALAXY GROWTH IN THE EARLY UNIVERSE?

From $z \sim 8$ to 3, we observe a steady increase in cosmic star formation density, as the first galaxies were in a phase of rapid mass assembly (Madau & Dickinson, 2014). This mass growth is believed to be driven by both the cold-mode accretion of pristine gas from the intergalactic medium, which could take place in the form of diffuse gas inflows or minor satellite accretion (minor mergers). However, the relative contribution of this physical process at high redshift remains undetermined due to the difficulty of observing these processes at play at such cosmological distances.

The sensitive ALMA [C ɪɪ] observations presented in this work on the COS2987 system revealed several potential [C ɪɪ] companions, separated by up to $10 - 20$ kpc away from the main galaxy. Given their sizes, fluxes with respect to the main galaxy, and the relatively close distances, it is likely that such satellite candidates will be accreted by the central position well in a few hundred Myrs (Kohandel et al., 2019).

On a similar note, CRISTAL-05 can be dissected into at least two components with a mass ratio of 1:5, consistent with the scenario of a satellite galaxy merging with the central one. Such minor mergers (or satellite accretion) are expected to be more frequent in high-redshift galaxies, according to simulations, aligning with the hierarchical formation of structures. Given the lack of studies that can actually resolve these systems and ultimately classify their kinematical state and the faint nature of these small satellites, our results are among the first to provide observational evidence that satellite accretion is taking place at $z \sim 5$ – 7, playing an important role in the mass assembly of galaxies. These results become more valuable as the minor merger fractions at $5 < z < 6$ are expected to be 2 – 4 lower than the major mergers, as seen in cosmological simulations (Ventou et al., 2019).

ARE ROTATING DISKS DYNAMICALLY HOTTER AT HIGH REDSHIFT? WHAT IS CAUSING THE HIGH TURBULENCE?

Studies of rotating disks at $z < 3$, mostly using CO and Hα, reveal an increase in the intrinsic dispersion velocity towards higher redshifts. This trend keeps increasing at higher redshifts according to the predictions of these systems in cosmological simulations. In recent years, ALMA has been key in expanding our understanding of the kinematical conditions of these rotating disks, mostly exploring the internal motions of the [C ɪɪ] dynamics. Most of these observations explore the gas motions of sub-mm galaxies at $z \sim 4.5$, which benefit from their bright nature and angular sizes. Interestingly, they have challenged our understanding of turbulence at high redshifts since such sources were found to be fast rotators with a high degree of stability, thus deviating from the cosmic evolution of the dispersion and rotation-to-dispersion ratios (Rizzo et al., 2020; Lelli et al., 2021).

The advent of sensitive ALMA [C II] observations of galaxies at $z > 4$ is enabling us to start exploring these scenarios for the more typical (fainter and lower mass than sub-mm galaxies) main-sequence star-forming galaxies like COS2987 and CRISTAL-05 . In our study, we found that the [C II] emission from the central source in the COS2987 system can be modeled as a rotating disk, with an intrinsic dispersion velocity of < 30 km s^{-1} , being dynamically colder than what is expected for rotating disks at z $\sim$ 7 from semi-analytic models (Wisnioski et al., 2015).

A similar result is seen in C05-NW at $z \sim 5.5$, whose intrinsic dispersion velocity of 33 $^{+2}_{-3}$ km s^{-1} , also deviates from the expected turbulence at z = 5.54. As previously discussed, compact mergers or galaxies with a strong outflow episode may mimic the velocity field of rotating disks. When considering a disk, such deviations from the expected velocity dispersion trend at high redshift could be caused by limitations in retrieving the kinematical modeling with an insufficient signal-to-noise ratio. For instance, the tilted-ring modeling requires a high signal-to-noise ratio per ring; otherwise, the intrinsic velocity dispersion may be underestimated (Lee, private communication).

If the rotating disk nature of this galaxy is confirmed, we have at hand one of the first observed cases of a mature dynamical typical galaxy in the first billion years of the universe. Even though these galaxies have low dispersions as expected by observations and models, the presence of surrounding satellite galaxies indicates that these galaxies may go through short periods of stability and satellite accretion is an important mechanism in place to contribute to the higher turbulence in early disk galaxies.

WHAT IS PRODUCING THE [C II] EMISSION IN HIGH-Z GALAXIES? WHAT IS THE ORIGIN OF THE [C II] HALOS?

It is still a matter of debate about the actual gas conditions of high-redshift galaxies. [C II] is a major coolant line of the ISM; hence, it connects directly with the energy released by massive stars during star formation activity (De Looze et al., 2014; Herrera-Camus et al., 2015b). Although high-redshift galaxies follow the $L_{[CII]}$–SFR trend of local galaxies, the [C II] surface brightness of these systems is systematically lower than the local relation (Carniani et al., 2018b). Recent analytical models of the ionization/PDR radiation field conclude that these underluminous systems can result from a combination of starburst nature, low metallicity, and low gas density (Ferrara et al., 2019). In contrast, several sources at $5 < z < 7$ show a more extended emission distribution compared to the UV and dust sizes, which indicates that different heating sources rather than star formation might be in place (Fujimoto et al., 2020). Among the several scenarios, outflows caused by intense stellar feedback activity are the preferable explanation for this phenomenon (Ginolfi et al., 2020c).

In this thesis, we did not detect [C II] extended emission in COS2987 based on our multi-wavelength morphological analysis. We conclude that the main bulk of [C II] emission is generated by photoelectric heating in PDRs. On the contrary, we found extended [C II] emission in CRISTAL-05 . This stark difference suggests that extended [C II] emission (or [C II] halos) is not ubiquitous in high-redshift galaxies. While it could be argued that galaxies at redshifts above 7 do not host such [C II] halos, as possibly it would be too early for the extended emission to form, the recent detection of such [C II] halos in a low-mass star-forming galaxy at $z \sim 7$ contradicts this hypothesis (Akins et al., 2022).

Furthermore, the high-resolution observations of CRISTAL-05 revealed that the system is actually the merger of two galaxies, plus a possible additional diffuse component. In this case, our results suggest that the extended [C II] emission results from kinematic energy dissipation produced by this merger. The upper and lower limits of the L_{FIR} and $L_{[CII]}/L_{FIR}$ measurements in the regions around the two main galaxy components of CRISTAL-05 are consistent with those found in the overlap/shocked regions of the SQ and Taffy systems in the local universe (Appleton et al., 2013; Peterson et al., 2018). As such, mergers might not only contribute to galaxy growth but also chemically enrich the circumgalactic medium.

FUTURE STEPS

New results lead to new questions. We summarize the next steps we want to achieve to expand our knowledge in the gaseous components of the high-redshift universe:

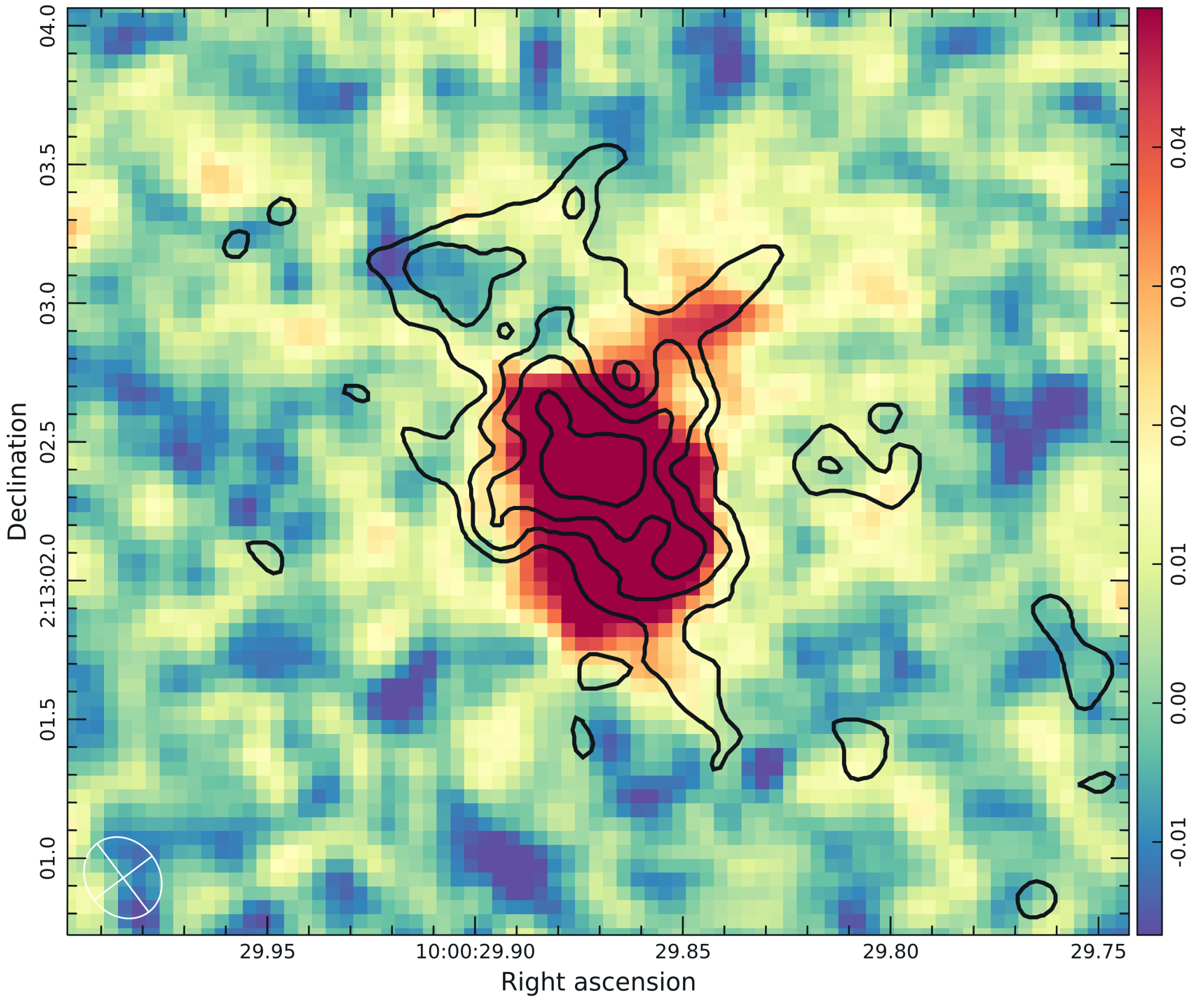

Figure 4.1: Comparison of the [OIII] excess and new [C ɪɪ] moment-0 map. The background image results from the subtraction of the JWST/NIRCAM F356W by averaging the F227W and F444W. The [C ɪɪ] moment-0 map is overlaid as 2-, 3-, 4- and 5-σ significance level.

WITNESSING THE ASSEMBLY OF COS2987

The immediate following steps are already in progress. We obtained new ALMA (0.2-0.3″) observation of the [C ɪɪ] line and continuum of COS2987 (ID 2021.1.01159.5, PI: Nascimento), doubling the sensitivity of the previous observation analyzed in this thesis. Combining the new deeper data with prior ones that cover the short spacing in the uv-plane, our main three goals are (i) to confirm the candidate [C ɪɪ] satellites (namely called N1, N2, W1, and W2 in Chapter 2) of the galaxy's environment, (ii) improve the parametrization of the dynamics as we improved the signal-to-noise and (iii) analyze the connection with the [O ɪɪɪ] emission. In Fig. 4.1 we show the preliminary results. The [C ɪɪ] moment-0 map is shown in black contour at significance levels of 2-, 3-, 4-, and 5-σ. In the background, we show the residuals of the subtraction of the JWST NIRCAM broadband filter F356W, which at z = 6.8076 traces the stellar continuum + contribution of the [O III] $_{4959}$, [O III] $_{5007}$ and H_β line emissions, by the line-free average image of F227W and F444W bands. Therefore, it represents the emission excess caused by mainly the two [O III] line emissions, which are a tracer of ionized gas. The [C II] emission now exhibits faint, widespread emission that was not detectable in shallower imaging, and it is closely associated with the [O III] emission. Notably, in the northwestern region of the galaxy, which coincides with the previously identified north-arm source of [C II] emission (N2 in Chapter 2), we observe an elongated emission featuring both [C II] and [O III] . This [O III] emission excess implies the presence of outflowing activity.

RESOLVING SUB-KPC SCALES OF THE [C II] OF CRISTAL-05 AND COS2987

We have shown that resolving typical galaxies in kpc-scales is crucial to accessing the internal structure of the gaseous components of early galaxies. The next step is to observe the sources in a more extended ALMA configuration, reaching angular resolutions of 0.1″ (∼ 600 pc, at z = 5.5 – 7). This would be one of the first times we will be accessing observations at pc-scales of this kind of star-forming galaxies at these epochs. Firstly, we will ultimately rule out the scenario that the velocity gradient in the moment-1 map is caused by two galaxies, distant less than 2 kpc for COS297 and C05-NW . Secondly, if we confirm the rotating nature of the galaxies, we can perform a better kinematical fitting, as the points in the current rotation curve are not fully independent.

LOOKING FOR IONIZED OUTFLOWS

We still need to explore if there is any contribution from outflows to the extended emission of CRISTAL-05 . Upcoming JWST GO2 NIRSpec observations, which will be publicly available, will enable us to explore such a scenario based on the optical [O III] $_{5007}$ line on this target. For COS2987, recent observations reported by (Witstok et al., 2022) show the detection of the [O III] $_{88\mu\mathrm{m}}$ line emission although at moderate significance, not allowing to check for possible broad line components that would point to outflow activity. Given the recent detection of such outflows in a similar system (Akins et al., 2022), it becomes a natural step to request deeper and possibly higher resolution ALMA observations of the [O III] $_{88\mu m}$ line to check for outflows in COS2987.

In the last few years, we have witnessed a big revolution in the characterization of early galaxies, especially after the launch and capabilities of JWST. In this thesis, we presented cutting-edge observations of the cold ISM gas in two galaxies at $z > 4$, representing valuable results and insights to understand the formation and growth of early galaxies. Despite the important advances and progress, we are still in the early steps of detecting and characterizing the origin and composition of such cold gas on a kpc scale. In the coming years, the CRISTAL survey will provide valuable insights into the high-precision exploration of the early universe.

BIBLIOGRAPHY

Akins H. B., et al., 2022, , 934, 64

Appleton P. N., et al., 2013, , 777, 66

Arata S., Yajima H., Nagamine K., Abe M., Khochfar S., 2020, , 498, 5541

Baldry I. K., Glazebrook K., Brinkmann J., Ivezić Ž., Lupton R. H., Nichol R. C., Szalay A. S., 2004, , 600, 681

Barisic I., et al., 2017, , 845, 41

Barnes J. E., Hernquist L. E., 1991, , 370, L65

Berry D., 2015, Astronomy and Computing, 10, 22

Béthermin M., et al., 2014, , 567, A103

Béthermin M., et al., 2020, , 643, A2

Bianchi S., et al., 2018, , 620, A112

Bolatto A. D., Wolfire M., Leroy A. K., 2013, , 51, 207

Bournaud F., Elmegreen B. G., Teyssier R., Block D. L., Puerari I., 2010, , 409, 1088

Bournaud F., et al., 2011, , 730, 4

Bouwens R. J., et al., 2014, , 793, 115

Bouwens R. J., et al., 2016, , 833, 72

Bouwens R., et al., 2020, , 902, 112

Bouwens R. J., et al., 2021, arXiv e-prints, p. arXiv:2106.13719

Bowler R. A. A., McLure R. J., Dunlop J. S., McLeod D. J., Stanway E. R., Eldridge J. J., Jarvis M. J., 2017, , 469, 448

Brinchmann J., Charlot S., White S. D. M., Tremonti C., Kauffmann G., Heckman T., Brinkmann J., 2004, , 351, 1151

Burkert A., et al., 2010, , 725, 2324

Capak P. L., et al., 2015, , 522, 455

Carilli C. L., Walter F., 2013, , 51, 105

Carniani S., et al., 2018a, , 478, 1170

Carniani S., et al., 2018b, , 478, 1170

Carniani S., Maiolino R., Smit R., Amorín R., 2018c, , 854, L7

Carniani S., et al., 2020, , 499, 5136

Cicone C., et al., 2015, , 574, A14

Clark P. C., Glover S. C. O., Ragan S. E., Duarte-Cabral A., 2019, , 486, 4622

Conselice C. J., Arnold J., 2009, , 397, 208

Cormier D., et al., 2015, , 578, A53

Czekala I., et al., 2021, , 257, 2

Daddi E., et al., 2021, , 649, A78

Daddi E., et al., 2022, , 926, L21

Dayal P., Ferrara A., 2018, , 780, 1

Dayal P., et al., 2020, , 495, 3065

De Looze I., Baes M., Bendo G. J., Cortese L., Fritz J., 2011, , 416, 2712

De Looze I., et al., 2014, , 568, A62

De Lucia G., Springel V., White S. D. M., Croton D., Kauffmann G., 2006, Monthly Notices of the Royal Astronomical Society, 366, 499

Dekel A., et al., 2009, , 457, 451

Dessauges-Zavadsky M., et al., 2020, , 643, A5

Di Teodoro E. M., Fraternali F., 2015, , 451, 3021

Díaz-Santos T., et al., 2013, , 774, 68

Draine B. T., 1978, , 36, 595

Draine B. T., 2011, Physics of the Interstellar and Intergalactic Medium

Dressler A., 1980, , 236, 351

Duncan K., et al., 2019, , 876, 110

Dunlop J. S., et al., 2013, , 432, 3520

Dunlop J. S., et al., 2021, PRIMER: Public Release IMaging for Extragalactic Research, JWST Proposal. Cycle 1, ID. #1837

Dutton A. A., Macciò A. V., 2014, , 441, 3359

Eales S. A., Wynn-Williams C. G., Duncan W. D., 1989, , 339, 859

Elmegreen B. G., Elmegreen D. M., 2005, , 627, 632

Emonts B. H. C., et al., 2023, Science, 379, 1323

Faber S. M., et al., 2007, , 665, 265

Faisst A. L., et al., 2017, , 847, 21

Faisst A. L., et al., 2020, , 247, 61

Ferrara A., Vallini L., Pallottini A., Gallerani S., Carniani S., Kohandel M., Decataldo D., Behrens C., 2019, , 489, 1

Ferreira L., et al., 2022, , 938, L2

Förster Schreiber N. M., Wuyts S., 2020, , 58, 661

Fraternali F., Karim A., Magnelli B., Gómez-Guijarro C., Jiménez-Andrade E. F., Posses A. C., 2021, , 647, A194

Fudamoto Y., et al., 2020, , 643, A4

Fujimoto S., et al., 2019, , 887, 107

Fujimoto S., et al., 2020, , 900, 1

Gaia Collaboration et al., 2018, , 616, A1

Gallerani S., Pallottini A., Feruglio C., Ferrara A., Maiolino R., Vallini L., Riechers D. A., Pavesi R., 2018, , 473, 1909

Galliano F., Galametz M., Jones A. P., 2018, , 56, 673

Genzel R., et al., 2015, , 800, 20

Genzel R., et al., 2020, , 902, 98

Ginolfi M., et al., 2020a, , 633, A90

Ginolfi M., et al., 2020b, , 643, A7

Ginolfi M., et al., 2020c, , 643, A7

Girard M., et al., 2018, , 613, A72

Goldsmith P. F., Langer W. D., Pineda J. L., Velusamy T., 2012, , 203, 13

Grazian A., et al., 2015, , 575, A96

Gullberg B., et al., 2015, , 449, 2883

Guo Y., et al., 2023, , 945, L10

Harikane Y., et al., 2018, , 859, 84

Harrison C. M., 2017, Nature Astronomy, 1, 0165

Hayward C. C., Hopkins P. F., 2016, Monthly Notices of the Royal Astronomical Society, 465, 1682

Heckman T. M., Lehnert M. D., Strickland D. K., Armus L., 2000, , 129, 493

Heintz K. E., Watson D., Oesch P., Narayanan D., Madden S. C., 2021, arXiv e-prints, p. arXiv:2108.13442

Herrera-Camus R., et al., 2015a, , 800, 1

Herrera-Camus R., et al., 2015b, , 800, 1

Herrera-Camus R., et al., 2018a, , 861, 95

Herrera-Camus R., et al., 2018b, , 861, 95

Herrera-Camus R., et al., 2021, , 649, A31

Hopkins P. F., Somerville R. S., Hernquist L., Cox T. J., Robertson B., Li Y., 2006, , 652, 864

Hopkins P. F., Hernquist L., Cox T. J., Kereš D., 2008, , 175, 356

Hoyle F., 1949, , 109, 365

Ilbert O., et al., 2013, , 556, A55

Inoue A. K., et al., 2016, Science, 352, 1559

Jones G. C., et al., 2021, , 507, 3540

Jorsater S., van Moorsel G. A., 1995, , 110, 2037

Katz H., et al., 2019, , 487, 5902

Kennicutt R. C., Evans N. J., 2012, , 50, 531

Kereš D., Katz N., Weinberg D. H., Davé R., 2005a, , 363, 2

Kereš D., Katz N., Weinberg D. H., Davé R., 2005b, , 363, 2

King A., Pounds K., 2015, , 53, 115

Klaas U., Haas M., Heinrichsen I., Schulz B., 1997, , 325, L21

Koekemoer A. M., et al., 2011, , 197, 36

Kohandel M., Pallottini A., Ferrara A., Zanella A., Behrens C., Carniani S., Gallerani S., Vallini L., 2019, , 487, 3007

Kohandel M., Pallottini A., Ferrara A., Carniani S., Gallerani S., Vallini L., Zanella A., Behrens C., 2020, , 499, 1250

Kroupa P., Weidner C., 2003, , 598, 1076

Lagache G., Cousin M., Chatzikos M., 2018, , 609, A130

Laigle C., et al., 2016, , 224, 24

Lambas, D. G. Alonso, S. Mesa, V. O´Mill, A. L. 2012, A&A, 539, A45

Lambert T. S., et al., 2023, , 518, 3183

Laporte N., Nakajima K., Ellis R. S., Zitrin A., Stark D. P., Mainali R., Roberts-Borsani G. W., 2017, , 851, 40

Le Fèvre O., et al., 2020, , 643, A1

Lelli F., Di Teodoro E. M., Fraternali F., Man A. W. S., Zhang Z.-Y., De Breuck C., Davis T. A., Maiolino R., 2021, Science, 371, 713

Longair M. S., 2008, Galaxy Formation

Lupi A., Bovino S., 2020, , 492, 2818

Mac Low M.-M., Klessen R. S., 2004, Reviews of Modern Physics, 76, 125

Madau P., Dickinson M., 2014, , 52, 415

Maiolino R., et al., 2012, , 425, L66

Malhotra S., et al., 2001, , 561, 766

Matthee J., et al., 2017, , 851, 145

Matthee J., et al., 2019, , 881, 124

McMullin J. P., Waters B., Schiebel D., Young W., Golap K., 2007, in Shaw R. A., Hill F., Bell D. J., eds, Astronomical Society of the Pacific Conference Series Vol. 376, Astronomical Data Analysis Software and Systems XVI. p. 127

Meyer R. A., et al., 2022, , 927, 152

Naidu R. P., Tacchella S., Mason C. A., Bose S., Oesch P. A., Conroy C., 2020, , 892, 109

Navarro-Carrera R., Rinaldi P., Caputi K. I., Iani E., Kokorev V., van Mierlo S. E., 2023, arXiv e-prints, p. arXiv:2305.16141

Navarro J. F., Frenk C. S., White S. D. M., 1996, , 462, 563

Nayyeri H., et al., 2017, , 228, 7

Neeleman M., Prochaska J. X., Kanekar N., Rafelski M., 2020, , 581, 269

Neeleman M., et al., 2021, , 911, 141

Nelson D., et al., 2019, , 490, 3234

Omont A., 2007, Reports on Progress in Physics, 70, 1099

Pallottini A., Ferrara A., Gallerani S., Vallini L., Maiolino R., Salvadori S., 2017, , 465, 2540

Pallottini A., et al., 2019, , 487, 1689

Pallottini A., et al., 2022, , 513, 5621

Papadopoulos P. P., Greve T. R., 2004, , 615, L29

Pavesi R., et al., 2016, , 832, 151

Peterson B. W., et al., 2018, , 855, 141

Pillepich A., et al., 2019, , 490, 3196

Pizzati E., Ferrara A., Pallottini A., Gallerani S., Vallini L., Decataldo D., Fujimoto S., 2020, , 495, 160

Pizzati E., Ferrara A., Pallottini A., Sommovigo L., Kohandel M., Carniani S., 2023, , 519, 4608

Poggianti B. M., De Lucia G., Varela J., Aragon-Salamanca A., Finn R., Desai V., von der Linden A., White S. D. M., 2010, , 405, 995

Posses A. C., et al., 2023, , 669, A46

Postman M., et al., 2005, , 623, 721

Price S. H., et al., 2021, , 922, 143

Rauch M., Becker G. D., Haehnelt M. G., Gauthier J.-R., Ravindranath S., Sargent W. L. W., 2011, , 418, 1115

Rizzo F., Vegetti S., Powell D., Fraternali F., McKean J. P., Stacey H. R., White S. D. M., 2020, , 584, 201

Rizzo F., Vegetti S., Fraternali F., Stacey H. R., Powell D., 2021, , 507, 3952

Rizzo F., Kohandel M., Pallottini A., Zanella A., Ferrara A., Vallini L., Toft S., 2022, , 667, A5

Robertson B. E., Ellis R. S., Furlanetto S. R., Dunlop J. S., 2015, The Astrophysical Journal, 802, L19

Romano M., et al., 2021, , 653, A111

Ryden B., 2003, Introduction to cosmology

Sánchez Almeida J., Elmegreen B. G., Muñoz-Tuñón C., Elmegreen D. M., 2014, , 22, 71

Sanders D. B., Mirabel I. F., 1996, , 34, 749

Schaerer D., et al., 2020, , 643, A3

Schreiber C., et al., 2015, , 575, A74

Scoville N., et al., 2007, , 172, 38

Sérsic J. L., 1963, Boletin de la Asociacion Argentina de Astronomia La Plata Argentina, 6, 41

Sharma G., Salucci P., Harrison C. M., van de Ven G., Lapi A., 2021, , 503, 1753

Shibuya T., Miura N., Iwadate K., Fujimoto S., Harikane Y., Toba Y., Umayahara T., Ito Y., 2022, , 74, 73

Silk J., 2013, , 772, 112

Skibba R. A., et al., 2011, , 738, 89

Smit R., et al., 2015, , 801, 122

Smit R., et al., 2018, , 553, 178

Solomon P. M., Downes D., Radford S. J. E., 1992, , 398, L29

Somerville R. S., Davé R., 2015, , 53, 51

Song M., et al., 2016, , 825, 5

Sparre M., Whittingham J., Damle M., Hani M. H., Richter P., Ellison S. L., Pfrommer C., Vogelsberger M., 2022, , 509, 2720

Speagle J. S., Steinhardt C. L., Capak P. L., Silverman J. D., 2014, , 214, 15

Spilker J. S., et al., 2015, , 811, 124

Spilker J. S., et al., 2022, , 929, L3

Stacey G. J., Geis N., Genzel R., Lugten J. B., Poglitsch A., Sternberg A., Townes C. H., 1991, , 373, 423

Stacey G. J., Hailey-Dunsheath S., Ferkinhoff C., Nikola T., Parshley S. C., Benford D. J., Staguhn J. G., Fiolet N., 2010, , 724, 957

Tacconi L. J., et al., 2010, , 463, 781

Tacconi L. J., et al., 2018, , 853, 179

Tojeiro R., et al., 2013, , 432, 359

Toomre A., 1964, , 139, 1217

Tumlinson J., Peeples M. S., Werk J. K., 2017, , 55, 389

Übler H., et al., 2017, , 842, 121

Übler H., et al., 2019, , 880, 48

Vallini L., Gallerani S., Ferrara A., Pallottini A., Yue B., 2015, , 813, 36

Vallini L., Ferrara A., Pallottini A., Carniani S., Gallerani S., 2020, , 495, L22

Vallini L., Ferrara A., Pallottini A., Carniani S., Gallerani S., 2021, , 505, 5543

Ventou E., et al., 2019, , 631, A87

Willott C. J., Carilli C. L., Wagg J., Wang R., 2015, , 807, 180

Wisnioski E., et al., 2015, , 799, 209

Wisnioski E., et al., 2019, , 886, 124

Witstok J., et al., 2022, , 515, 1751

Wolfire M. G., McKee C. F., Hollenbach D., Tielens A. G. G. M., 2003, , 587, 278

Yajima H., Nagamine K., Zhu Q., Khochfar S., Dalla Vecchia C., 2017, , 846, 30

Zanella A., et al., 2018, , 481, 1976

Zaroubi S., 2013, in Wiklind T., Mobasher B., Bromm V., eds, Astrophysics and Space Science Library Vol. 396, The First Galaxies. p. 45 (`arXiv:1206.0267`), doi:10.1007/978-3-642-32362-1_2

Zhang H., Fang T., Zaritsky D., Behroozi P., Werk J., Yang X., 2020, , 893, L3 de Ugarte Postigo A., et al., 2012, , 538, A44

van de Voort F., Schaye J., Booth C. M., Haas M. R., Dalla Vecchia C., 2011, , 414, 2458

van der Tak F. F. S., et al., 2018, , 35, e002

APPENDIX A

COS2987

A.1 DATA PRODUCTS

A.1.1 [C II] MOMENT-0 MAPS FOR THE AVAILABLE OBSERVATIONS

In Figure A.1, we display the [C II] moment-0 maps for the available observations: low-resolution data from Smit et al. (2018) (left panel; PI: Smit, ALMA ID: 2015.1.01111.S), high-resolution data obtained in Cycle 6 (central panel; PI: Aravena, PID: 2018.1.01359.S) and the combination of both data sets (right panel). The cubes were obtained using the *tclean* task of CASA software using natural weighting to preserve sensitivity. The maps represent the collapsed line cube, averaged over a 150 km s^{-1} centered at the [C II] line frequency.

A.1.2 DATA CUBE

In Figure A.2, we provide the $2'' \times 2''$ [C II] channel map postage stamps in velocity steps of 30 km s^{-1}, within the velocity range of [-180,180] km s^{-1}.

A.1.3 GALAXY WIDE-FIELD

In the left panel of Figure A.3, we display the F160W-band image overlapped by the [C II] moment-0 map in contours at significance levels of 2-, 3-, 4-, 5-, and 6-σ. In Section 2.3.1 we searched for a UV counterpart for the candidate [C II] emitter W1 and W2, and we just found a rest-frame UV emitter which is located east from W1. The centroid distance of $0.95''$ for the central source C and W1 translates into a projected physical separation of 5 kpc. It was previously

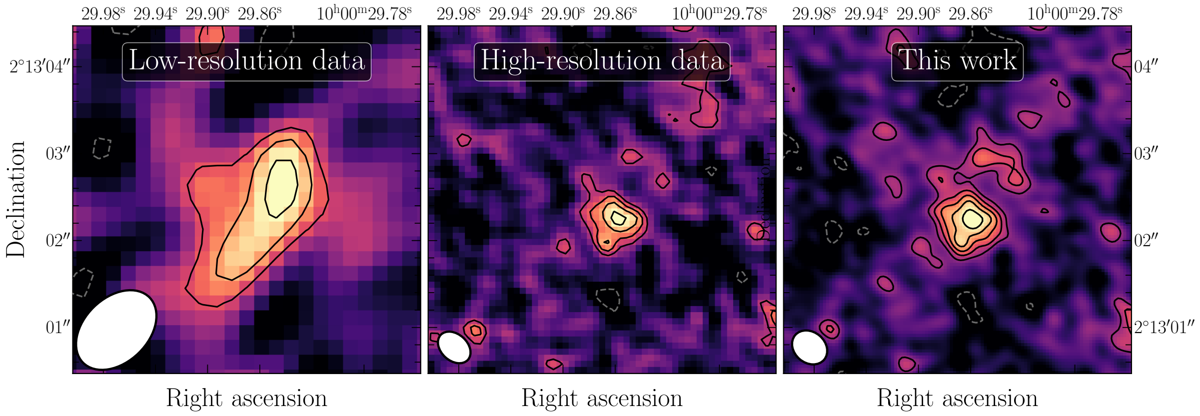

Figure A.1: Comparison of the 5″ ×5″ zoom-in [C II] moment-0 maps for the available observations of COS2987. The left, central, and right panels correspond to the observation of Smit et al. (2018), our observation, and the combination of both, respectively. The overlaid black contours show the 2, 4, 6, and 8-σ levels, and the dashed dark gray contours show the -2σ level of each [C II] map. The white ellipse in the bottom right corner represents the beam size.

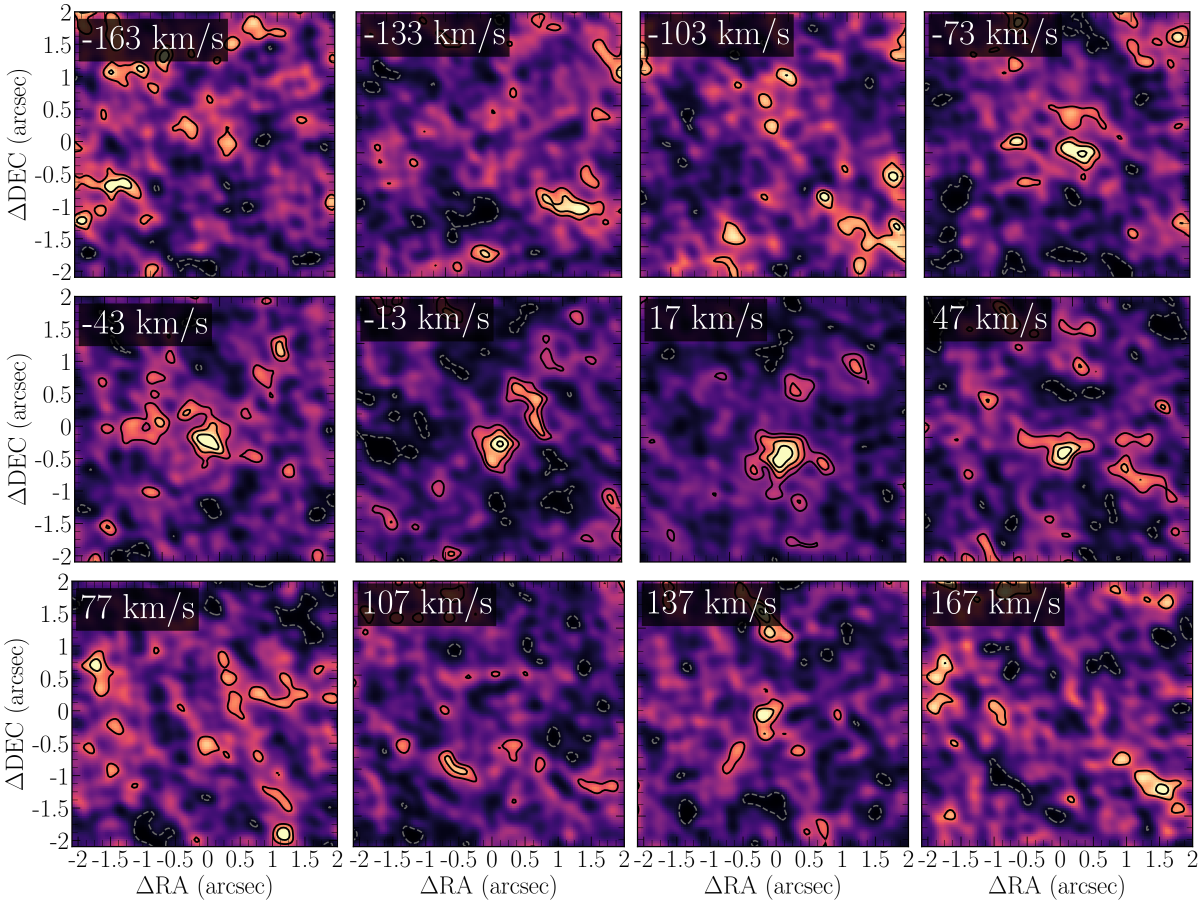

Figure A.2: Channel maps of the cube within a velocity range of [-180,180] km s^{-1} (in bins of 30 km s^{-1}), centered at the observed [C II] frequency. The overlaid black contours show the 2-, 4-, 6-, and 8-σ levels of the maps, and the dashed dark gray contours show the -2σ level of the [C II] maps. The central velocity of each channel is placed in the left corner of each image.

identified as a galaxy with photometric redshift of 1.73 by Laigle et al. (2016). If the W2 candidate emitter was located at this redshift, the tentative emission would be explained by some emission at rest-frame frequency of 664.35 GHz. The closest bright possible emission would be the CO(6-5) at 691.47 GHz. Therefore, we ruled out this possibility.

In the right panel of Figure A.3, we display the wide-field continuum image centered at the COS2987 galaxy. The image excludes any channel within the velocity range [-250,250] km s^{-1} centered at the line. We zoom in the region represented by the white dashed line in the bottom left panel. The black solid lines correspond to the continuum significance levels from 2- to 7-σ at steps of 1-σ and the white solid lines correspond to the [C II] emission significance level of 2-, 3-, 4-, 5-, 6-σ. We reported the continuum detection for the galaxy COSMOS 4104 (α, δ) =(10:00:29.6668, +02:13:14.591) at the photometric redshift 2.25 (Nayyeri et al., 2017).

A.2 SOURCES PROPERTIES

In Section 2.3.1, we describe the properties of four [C II] emitters: the central source (C), north-east emission (N1), north-west arm (N2), west emission (W1), south-west emission (W2). The latter two are deemed as candidate [C II] emitters. They are shown in Figure 2.1 (central panel) and their properties are listed in Table A.1. The properties are taken from a region that contains the emission of each source. The central coordinates (right ascension and declination) represent the centroids of each emission. The [C II] luminosity is obtained following (Solomon et al., 1992), using:

$$L_{[CII]} = 1.04 \times 10^{-3}\, S_{[CII]} \Delta v\, D_L^2\, \nu_{obs}, \tag{A.1}$$

where $L_{[CII]}$ is measured in $L_{\odot}$, the velocity integrated flux, $S_{[CII]}\Delta v$, in Jy km s^{-1}, the observed frequency, ν_{obs}, in GHz, and the luminosity distance, D_L, in Mpc.

A.3 TARGET EXTENSION

We employed a Monte Carlo Markov Chain (MCMC) technique to fit a two-dimensional Sérsic profile to the [C II] and UV surface brightness distribution. We use the *Sersic2D* task from the

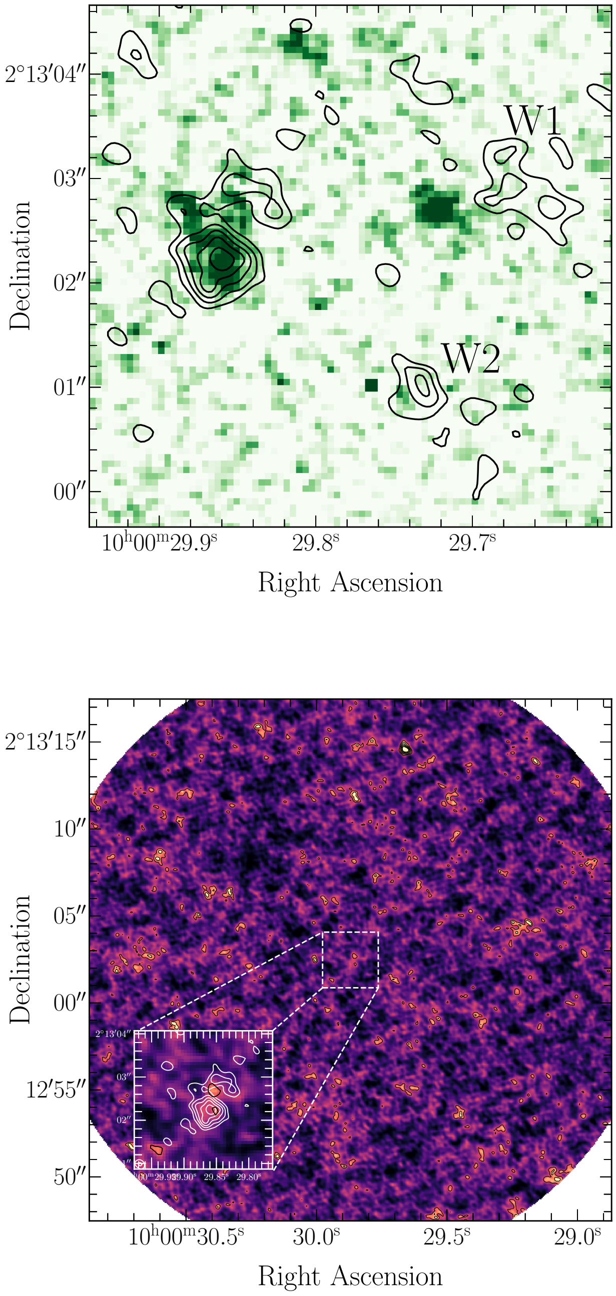

Figure A.3: Wide-field rest-frame UV and continuum maps of COS2987 and surrounding regions. **(a) Left panel:** HST F160W-band image in a 6″ × 6″ region containing the central source and the candidate [C II] emitters (see Section 2.3.1). The [C II] moment-0 map is overlaid in black contours represented by the significance levels of 2-, 3-, 4-, 5-, 6-σ. **(b) Right panel:** Continuum map of the COS2987 field. The black lines correspond to the continuum significance levels from 2- to 7-σ at steps of 1-σ. In the bottom left panel within the main panel, we zoom in the central source in a 4″ ×4″ region. The overlaid white lines represent the [C II] moment-0 map for the significance levels from 2- to 6-σ, at steps of 1-σ.

astropy package in python to generate the surface brightness map, which is described by the following parameters: amplitude (a; surface brightness at the effective radius), ellipticity (e), Sérsic index (n), effective half-light radius ($r_{\rm eff}$), rotation angle (θ), and central pixel position (x_0 and y_0). For the rest-frame UV and [C II] emission, we follow two approaches: (i) setting all the parameters as free; and (ii) fixing the Sérsic index $n = 1$, for a fair comparison with previous studies (Fujimoto et al., 2020). We excluded the pixels within the region corresponding to the north-east foreground galaxy (located a z = 2.099; Laporte et al., 2017) and the north-west arm. In the case of ALMA maps, we assume a constant Gaussian noise across the whole image. In the case of HST images, we consider a background Gaussian noise and Poisson noise from the emission added in quadrature. We ran the MCMC routine with 100 walkers for 5000 interactions. In Figures A.4, A.5, A.6, and A.7 we show the posterior distributions of each parameter.

A.4 ^{3D}BAROLO PRODUCTS

In Table A.2 we provide the best-fit values for each ring for the free parameters: rotational velocity, dispersion velocity, inclination, position angle and system velocity. In Figure A.8, we display the residuals (weighted by the moment-0 map) for the different inclination for the kinematics modeling.

Property	N1	N2	W1	W2
RA	10:00:29.8841	10:00:29.8429	10:00:29.6692	10:00:29.7354
DEC	+02:13:02.671	+02:13:02.871	+2:13:02.832	+02:13:00.958
S/N	2.2 σ	4.1σ	5.2σ	3.6σ
[C II] line flux (Jy km s^{-1})	0.02± 0.01	0.07 ± 0.02	0.10 ± 0.03	0.06 ± 0.02
$L_{[CII]}$ (10^8 $L_\odot$)	0.2 ± 0.1	0.8 ± 0.2	1.1 ± 0.3	0.7 ± 0.2

Table A.1: [C II] properties of the identified clump candidates around COS2987. (central panel).

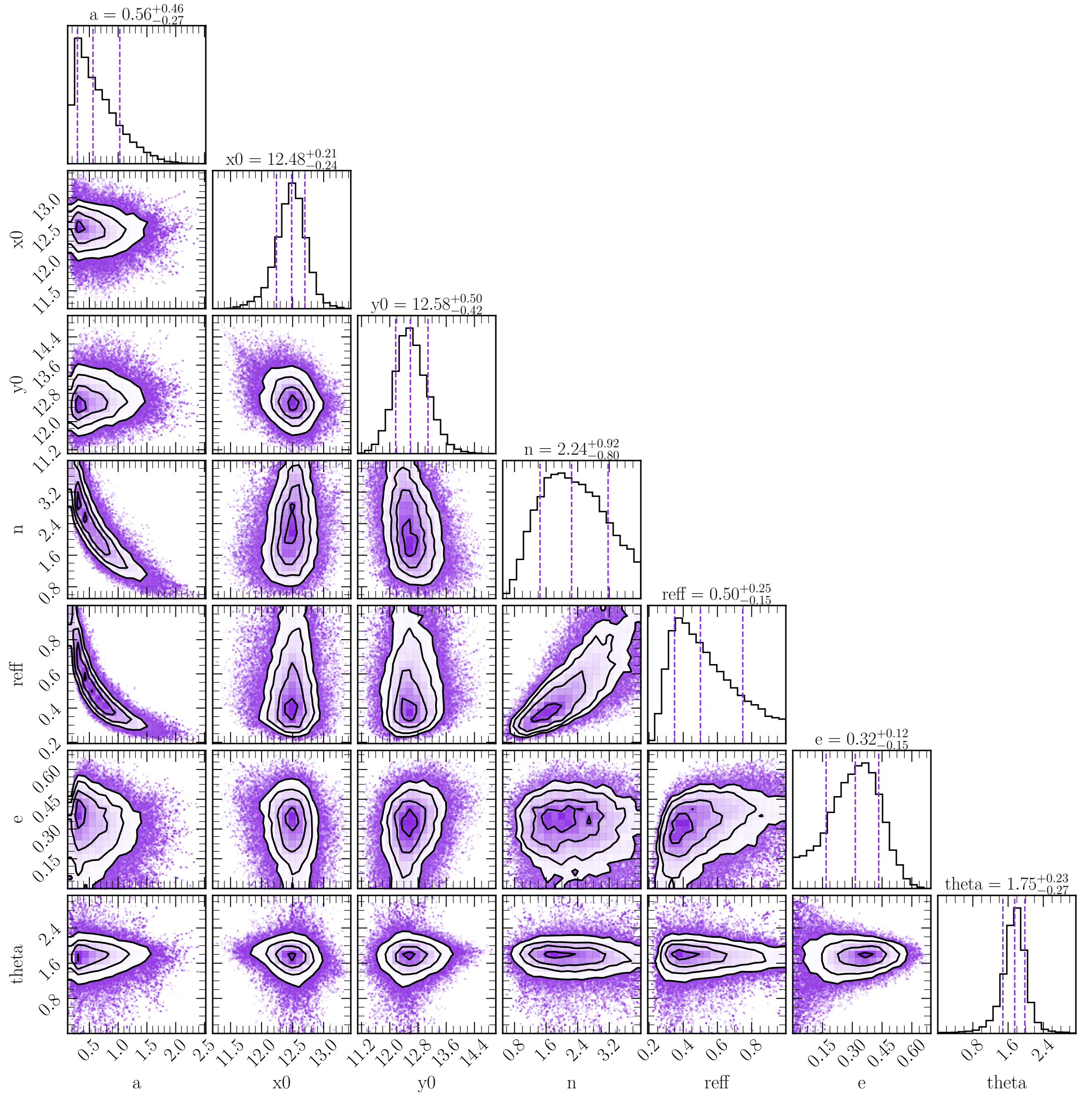

Figure A.4: Posterior distributions of parameters of the two-dimensional UV surface brightness, setting the Sérsic index as a free parameter. The Sérsic profile model also includes the surface brightness at the effective radius (a), the central pixel position (x_0 and y_0), the effective half-light radius (r_{eff}), ellipticity (e), and the rotation angle (theta). Black contours in the 2D posterior distributions and the dashed purple lines in the histograms correspond to 16%, 50%, and 84% confidence regions.

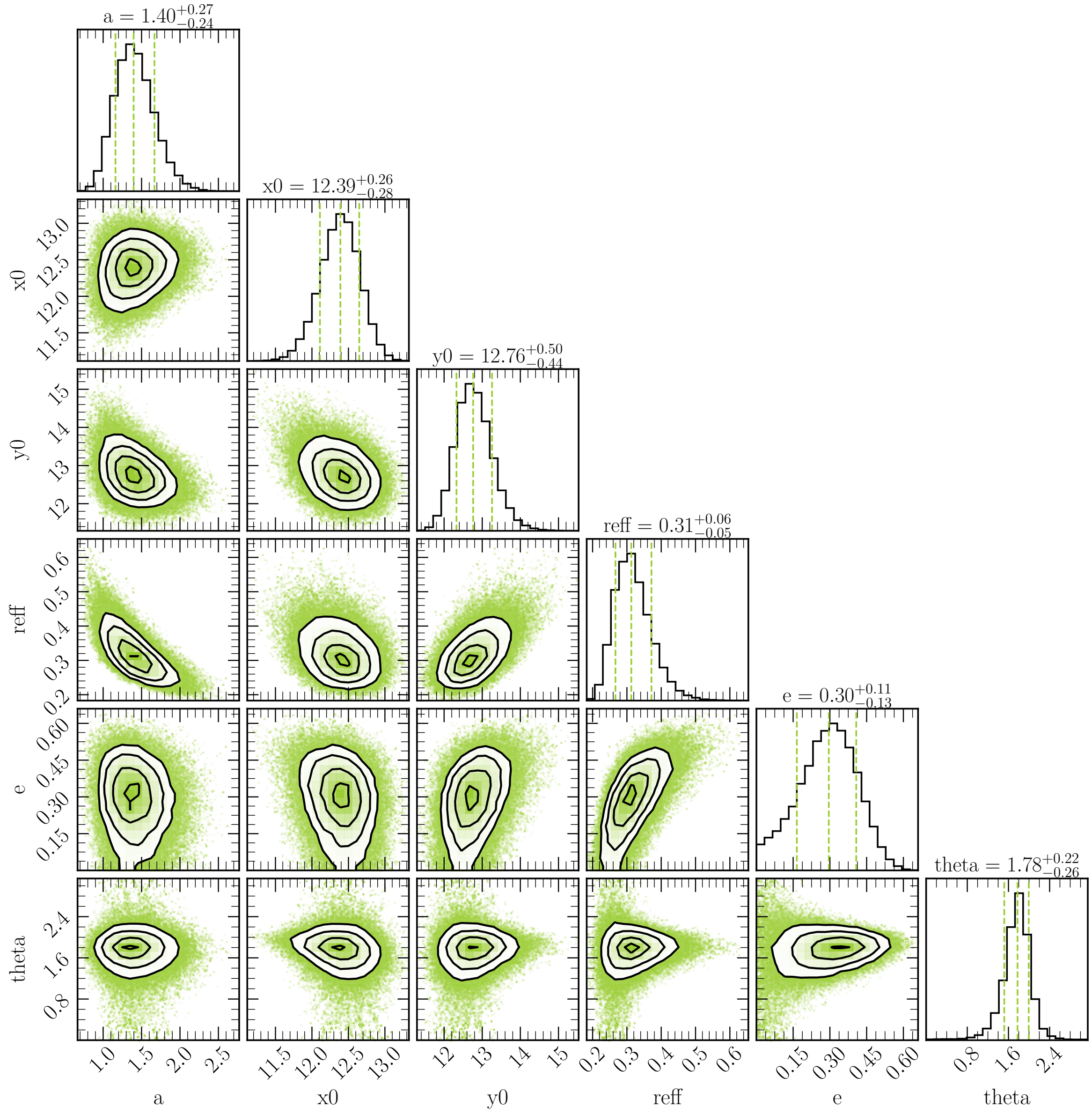

Figure A.5: Posterior distributions of parameters of the two-dimensional UV surface brightness, setting the Sérsic index equals 1. Black contours in the 2D posterior distributions and the dashed green lines in the histograms correspond to 16%, 50%, and 84% confidence regions.

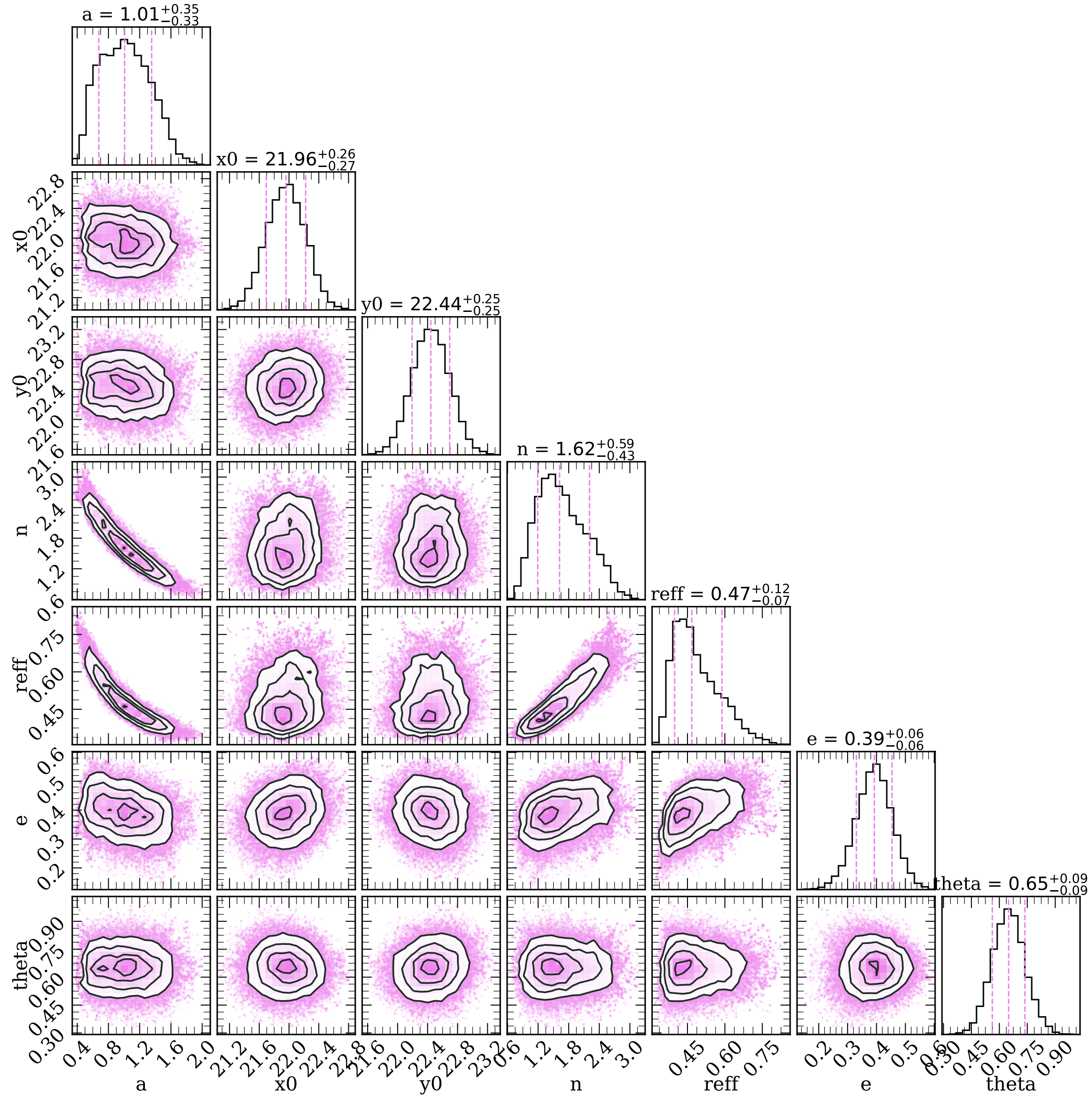

Figure A.6: Posterior distributions of parameters of the two-dimensional [C II] surface brightness, setting the Sérsic index as a free parameter. The Sérsic profile model also includes the surface brightness at the effective radius (a), the central pixel position (x_0 and y_0), the effective half-light radius ($r_{\rm eff}$), ellipticity (e), and the rotation angle (theta). Black contours in the 2D posterior distributions and the dashed pink lines in the histograms correspond to 16%, 50%, and 84% confidence regions.

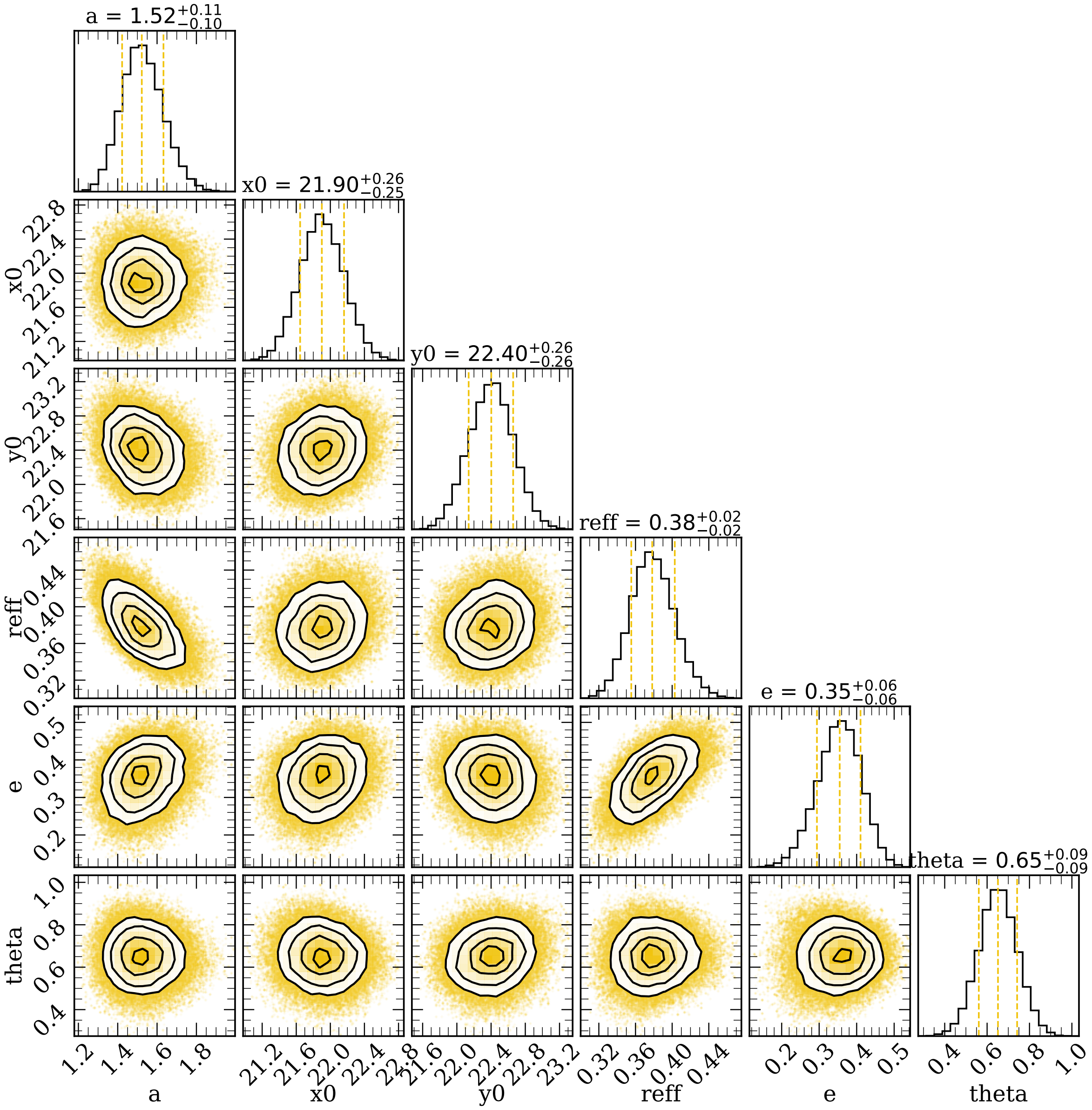

Figure A.7: Posterior distributions of parameters of the two-dimensional [C II] surface brightness, setting the Sérsic index equals to 1. Black contours in the 2D posterior distributions and the dashed yellow lines in the histograms correspond to 16%, 50%, and 84% confidence regions.

Table A.2: Best-fit parameters for each ring as a ^{3D}BAROLO output.

Ring	$\mathrm{v_{rot}}$ (km $\mathrm{s^{-1}}$)	$\mathrm{v_{disp}}$ (km $\mathrm{s^{-1}}$)	INC (deg)	P.A. (deg)	V^{sys} (km $\mathrm{s^{-1}}$)
1	104^{+10}_{-12}	15^{+7}_{-6}	24^{+3}_{-3}	179^{+4}_{-4}	-9^{+5}_{-5}
2	110^{+25}_{-21}	28^{+10}_{-7}	21^{+10}_{-8}	170^{+9}_{-10}	-15^{+5}_{-4}
3	44^{+5}_{-6}	36^{+9}_{-13}	25^{+5}_{-3}	182^{+4}_{-5}	-1^{+8}_{-8}

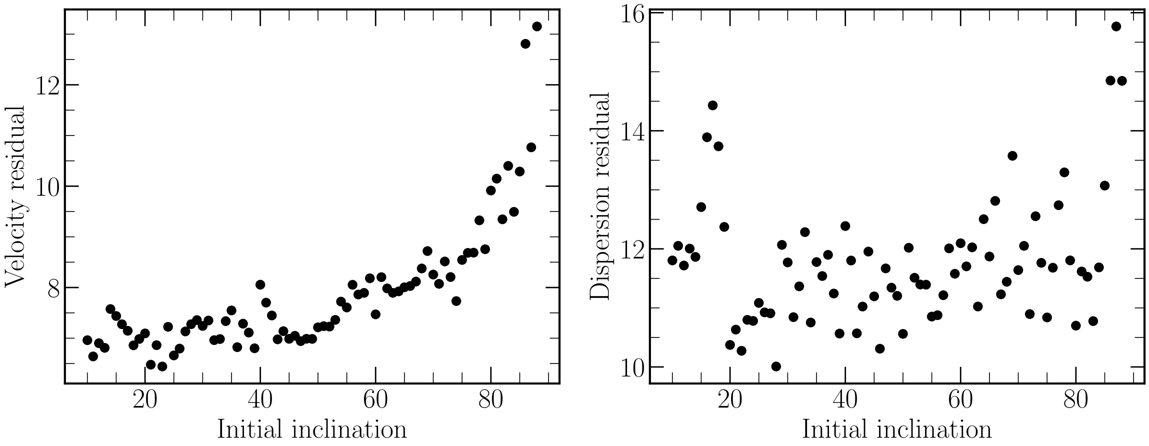

Figure A.8: Residuals (data - model, weighted by the [C II] moment-0 map) of the trial-and-error tests for the radial (left panel) and dispersion velocities (right panel) maps for initial inclinations ranging from 10 to 90 deg.

APPENDIX B

CRISTAL-05

B.1 [C II] MOMENT-0 MAP

In Figure B.1, we display the non-JvM [C II] moment-0 maps for the combined datasets obtained using the *tclean* task of CASA software using Briggs weighting, with robust = 0.5. The map represents the collapsed line cube, averaging the emission within the full-width tenth maximum centered at the [C II] line frequency.

B.2 DYNAMICAL MODELLING

In Figures B.2 we show the posterior distributions of the free parameters of the Dysmalpy routine.

B.3 ENVIRONMENT

Our observations cover a primary beam of $r_{PB} = 15''$, which translates into a projected area of 25 Mpc^2. We report the detection of 3 galaxies in the continuum maps, with no [C II] emission counterpart. Since the merger frequency is enhanced in overdensities, we explore the possibility that CRISTAL-05 is located close to the density peak of a protocluster environment. These galaxies are identified in the COSMOS2015 survey (Laigle et al., 2016) as 684856, 15086, and 686297, whose distant respectively 51, 70, and 86 kpc. None of the sources have an available spectroscopic redshift, but COSMOS 2020 assigned a photometric redshift of $z_{phot}^{15086} = 1.91$ and

z_{phot}^{686297}. Target 684856 was not covered from COSMOS2020 but COSMOS 2015 found z_{phot}^{684856} = 5.13. At this redshift, we did not find a [C II] detection in the location of 684856. Therefore, we see no evidence that CRISTAL-05 is within a galaxy overdensity at z = 5.5.

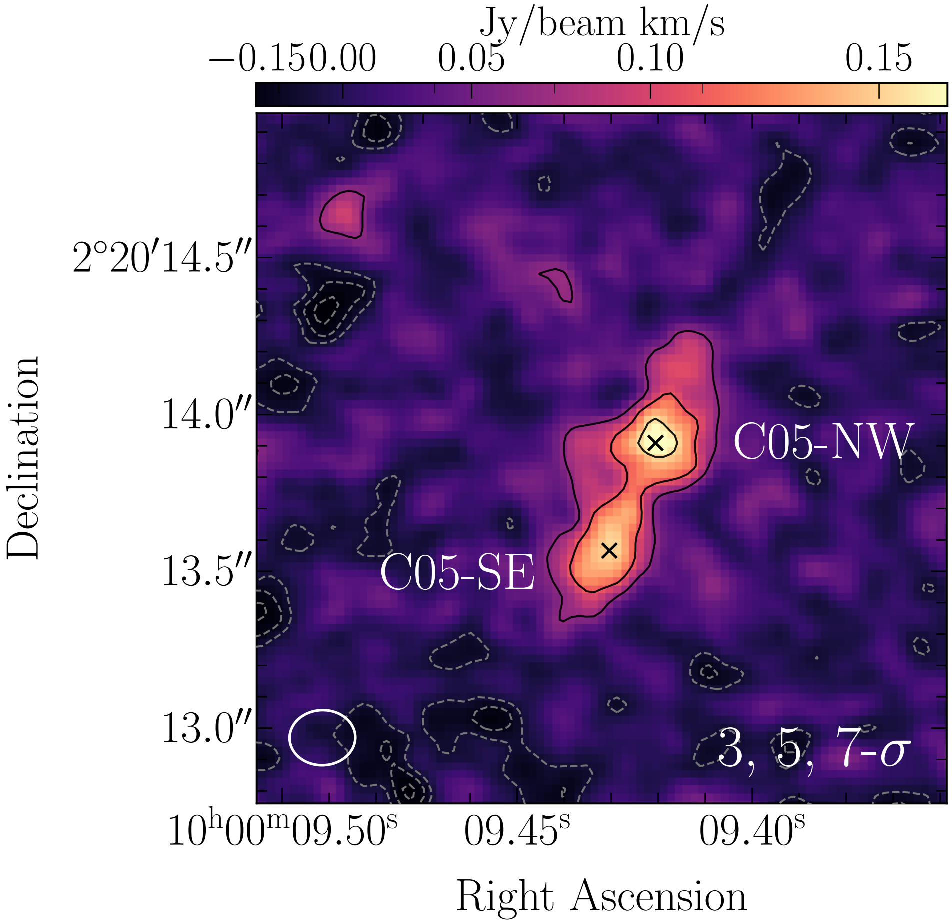

Figure B.1: ALMA [C II] moment-0 map (non-JvM corrected), for a Briggs weighting and robust = 0.5. The overlaid black contours correspond to the 3, 5, 7-$\sigma_{[CII]}$ levels, where $\sigma_{[CII]} = 0.02$ Jy/beam km s^{-1} is the rms noise level. The white ellipse indicates the beam size of $0.21'' \times 0.18''$.

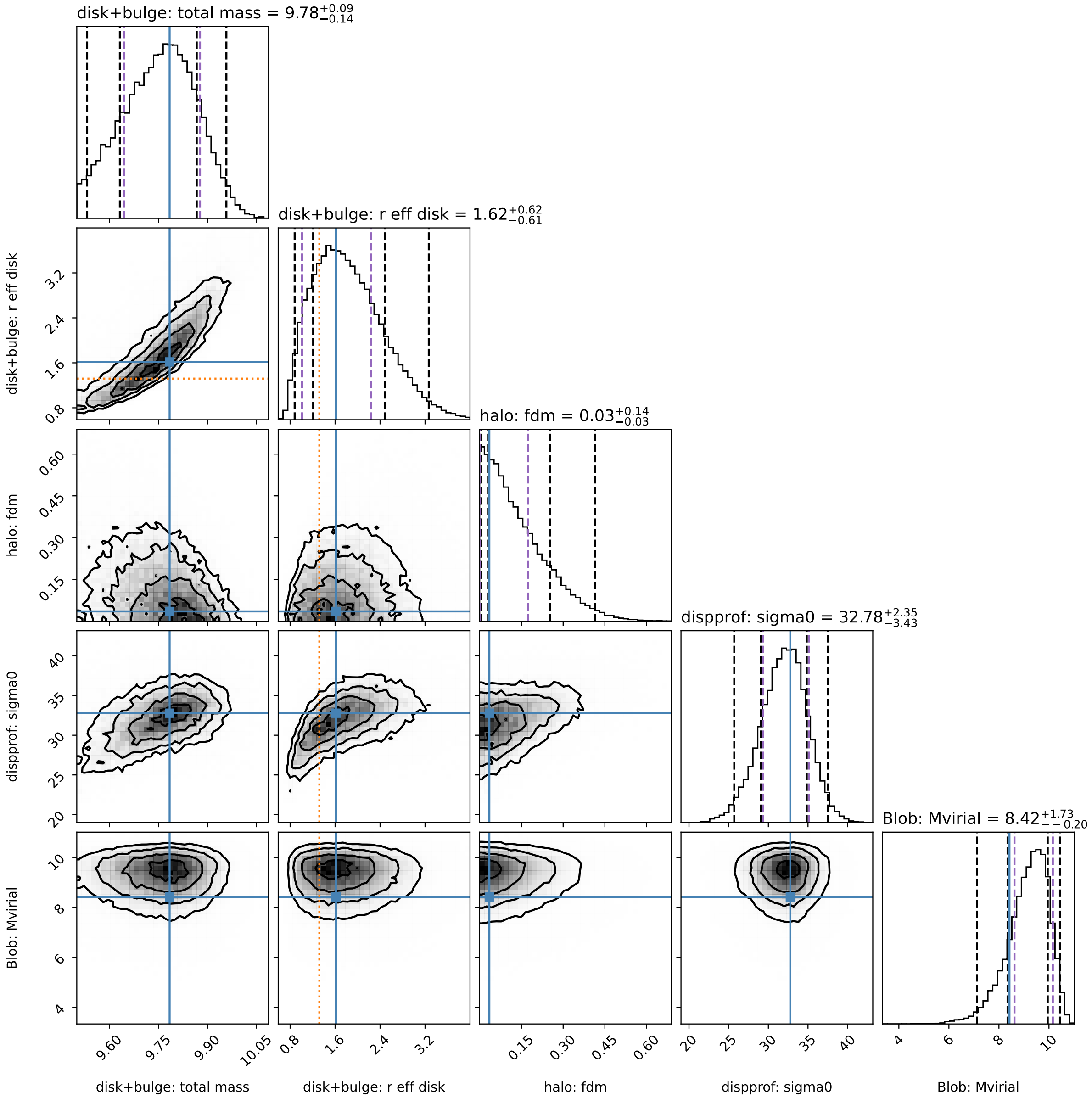

Figure B.2: Posterior distributions for the kinematical modeling in C05-NW .